THE UNIVERSITY *of* EDINBURGH

Satellite Investigations of Ice-Ocean Interactions in the Amundsen Sea Sector of West Antarctica

Malcolm McMillan

Thesis submitted in fulfilment of
the requirements for the degree of
Doctor of Philosophy
to the
University of Edinburgh

2012

Declaration

I declare that this thesis has been composed solely by myself and that it has not been submitted, either in whole or in part, in any previous application for a degree. Except where otherwise acknowledged, the work presented is entirely my own.

Malcolm McMillan

January 2012

Abstract

This thesis analyses satellite-based radar data to improve our understanding of the interactions between the Antarctic Ice Sheet and the ocean in the Amundsen Sea Sector of West Antarctica. Over the last two decades, the European Remote Sensing (ERS) Satellites have provided extensive observations of the marine and cryospheric environments of this region. Here I use this data record to develop new datasets and methods for studying the nature and drivers of ongoing change in this sector. Firstly, I develop a new bathymetric map of the Amundsen Sea, which serves to provide improved boundary conditions for models of (1) ocean heat transfer to the ice sheet margin, and (2) past ice sheet behaviour and extent. This new map augments sparse ship-based depth soundings with dense gravity data acquired from ERS altimetry and achieves an RMS depth accuracy of 120 meters. An evaluation of this technique indicates that the inclusion of gravity data improves the depth accuracy by up to 17 % and reveals glaciologically-important features in regions devoid of ship surveys. Secondly, I use ERS synthetic aperture radar observations of the tidal motion of ice shelves to assess the accuracy of tide models in the Amundsen Sea. Tide models contribute to simulations of ocean circulation and are used to remove unwanted signals from estimates of ice shelf flow velocities. The quality of tide models directly affects the accuracy of such estimates yet, due to a lack of *in situ* records, tide model accuracy in this region is poorly constrained. Here I use two methods to determine that tide model accuracy in the Amundsen Sea is of the order of 10 cm. Finally, I develop a method to

map 2-d ice shelf flow velocity from stacked conventional and multiple aperture radar interferograms. Estimates of ice shelf flow provide detail of catchment stability, and the processes driving glaciological change in the Amundsen Sea. However, velocity estimates can be contaminated by ocean tide and atmospheric pressure signals. I minimise these signals by stacking interferograms, a process which synthesises a longer observation period, and enhances long-period (flow) displacement signals, relative to rapidly-varying (tide and atmospheric pressure) ones. This avoids the reliance upon model predictions of tide and atmospheric pressure, which can be uncertain in remote regions. Ice loss from Amundsen Sea glaciers forms the largest component of Antarctica's total contribution to sea level, yet because present models cannot adequately characterise the processes driving this system, future glacier evolution is uncertain. Observations and models implicate the ocean as the driver of glaciological change in this region and have focussed attention on improving our understanding of the nature of ice-ocean interactions in the Amundsen Sea. This thesis contributes datasets and methods that will aid historical reconstructions, current monitoring and future modelling of these processes.

Acknowledgements

This work was funded by the UK Natural Environment Research Council's National Centre for Earth Observation, through a Centre for Polar Observation and Modelling PhD studentship.

I thank my supervisors, Andy Shepherd and Pete Nienow, for all their help and advice during the past three years. I am grateful to Anthony Newton for acting as my advisor throughout this time. I thank my examiners, Adrian Luckman and Martin Siegert, for their time and effort in reading and examining my thesis.

Thanks also go to my office mates, for their humour and friendship, and in particular to those who have shared an enthusiasm for discussing all things ice-related - Kate, Steve, Eero, Ian, Noel, Aud and Tom. Finally, thanks to my parents and to Anna for all their help and support.

Contents

List of Tables

List of Figures

Chapter 1

Introduction

1.1 Aim

The aim of this thesis is to use satellite-based radar observations to develop datasets and methods to improve our understanding of ice-ocean interactions in the Amundsen Sea Sector of the West Antarctic Ice Sheet (WAIS). In recent years, this region has exhibited signs of rapid glaciological change, which has fuelled speculation as to its stability in a changing climate. This thesis will add to a growing body of work which details the processes governing the response of the WAIS to changes in its external environment over a range of timescales.

1.2 Motivation

It is almost 50 years since the first scientific observations of Antarctica were made from space. Since then, satellites have revolutionised our ability to monitor the Antarctic Ice Sheet (AIS) on a continent-wide scale; detailing the diverse

behaviour of a vast ice sheet. During this period, satellites have identified coastal regions of the WAIS which are out of balance, and where outlet glacier dynamics are changing rapidly (Rignot, 2008). Interpreting the significance of these changes is difficult given our limited understanding of the complex interactions between the ice sheet and its surrounding environment. Global-scale models do not adequately account for the interactions between ice, atmosphere and ocean and as a result are unable to simulate the current coastal ice mass imbalances (Huybrechts, 2004). Satellite records are of insufficient duration to determine whether we are witnessing a secular anthropogenically-driven trend or merely a snapshot of Earth's natural variability. As a result, the implications of current observations are unclear, and the future contribution of the AIS to sea level rise remains uncertain (Lemke *et al.*, 2007).

Satellite observations from the last two decades have shown the Amundsen Sea Sector of the WAIS to be a system out of balance; losing more mass at its margins than it accumulates through precipitation (Rignot, 1998; Shepherd *et al.*, 2001; Thomas *et al.*, 2004). Currently this sector has the greatest mass deficit of all of Antarctica (Shepherd and Wingham, 2007) and is losing mass at a rate comparable to that of the entire Greenland Ice Sheet (Turner *et al.*, 2009). The Pine Island Glacier has become an icon of the change occurring in this area, exemplifying the characteristics expected from an out-of-balance system; both grounded and floating ice are thinning (Shepherd *et al.*, 2001, 2004; Thomas *et al.*, 2004; Pritchard *et al.*, 2009) and accelerating (Rignot, 2008), and the grounding line of the glacier is retreating (Rignot, 1998; Joughin *et al.*, 2010).

As a whole, the Amundsen Sea Sector holds enough ice to raise sea levels by approximately 1.5 metres (Rignot, 2001). Much of the ice rests on bedrock well below sea level and many of the ice streams draining this sector sit in deep troughs that deepen further inland (Lythe and Vaughan, 2001; Holt *et al.*, 2006; Vaughan *et al.*, 2006). Theoretical arguments (Weertman, 1974; Schoof, 2007) suggest that

such a configuration may be intrinsically unstable; once the ice sheet begins to retreat, it is impossible for it to stabilise whilst it remains on an inward-sloping bed. Evidence of past ice sheet behaviour indicates that the Amundsen Sea Sector of the WAIS has indeed undergone a progressive retreat since the Last Glacial Maximum (Smith *et al.*, 2011), across the broadly inward-sloping continental shelf (Nitsche *et al.*, 2007). Furthermore, there have been periods of rapid sea level rise (Meltwater Pulse 1a, $\sim$ 14 000 years ago, contributing in excess of 5 cm/yr) and a WAIS source to this event cannot be discounted (Bassett *et al.*, 2007). These arguments have fuelled speculation (Mercer, 1978; Vaughan, 2008) that the influence of humans could drive the WAIS into a more rapid and unstoppable retreat, and so accelerate rates of sea level rise beyond current expectations. Recent satellite observations of accelerating mass imbalances in the Amundsen Sea Sector of the WAIS have raised the possibility that we may be witnessing such a scenario. However, from the short timespan of the satellite era, it is difficult to determine whether this is indeed occurring, or whether we have simply captured a snapshot of the long-term post-LGM ice sheet decline. This uncertainty has reinforced the need to continue monitoring this region and to understand the processes that are driving change. This will allow tighter constraints to be placed upon the probability and timescales of a more rapid collapse event occurring.

Numerous studies have identified the ocean as the probable source of the recent elevated Amundsen Sea Sector ice imbalance (Rignot and Jacobs, 2002; Shepherd *et al.*, 2002; Payne *et al.*, 2004; Shepherd *et al.*, 2004). Atmospheric factors have been rejected as the principle driver on the basis of insufficient surface melting (Tedesco, 2009) and snowfall variability (Wingham *et al.*, 1998; Shepherd *et al.*, 2004). The synchronised thinning of ice shelves and their upstream catchments (Shepherd *et al.*, 2002, 2004) is consistent with the hypothesis of ocean-driven change. This hypothesis is further supported by observations of warm Circumpolar Deep Water breaching the continental shelf break (Walker

et al., 2007), flowing along troughs in the continental shelf (Nitsche *et al.*, 2007) and accessing the cavities beneath ice shelves (Jacobs *et al.*, 1996; Jenkins *et al.*, 2010). This water is several degrees above the *in situ* freezing point and thus capable of driving the high rates of basal melting which have been estimated for ice shelves in this region (Jacobs *et al.*, 1996; Rignot and Jacobs, 2002; Shepherd *et al.*, 2004). However, glaciers draining into the Amundsen Sea exhibit spatial (Shepherd *et al.*, 2004; Rignot, 2008) and temporal (Joughin *et al.*, 2003; Rignot, 2008) variations in behaviour. Not all glaciers are accelerating and retreating, ice shelf thinning rates vary by an order of magnitude (Shepherd *et al.*, 2004), and periods of change have been punctuated by intervals of relative mass balance and stability (Joughin *et al.*, 2003; Rignot, 2008).

The spatially and temporally differing behaviour of glaciers draining into the Amundsen Sea indicates a complex system of ice-ocean interactions that at present is poorly understood. This lack of understanding limits the ability of models to extrapolate from current observations to future trends in ice mass loss. Consequently, the contribution of this region to sea level projections, originating from changes to glacier dynamics, remains unaccounted for (Lemke *et al.*, 2007). To address this, the significance of various factors that modulate glaciological behaviour in this region must be determined. These factors include subglacial topography, ocean bathymetry, ocean circulation, ocean temperature, heat transfer in sub-ice shelf cavities, and the dynamic response of glaciers to events occurring both during and prior to the satellite era. To understand the relative influences of these factors, and the timescales over which they operate, requires observations with the resolution and accuracy required by models. These can extend the record of contemporary change and provide datasets with which to validate and constrain models of ice-ocean interactions. In remote regions, such as the Amundsen Sea, satellites are well suited for this purpose, providing spatially extensive datasets at the spatial and temporal resolution required by

models. These observations can contribute towards an improved understanding of ice-ocean interactions, and a narrowing of the uncertainty associated with the WAIS contribution to sea level rise.

1.3 Objectives

The aim of this thesis is to utilise satellite-based radar data to develop methods and datasets to improve our understanding of ice-ocean interactions in the Amundsen Sea Sector of the West Antarctic Ice Sheet. Within the current literature relating to ice-ocean interactions in the Amundsen Sea, there are several specific areas in which improved datasets and methods could benefit our understanding, and to which the application of satellite-based radar is well suited. Currently there is (1) no bathymetric map of the Amundsen Sea that utilises data sources other than sparse ship-based surveys, (2) uncertainty regarding the accuracy of tide models in this region, and (3) uncertainty regarding the degree of contamination, arising from the vertical motion of an ice shelf, in many ice shelf velocity estimates. These issues hamper both modelling studies of ice-ocean interactions and the monitoring of ongoing glaciological change. As such, they motivate the following objectives of this thesis:

1. To use satellite radar data to produce a new bathymetric map of the Amundsen Sea.

2. To use satellite radar data to assess the accuracy of tide models in the Amundsen Sea.

3. To develop an interferometric synthetic aperture radar-based method for mapping ice shelf velocity, that minimises and quantifies the effect of ice shelf vertical motion.

Objective (1) will provide a new set of boundary conditions of improved certainty for modelling studies of past ice sheet behaviour and current ocean heat transfer to the base of ice shelves. Past ice sheet behaviour provides context for current observations (Lowe and Anderson, 2002) and analogues for how the ice sheet might respond to changes in climate. Models of ocean heat transfer can quantify the heat currently available to melt each ice shelf in the Amundsen Sea, and provide predictions of how a changing climate may affect heat availability (Thoma *et al.*, 2008).

Objective (2) narrows the uncertainty associated with tide model predictions in the Amundsen Sea. Tides are one of the main drivers of ocean circulation and mixing beneath ice shelves and therefore tide models are an essential component of modelling studies of ice-ocean interactions (Makinson *et al.*, 2011). Additionally, tide model predictions are essential to many satellite-based methods of estimating ice shelf elevation (Bamber *et al.*, 2009) and flow speeds (Rignot and Jacobs, 2002), which are themselves key observables for both monitoring and understanding glaciological change. Tide model accuracy directly affects the accuracy of these estimates and must therefore be determined.

Objective (3) contributes towards a reduction in the error and uncertainty associated with many satellite-derived estimates of ice shelf velocity. Improved velocity estimates benefit the ongoing monitoring of ice shelf stability, as accelerating flow can be a precursor to ice shelf collapse (Rignot *et al.*, 2004). High quality velocity maps also form an essential part of satellite-based methods to determine ocean melting beneath ice shelves (Joughin and Padman, 2003) and so contribute to efforts to understand the processes driving glaciological change in the Amundsen Sea.

Chapter 2

The Amundsen Sea Sector of the West Antarctic Ice Sheet

2.1 Physical Setting

The Antarctic Ice Sheet (AIS) is the largest ice mass on Earth. With an ice volume of 25 million km^3 (Lythe and Vaughan, 2001), it covers an area larger than Europe and holds $\sim$ 70 % of Earth's freshwater (Turner *et al.*, 2009). The AIS consists of three distinct components; the East and West Antarctic Ice Sheets (covering areas of 10.3 x 10^6 km^2 and 2.0 x 10^6 km^2 respectively), and the Antarctic Peninsula (spanning an area of 0.5 x 10^6 km^2). The work of this thesis focuses upon the Amundsen Sea Sector of the West Antarctic Ice Sheet (WAIS) (figure 2.1). This sector drains over 40 % (by volume) of the WAIS (Payne *et al.*, 2004) and holds sufficient ice to raise sea levels by $\sim$ 1.5 metres (Rignot, 2001). The WAIS is the only marine ice sheet that still exists in our current climate. Approximately 75 % of its area currently rests on bedrock below sea level (Lythe and Vaughan, 2001; Vaughan *et al.*, 2001), and much of this area

would remain submerged even if the ice was removed. The conditions at the base of the WAIS vary between areas of soft deformable marine sediments, deposited during past periods of WAIS deglaciation, and hard non-deformable sediments or bedrock (Anandakrishnan *et al.*, 1998; Bingham and Siegert, 2007; Joughin *et al.*, 2009; Rippin *et al.*, 2011). The WAIS is predominantly a warm-based ice sheet (Siegert, 2008), with sub-glacial melting driven by a combination of frictional and geothermal heat (Kamb, 2001; Raymond *et al.*, 2001). The presence of water, a smooth base and deformable sediment underneath large regions of the ice sheet allows the ice to slide over its base and provides the conditions required for fast-flowing ice streams and outlet glaciers to persist (Alley *et al.*, 1986; Siegert *et al.*, 2004, 2008).

Several fast flowing ice streams and outlet glaciers drain the Amundsen Sea Sector of the WAIS. These start as a network of tributaries hundreds of kilometres inland (Rignot *et al.*, 2004), which converge and accelerate to flow at speeds of several kilometres per year as they reach the coast (Rignot, 2008). Many of these glaciers sit in deep, narrow bedrock troughs, where the bedrock is in places around 1000 metres lower than its surroundings, and deepens further inland (figures 2.2 and 2.3) (Holt *et al.*, 2006; Vaughan *et al.*, 2006). At present, the two largest glaciers (Pine Island and Thwaites) are grounded at their termini on regions of hard bedrock (Joughin *et al.*, 2009). Seaward of the grounding line (the boundary between bedrock, ice and ocean), the ice streams form small floating ice shelves, typically several thousand square kilometres in area (with the exception of the larger Abbott and Getz Ice Shelves), and 500-1000 meters thick (Shepherd *et al.*, 2004). It is here that the majority of ice loss from this region occurs, primarily through ocean melting at the base of ice shelves (Jacobs *et al.*, 1996; Rignot and Jacobs, 2002). Atmospheric-driven surface melting is minimal in this region (van den Broeke *et al.*, 2006; Tedesco, 2009), as sub-zero temperatures predominate at this latitude.

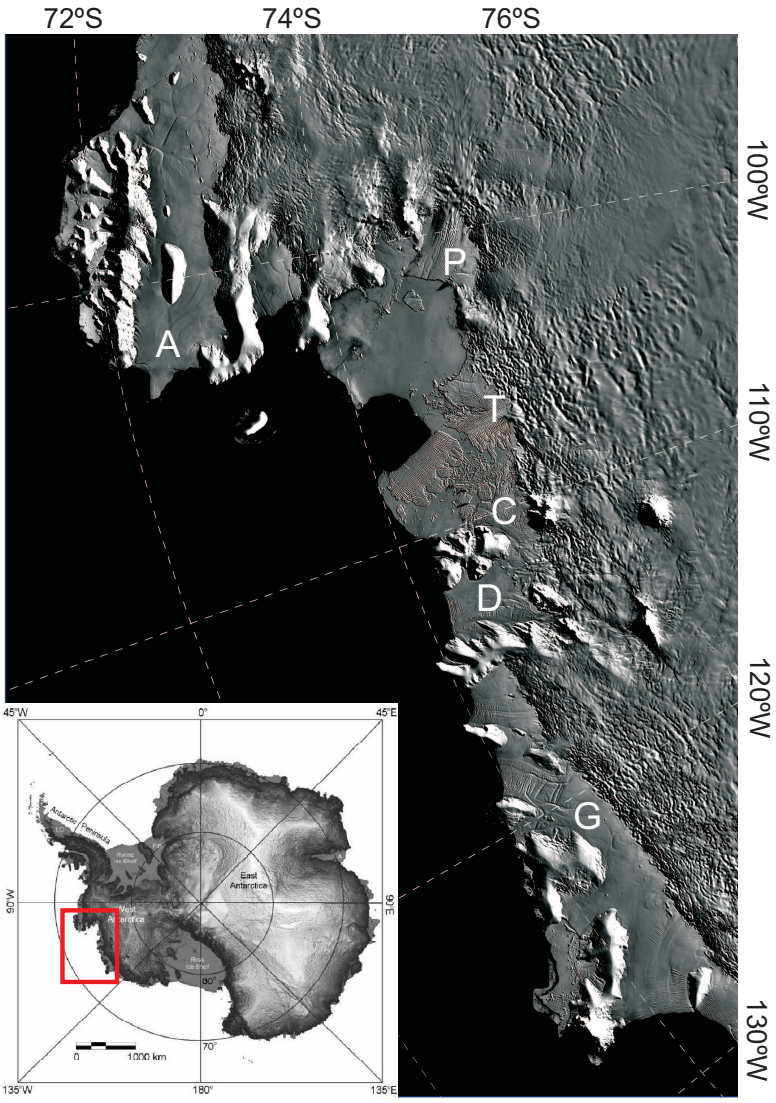

Figure 2.1: The Amundsen Sea Sector of the West Antarctic Ice Sheet (location marked by red box in inset figure). The main image is taken from the MODIS mosaic of Antarctica (Haran *et al.*, 2006); *A*, Abbott Ice Shelf; *P*, Pine Island Ice Shelf; *T*, Thwaites Ice Shelf; *C*, Crosson Ice Shelf; *D*, Dotson Ice Shelf; *G*, Getz Ice Shelf. Inset is a shaded relief of Antarctica's surface topography, adapted from Bamber *et al.* (2009).

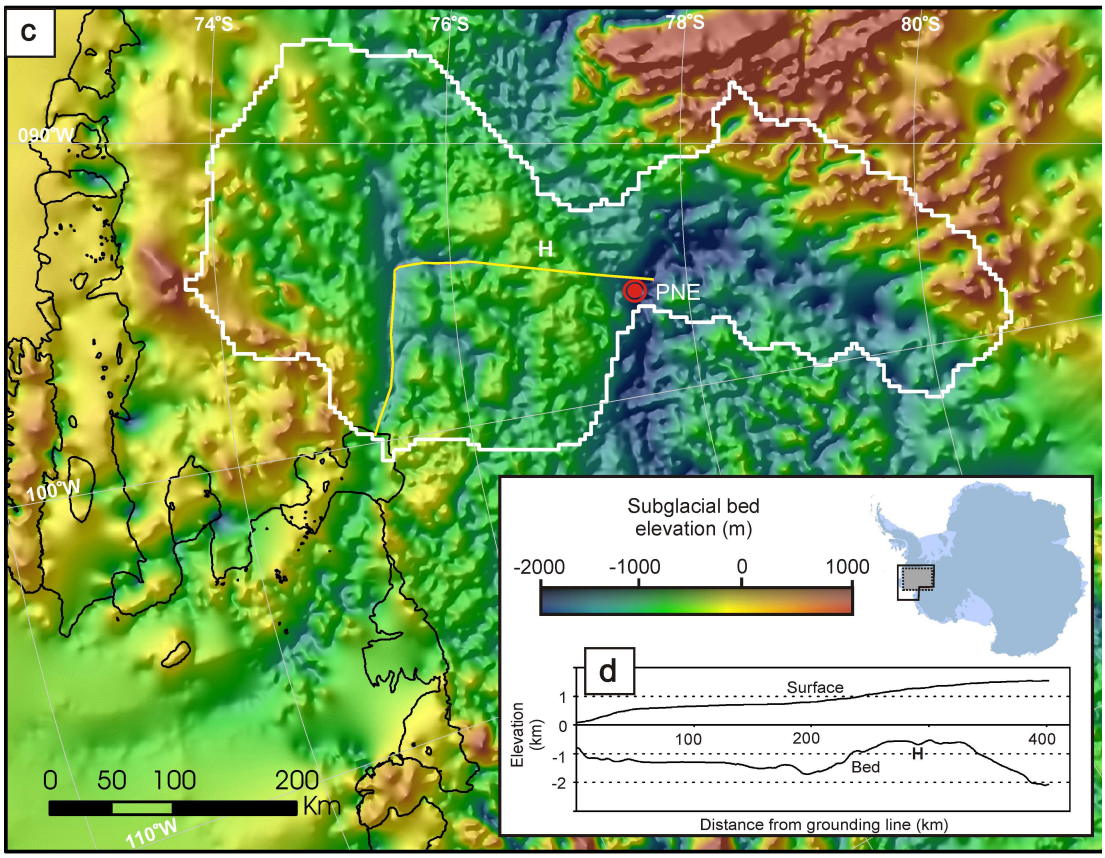

Figure 2.2: Bedrock topography of the Pine Island Glacier drainage basin, in the Amundsen Sea Sector of the WAIS, from Vaughan *et al.* (2006). The black line delineates the coastline and ice shelves; white line indicates Pine Island Glacier drainage basin; yellow line locates transect shown in inset figure; *H* indicates location of bedrock high; *PNE* marks location of field camp used in survey. Inset shows the bed depth of a transect along the main Pine Island Glacier trough, indicating that the bed deepens for $\sim$ 200 km inland.

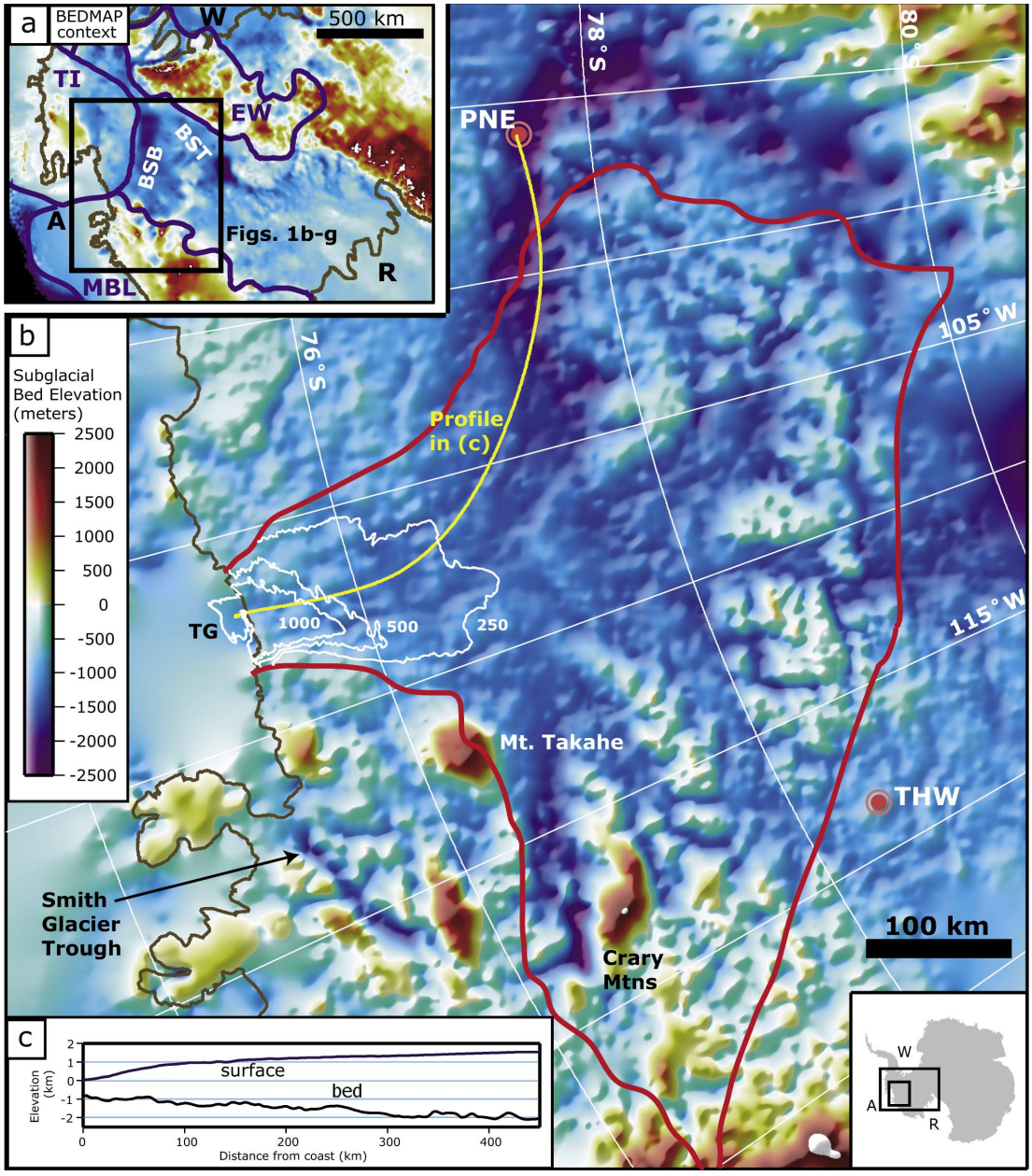

Figure 2.3: Bedrock topography of the Thwaites Glacier drainage basin, in the Amundsen Sea Sector of the WAIS, from Holt *et al.* (2006). The brown line delineates the coastline; red line indicates Thwaites Glacier drainage basin; white lines are ice velocity contours; yellow line locates position of transect shown in inset figure *c*; *PNE* marks location of field camp used in survey. Inset *a* shows a previous map of bed topography of the WAIS (BEDMAP). Inset *c* shows the bed depth along the transect marked in the main figure, indicating continual bed deepening into the WAIS interior.

2.2 Observations of Ice Sheet Change in the Satellite Era

During the late twentieth and early twenty-first centuries, satellites have provided a new view of the AIS. The wealth of data has revealed a complex picture of ice sheet behaviour and provided new insights into the mechanisms and timescales of glaciological change. Satellites have provided scientists with a platform from which to monitor the ice sheet on a continent-wide scale, and this has enabled comprehensive estimates of the AIS mass balance to be made. These studies (see Shepherd and Wingham (2007) for a full summary), which are based upon a range of techniques, agree that current AIS mass loss is dominated by losses to glaciers draining into the Amundsen Sea (figure 2.4). Estimates from 1996 and 2000 (Thomas *et al.*, 2004) indicated that over this four year period these glaciers discharged $\sim$ 60 % more ice than they accumulated within their catchments. From being in near-balance in the 1970's (Rignot, 2008), glaciers draining into the Amundsen Sea are now estimated to be losing between 50 Gt and 137 Gt of mass each year (Turner *et al.*, 2009). This is comparable to the rate of mass loss from the entire Greenland Ice Sheet (Turner *et al.*, 2009). The large range in current mass balance estimates reflects the different methods used, and the varying timespan and spatial coverage over which these measurements were made. In the following sections I summarise the satellite observations of glaciological change in the Amundsen Sea Sector of the WAIS.

2.2.1 Thinning of Grounded Ice

At the end of the last century, satellite-based radar altimetry showed that the ice of the Amundsen Sea Sector of the WAIS was thinning (Wingham *et al.*, 1998). Further estimates (Shepherd *et al.*, 2002) indicated that thinning rates,

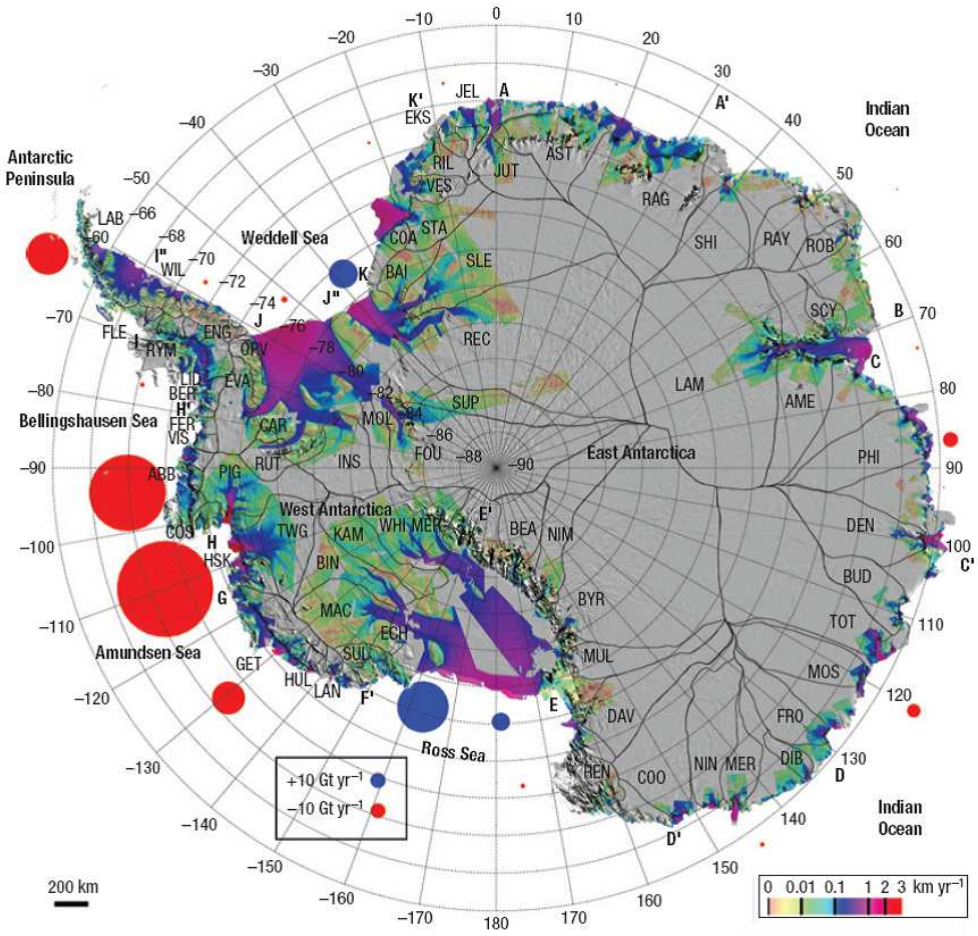

Figure 2.4: Ice velocity of the Antarctic Ice Sheet, from Rignot *et al.* (2008). Black lines delineate catchment basins. Coloured circles indicate mass loss (red) and mass gain (blue); circle radius indicates magnitude of imbalance.

when averaged over the entire Amundsen Sea Sector (grounded ice only), were 9 ± 2 cm yr^{-1}, during the period 1991-2000. Thinning was most pronounced over fast flowing areas of ice, suggesting that it was likely being driven by glacier dynamics. Maximum (grounded ice) thinning rates of 1.6 ± 0.2 m yr^{-1}, 2.6 ± 0.5 m yr^{-1} and 4.8 ± 0.3 m yr^{-1} were observed close to the grounding lines of the Pine Island, Thwaites and Smith glaciers, respectively (Shepherd *et al.*, 2001, 2002). These rates were beyond those expected from natural variability in snowfall accumulation; indeed they may have been an underestimate as variations in firn depth were not accounted for (Helsen *et al.*, 2008). Subsequently, repeat airborne observations from 2002-2004 (Thomas *et al.*, 2004) suggested that inland thinning rates along a 200 km section of the Pine Island Glacier had doubled compared to the values determined by Shepherd *et al.* (2001). Furthermore, thinning rates close to the grounding lines of several glaciers were estimated to now approach 6 m yr^{-1}. Although some of the variation may have been due to the different spatial scales of the observations (of the order of metres for airborne, versus kilometres for satellite-based radar), Thomas *et al.* (2004) concluded that the observed changes were at least in part due to a real acceleration in the thinning rate. More recently, laser altimetry acquired during the period 2003-2007 (Pritchard *et al.*, 2009) indicated thinning rates of up to 6 m yr^{-1}, 4 m yr^{-1} and 9 m yr^{-1} close to the grounding lines of the Pine Island, Thwaites and Smith Glaciers, respectively (figure 2.5). A separate study (Wingham *et al.*, 2009) has confirmed these trends over the central trunk of the Pine Island Glacier, finding that between 1995 and 2006 thinning rates had quadrupled. Combined, these observations document almost two decades of accelerating thinning rates over the fast flowing, grounded ice that drains into the Amundsen Sea.

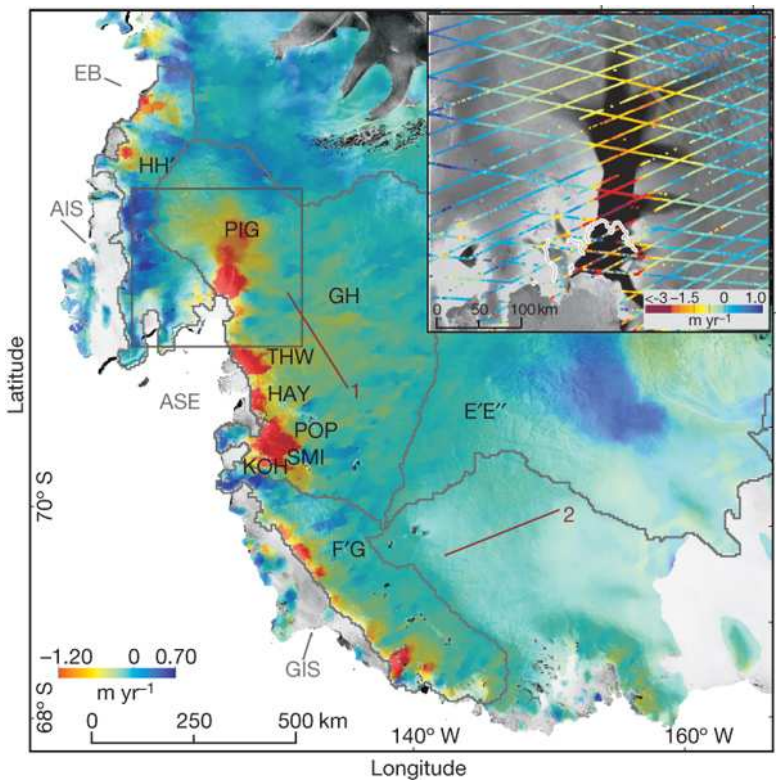

Figure 2.5: Rates of elevation change of grounded ice in the Amundsen Sea Sector of the WAIS between 2003 and 2007, determined from ICESat laser altimetry by Pritchard *et al.* (2009). *AIS*, Abbott Ice Shelf; *PIG*, Pine Island Glacier; *THW*, Thwaites Glacier; *HAY*, Haynes Glacier; *POP*, Pope Glacier; *SMI*, Smith Glacier; *KOH*, Kohler Glacier; *GIS*, Getz Ice Shelf. Inset shows thinning over Pine Island Glacier (marked by box in main figure). Profiles 1 and 2 are not shown here.

Table 2.1: Area, thickness and average 1992-2001 rates of elevation and thickness change of ice shelves floating in the Amundsen Sea, redrawn from Shepherd *et al.* (2004).

Ice Shelf	**Area (km^2)**	**Ice thickness (m)**	**Elevation rate ($cm\ year^{-1}$)**	**Thinning rate ($m\ year^{-1}$)**
Abbot	30 827	419	-6 ± 4	0.6 ± 0.4
Cosgrove	2553	729	-8 ± 3	0.7 ± 0.4
Pine Island	2365	657	-42 ± 4	3.9 ± 0.5
Thwaites	1687	698	-59 ± 7	5.5 ± 0.7
Crosson	3843	776	-49 ± 4	4.5 ± 0.5
Dotson	3433	469	-36 ± 2	3.3 ± 0.4
Getz	31 186	899	-17 ± 6	1.6 ± 0.6

2.2.2 Thinning of Ice Shelves

Between 1992 and 2001, satellite observations (Shepherd *et al.*, 2004) showed that all ice shelves in the Amundsen Sea underwent surface lowering (table 2.1). This was greatest (59 ± 7 cm yr^{-1}) for the centrally-located Thwaites Ice Shelf, and decreased towards the periphery of the embayment. The maximum observed rate of surface lowering corresponded to a thinning of 5.5 ± 0.7 m yr^{-1}, which has resulted in a 7 % thinning of the Thwaites Ice Shelf over the 9 year period of observation (Shepherd *et al.*, 2004). A context for this decadal record of thinning has been provided by Bindschadler (2002), who used a long-term record of Landsat imagery to estimate an upper bound of 4.8 m yr^{-1} for the mean thinning rate of the Pine Island Ice Shelf during the period 1973-2001. Because of several assumptions made in their study, the authors were not able to further constrain this estimate with a lower bound, and so the extent to which high thinning rates persisted before then 1990's remains uncertain.

2.2.3 Grounding Line Retreat

Changes in the position of the grounding line of a glacier reflect variations in ice thickness (assuming a constant sea level during the period of observation). Although satellites cannot directly detect the position of a glacier's grounding line, the technique of satellite-based radar interferometry can be used to locate a glacier's hinge line (the limit of tidal flexure) which is commonly taken as a surface expression of the grounding line (Rignot, 1998). Between 1992 and 1996, the grounding lines of the Pine Island and Thwaites glaciers were estimated (Rignot, 1998, 2001) to have retreated at a rate of 1.2 $\pm$ 0.3 km yr^{-1} and 0.4 $\pm$ 0.1 km yr^{-1}, respectively. A recent study of Pine Island Glacier (Joughin *et al.*, 2010) showed that since then grounding line retreat had continued at a comparable rate. Using an alternative method (altimeter-derived measurements of ice thinning, combined with ice surface and bedrock elevation data), Shepherd *et al.* (2002) derived estimates of grounding line retreat rates over the period 1991-2000 of 0.8 km yr^{-1}, 0.31 km yr^{-1} and 0.72 km yr^{-1} for the Pine Island, Thwaites and Smith glaciers, respectively. In the case of Pine Island Glacier, the retreat rate calculated by Shepherd *et al.* (2002) was based upon altimetry data located 13 km from the grounding line. This may have underestimated thinning at the grounding line, and explain why the retreat rate calculated by Shepherd *et al.* (2002) is slower than that derived by Rignot (1998).

2.2.4 Ice Acceleration

Satellite observations dating back to the 1970's have revealed large spatial and temporal variations in ice flow. Of all the glaciers draining into the Amundsen Sea, Pine Island Glacier has received perhaps the most attention, with an almost 40-year record of flow variability having been constructed (Joughin *et al.*, 2003;

Rignot, 2008). During this time there appear to have been two distinct periods of glacier acceleration (1974-1987 and 1994-2008) separated by an interval of more constant flow (Joughin *et al.*, 2003; Rignot, 2008). The timing of the earlier acceleration is only roughly constrained because of coarse temporal sampling, and may have extended prior to 1974. As of 2010, Pine Island Glacier was flowing at a speed approaching 4 km yr^{-1} close to its grounding line, which represents approximately an 80 % velocity increase since 1974, when the glacier was roughly in mass balance (Rignot, 2008). This type of behaviour is not ubiquitous throughout the Amundsen Sea Sector of the WAIS (figure 2.6). Whilst the Smith Glacier and Crosson Ice Shelf have undergone similarly high rates of acceleration (Rignot, 2008), the Dotson Ice Shelf, Kohler Glacier and easternmost sector of the Getz Ice Shelf maintained stable velocities in the period 1974-2006 (Rignot, 2008). Meanwhile, although the Thwaites Ice Shelf has accelerated, there has been no concurrent acceleration of the fast-flowing grounded ice stream, but instead a widening of this part of the Thwaites Glacier (Rignot, 2008).

2.2.5 A Glimpse of WAIS Instability?

The glaciological behaviour of the Amundsen Sea Sector of the WAIS is consistent with that expected from an unstable ice sheet in a state of retreat (Mercer, 1978). Specifically, the marine instability hypothesis (Weertman, 1974; Schoof, 2007) states that the grounding line of an ice sheet cannot be stable on an inward-sloping bed. With such a configuration, any retreat in the grounding line leads to an increase in ice thickness at the grounding line. This in turn causes an acceleration in ice flow (and hence ice discharge) across the grounding line, and results in the thinning of inland ice and further grounding line retreat. In such a scenario, ice sheet retreat is self-perpetuating, until a point is reached where the ice no longer rests on an inwardly-sloping bed. As a whole, the Amundsen Sea

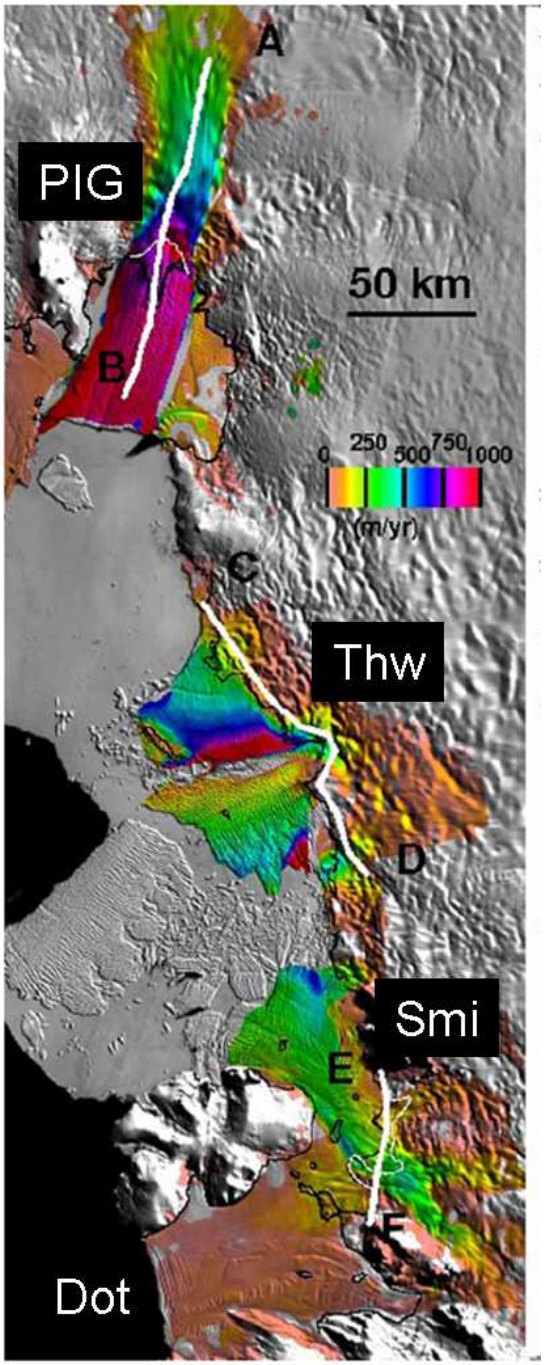

Figure 2.6: Ice velocity increase between 1996 and 2006. *PIG*, Pine Island Glacier; *Thw*, Thwaites Glacier; *Smi*, Smith Glacier and Crosson Ice Shelf; *Dot*, Dotson Ice Shelf, from Rignot (2008). Thin black lines indicate position of 1996 grounding lines; thin white lines are 2007 grounding lines. Thick white lines and *A*-*F* indicate transects that are not shown here.

Sector of the WAIS satisfies the criteria of a marine ice sheet that sits on a broadly inward-sloping bed (Holt *et al.*, 2006; Vaughan *et al.*, 2006; Nitsche *et al.*, 2007). Furthermore, this sector of the ice sheet has indeed been in long-term decline since the Last Glacial Maximum (LGM) some 20 000 years ago (Lowe and Anderson, 2002). The characterisation of the Amundsen Sea Sector of the WAIS as resting on a uniform reverse slope is of course a simplification; the topography is complex and contains numerous local highs which could halt or slow unstable retreat. The concern is, however, that current observations of a large ice mass deficit may indicate that an additional external forcing is now acting to drive an accelerated phase of unstable retreat.

It is against the backdrop of post-LGM deglaciation that contemporary satellite observations must be judged. To determine the significance of recent mass loss observations requires an understanding of whether, in the context of long-term ice retreat, the behaviour we are currently witnessing is anomalous. Have we merely captured a snapshot of the long term evolution of the ice sheet as it retreats across the inward-sloping continental shelf? Or are we observing elevated rates of change which are a response to some external forcing? If so, what is the nature of this forcing - is it anthropogenic in origin, or simply a result of the natural variability exhibited by Earth's system? Answering these questions requires an understanding of (1) the longer term behaviour of the ice sheet prior to contemporary satellite observations and (2) the processes driving recent changes to the ice sheet. These can provide an insight into whether or not we are witnessing the early stages of a more rapid ice sheet collapse. In the following sections I review evidence relating to the post-LGM history of the ice sheet and the processes driving current changes.

2.3 Post-LGM History of the Amundsen Sea Sector of the WAIS

In this section I provide an overview of the history of the Amundsen Sea Sector of the WAIS since the LGM, which is defined as the last period of maximum ice extent around Antarctica, $\sim$ 20 000 years ago. At that point in time the ice sheet extended to the continental shelf edge (Evans *et al.*, 2006; Larter *et al.*, 2009). Since then the ice sheet has retreated $\sim$ 500 km to its present day position, leaving behind a record of its past on what is now the Amundsen Sea floor. Evidence of post-LGM ice sheet behaviour has been acquired by ship-based surveys. These have provided imagery detailing the morphology of the seabed (figure 2.7) and sediment cores with which to constrain the timing of ice sheet retreat.

2.3.1 Ice Sheet Behaviour Inferred from Sea Floor Morphology

Ship-based surveys have mapped several sea-floor troughs that extend across the continental shelf from beneath current day ice shelves (Jacobs *et al.*, 1996; Lowe and Anderson, 2002; Dowdeswell *et al.*, 2004; Evans *et al.*, 2006; Larter *et al.*, 2009; Graham *et al.*, 2011). These troughs tend to become progressively deeper as they approach the current ice margin (Nitsche *et al.*, 2007). Surveys of these troughs have identified elongated bedforms on both the inner (Larter *et al.*, 2009) and outer (Evans *et al.*, 2006; Graham *et al.*, 2011) continental shelf. These bedforms are characteristic of ice streaming, and provide evidence that these troughs were once inhabited by paleo-ice streams that extended to close to the continental shelf edge. On the inner shelf, the troughs are incised with systems of subglacial meltwater channels, providing evidence that large volumes of water were discharged from beneath the ice sheet (Lowe and Anderson, 2002; Larter *et al.*, 2009). The frequency and duration of such events, however, remains

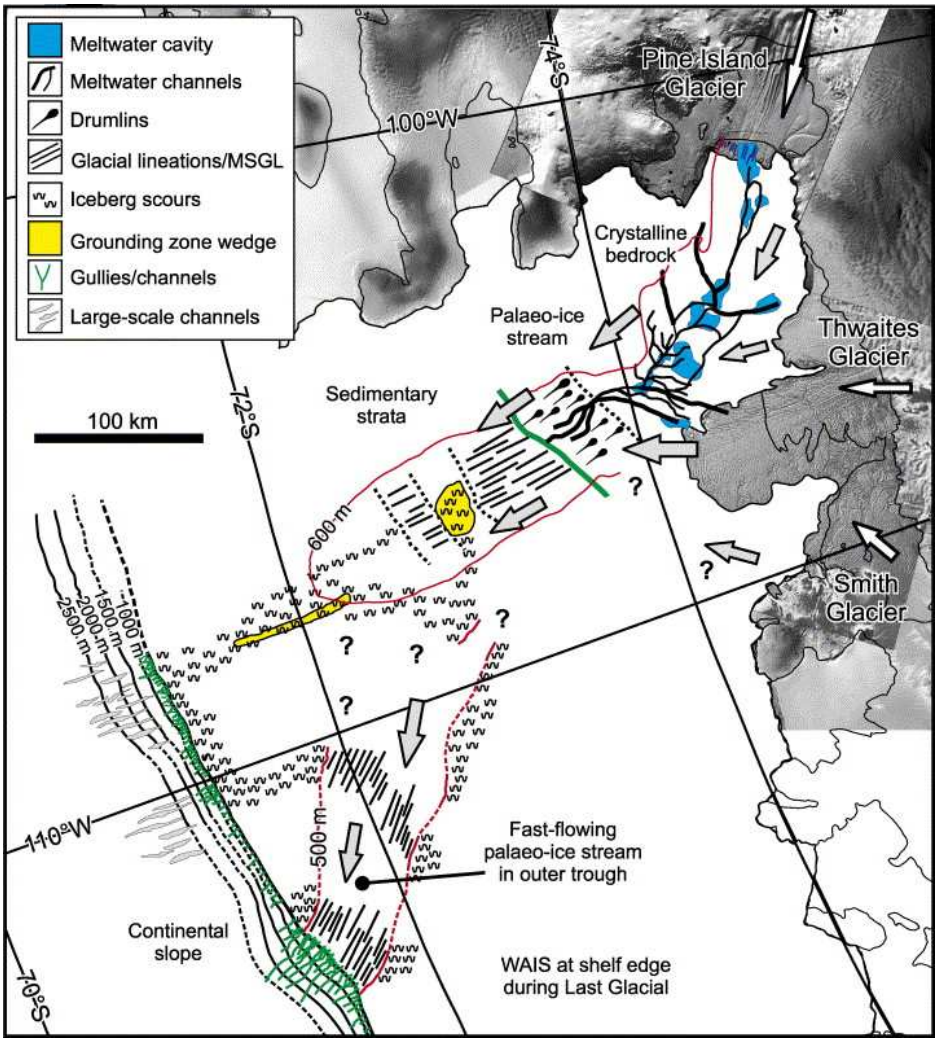

Figure 2.7: Summary of the principle morphological features imaged by surveys of the Amundsen Sea continental shelf region, from Evans *et al.* (2006).

uncertain. On the mid-shelf region, surveys show regularly-spaced furrows running perpendicular to the direction of ice flow (Jakobsson *et al.*, 2011). These have been interpreted as the footprint of a massive flotilla of icebergs as they temporarily grounded at low tide, and used as evidence for a massive ice shelf disintegration that occurred more than $\sim$ 12 000 years ago (Jakobsson *et al.*, 2011). On the mid- and outer-shelf, the presence of a series of sediment wedges indicate that ice retreat was periodically stabilised, probably by topographic highs in the underlying bedrock topography (Lowe and Anderson, 2002; Graham *et al.*, 2011). These wedges may have formed in as little as $\sim$ 100 years (Graham *et al.*, 2011), and so their presence remains consistent with a process of relatively rapid, if episodic, ice retreat.

2.3.2 Timing of Deglaciation in the Amundsen Sea

Determining the timing of post-LGM deglaciation across the Amundsen Sea continental shelf is important because it provides the wider context for the currently observed rates of ice retreat. Such a chronology can be determined by dating sediment samples retrieved from sites across the continental shelf. Ice retreat histories have been inferred from data acquired both from the eastern Amundsen Sea (along a cross-shelf sea floor trough originating from the Pine Island and Thwaites Glaciers) (Lowe and Anderson, 2002) and the western Amundsen Sea (along troughs originating from the Dotson and Getz Ice Shelves) (Smith *et al.*, 2011). In the eastern sector only sparse data are available, although the few dates that do exist are broadly consistent with evidence from the western sector (Lowe and Anderson, 2002; Smith *et al.*, 2011). In particular, no data exist within $\sim$ 200 km of the current position of the Pine Island Ice Shelf's calving front, and so the retreat rate immediately prior to the satellite era remains uncertain. In the western sector, a more extensive data record provides a more

detailed history. Based upon radiocarbon dating of samples from the western trough, Smith *et al.* (2011) estimate that ice retreat from the continental shelf edge commenced between $\sim$ 22 000 and 16 000 years ago. By $\sim$ 14 000 years before present (BP) the ice extent was limited to the mid-shelf, before retreating to within 10-12 km of the current ice shelf front by 13 000 - 10 000 years BP (figure 2.8).

Smith *et al.* (2011) used their chronological record to calculate average rates of ice retreat since the LGM (figure 2.8). Over the outer part of the continental shelf the rate of ice retreat was relatively slow (mean rate of $\sim$ 20 m/yr). These rates increased to 140-400 m/yr as the ice sheet retreated across the inner ice shelf. This increase in retreat rate coincides with a region of deepening bedrock (i.e. an increase in the landward-sloping gradient), which is consistent with the marine instability hypothesis. Additionally, the retreat broadly coincides with the timing of Melt Water Pulse 1a, and so it is possible that a sudden rise in sea level may have helped to drive accelerated retreat across the inner shelf. Over the past $\sim$ 10 000 years, as the ice sheet reached its current position, the retreat rate slowed again to an average of $\sim$ 7 m/yr.

Comparing past and present retreat rates suggests that the current retreat rate of the Pine Island Glacier (1.2 $\pm$ 0.3 km/yr (Rignot, 1998)) is anomalously high compared to the mean ice sheet retreat rates across the Amundsen Sea continental shelf since the LGM (figure 2.8). The recent retreat rate of Thwaites Glacier (0.4 $\pm$ 0.1 km/yr (Rignot, 2001)) is broadly comparable to the maximum historical retreat rate estimated by Smith *et al.* (2011). The past rates of retreat determined by Smith *et al.* (2011) are, however, only long term averages and may encompass short periods of more rapid deglaciation, such as currently experienced by the Pine Island Glacier.

Satellite observations show that glaciers draining the Amundsen Sea Sector of

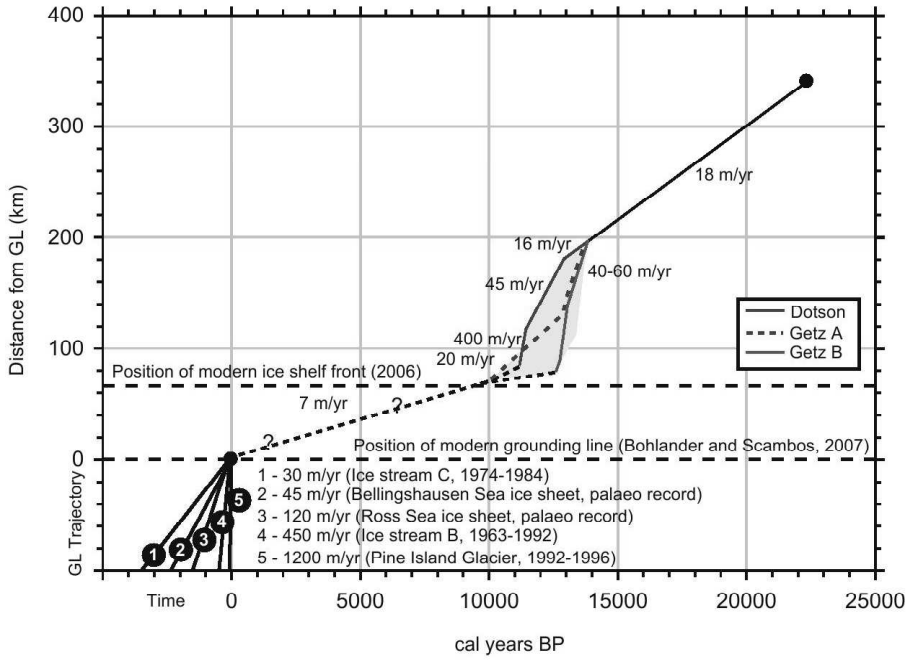

Figure 2.8: Retreat trajectory for the deglaciation of the WAIS in the western Amundsen Sea, from Smith *et al.* (2011). Average retreat rates are shown together with the trajectory of a range modern and palaeo retreat rates (lines numbered 1-5) for Ice Stream B and C, Pine Island Glacier and ice draining into the Bellingshausen Sea. Grey shading represents the range of rates estimated for the mid-inner shelf.

the WAIS are undergoing rapid change, and are currently retreating at rates far higher than the long term average since the LGM (Rignot, 1998; Smith *et al.*, 2011). However, because of the limited temporal resolution of the historical record in the Amundsen Sea, it is unclear whether current rates have been matched in the past, albeit over short time periods, or whether they are uniquely a recent phenomenon. As such, it is difficult to judge the significance of current behaviour solely from these observations, without additionally understanding the processes driving change. These processes are addressed in the following section.

2.4 The Coupled Ice-Ocean System

Observations and modelling studies agree that the ocean plays a key role in driving the current large mass imbalance in the Amundsen Sea Sector of the WAIS (Rignot, 1998; Payne *et al.*, 2004; Shepherd *et al.*, 2004; Walker *et al.*, 2007; Joughin *et al.*, 2010). Contemporary ocean forcing has the potential to (1) accelerate the long term decline of the ice sheet, and (2) push ice retreat beyond bedrock highs which may otherwise stabilise retreat (*c.f.* the instability hypothesis (Schoof, 2007)). Furthermore, the ocean can exhibit short-term temporal variability (compared to bedrock topography for example), and thus drive relatively fast changes to the ice sheet. Ocean forcing is of particular importance in the Amundsen Sea sector, because of the presence of relatively warm ocean waters flowing into the cavities beneath ice shelves. These drive high rates of ice shelf basal melting near the grounding line. Several mechanisms have been suggested to link enhanced basal melt to an increase in ice discharge across the grounding line. These include (1) a reduction in basal drag as more ice loses contact with the bedrock, either through the thinning of the ice shelf / ice plain (Rignot, 2002b; Payne *et al.*, 2004) or by the direct melting of grounded ice (Schoof, 2007), or (2) an increase in longitudinal stresses across the grounding

line, as melting steepens the base of the ice shelf, and thus increases driving stresses near to the grounding line (Schoof, 2007).

Given the significance of the ocean influence, an adequate explanation of the evolution of glaciers draining into the Amundsen Sea requires that they are treated as part of a coupled ice-ocean system. This in turn demands knowledge relating to the properties and behaviour of the ocean, and the interactions that occur between ice shelves and the ocean. In the remainder of this section I review these topics. I begin with a description of the oceanography of the Amundsen Sea. I then turn to the sub-ice shelf cavity and give an overview of the generalised cavity system, describing both ocean circulation and the mass exchanges that occur at the ice-ocean interface. I then focus specifically upon measurements of basal melting beneath ice shelves in the Amundsen Sea. Finally, I widen the discussion to consider other effects of the ocean upon ice shelves, as these will be of importance in later chapters.

2.4.1 Amundsen Sea Oceanography

The likelihood that ocean conditions are driving contemporary glaciological change in the Amundsen Sea Sector of the WAIS has focused interest on ocean processes in this region. In this section I give an overview of the current understanding of these processes, as provided by oceanographic data and modelling studies.

Oceanographic Modelling of Amundsen Sea Circulation

The Antarctic continent is surrounded by the Antarctic Circumpolar Current (ACC), a vast ocean current that circulates eastwards around the globe (figure

2.9). In the Amundsen Sea, this current passes close to the continental shelf break, allowing relatively warm ACC water that resides at depth (Circumpolar Deep Water (CDW)) to flow on to the continental shelf via depressions in the continental shelf break (Walker *et al.*, 2007). This water is typically at least 2°C warmer than water found at other locations on the continental shelf and 3°C warmer than the *in situ* melting point (Jacobs *et al.*, 1996). As such, it is sufficiently warm to cause high rates of ice-melting should it cross the relatively narrow continental shelf and reach the underside of ice shelves. On the continental shelf of the Amundsen Sea there is a clockwise circulation of surface waters (Grotov *et al.*, 1998; Assmann *et al.*, 2005), with coastal waters driven westwards by easterly coastal winds (figure 2.10).

Oceanographic Surveys in the Amundsen Sea

Ship-based oceanographic surveys are sparse in the Amundsen Sea, because of its remote location and perennial sea-ice cover. In recent years, as it has become clear that the ocean may be driving rapid glaciological change, there has been an increase in survey activity. In 1994, the first surveys across a deep channel running along the front of the Pine Island Glacier Ice Shelf were made (Jacobs *et al.*, 1996). Basal melt rates were found to be 5-50 times higher than at other ice shelves around Antarctica, as a result of the intrusion of CDW into the cavity beneath the ice shelf. These observations provided evidence that this region may provide a substantial deficit to the AIS mass balance.

Subsequent surveys have focused upon providing both topographic detail of the sea floor (Lowe and Anderson, 2002; Evans *et al.*, 2006) and further details of the delivery of ocean heat to the base of ice shelves (Walker *et al.*, 2007; Wahlin *et al.*, 2010). Sea floor surveys have identified deep sea floor troughs, originating from paleo-ice streams (Dowdeswell *et al.*, 2004), that run across the relatively

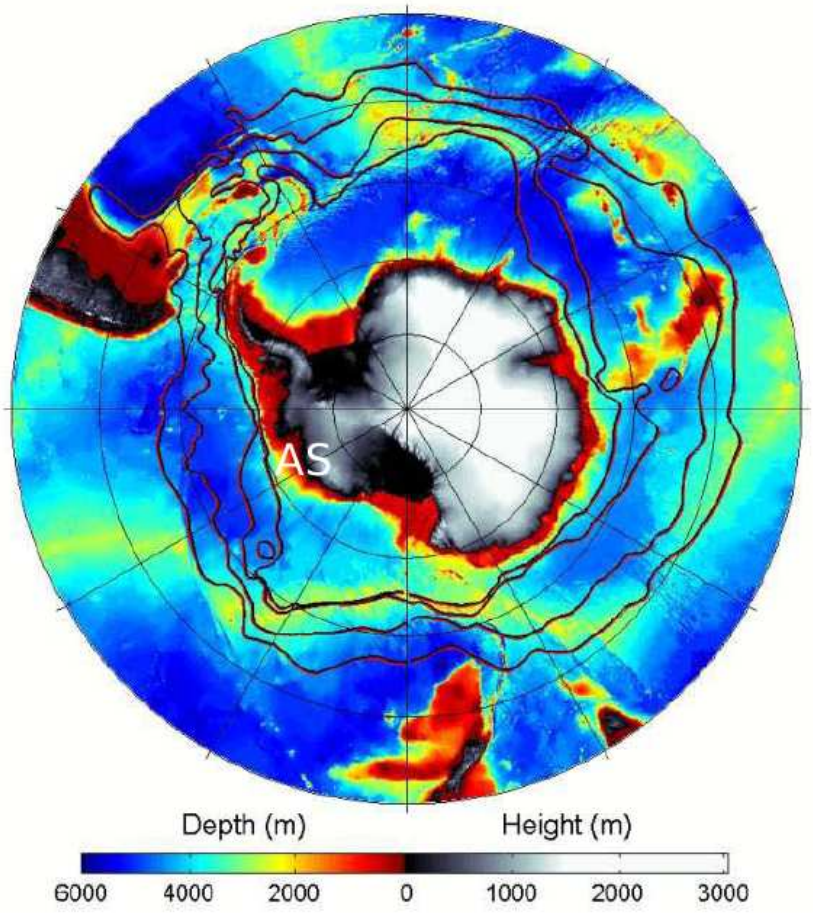

Figure 2.9: The location of the Antarctic Circumpolar Current (ACC), adapted from Turner *et al.* (2009). The ACC lies between the inner and outer red lines; other red lines indicate positions of other oceanic fronts. Colour scale shows surface topography; *AS* marks the Amundsen Sea Sector.

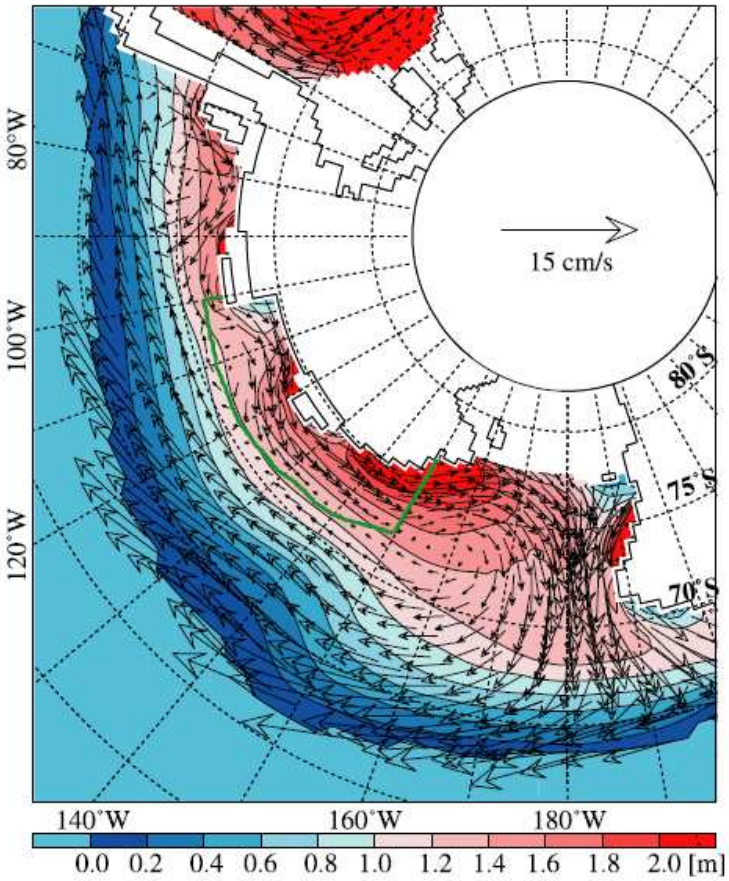

Figure 2.10: Modelled mean winter sea ice drift velocities around the WAIS, from Assmann *et al.* (2005). Arrows indicate velocity vectors, and the colour scale indicates sea ice thickness. The Amundsen Sea is roughly bounded by 90°W and 125°W.

narrow continental shelf. These features provide pathways along which dense CDW can access sub-ice shelf cavities and drive high rates of ice shelf basal melting. Oceanographic surveys conducted in 2003 and 2008 have provided details of the properties of water flowing through two of these large troughs (Shoosmith and Jenkins, 2006; Walker *et al.*, 2007; Wahlin *et al.*, 2010) (figure 2.11). These confirm the presence of warm CDW residing at depth, and show spatial variation in water column composition between sites. This variability is, in part, due to the outflow of cooler, less dense melt water from beneath ice shelves. The water passing through the two surveyed troughs (Walker *et al.*, 2007; Wahlin *et al.*, 2010) contains sufficient heat to account for all current mass loss from glaciers draining into the Amundsen Sea (Rignot and Thomas, 2002), under the assumptions that (1) the surveys were representative of annual and inter-annual heat flow variability, and (2) all available heat reached the base of ice shelves and was used to melt ice. These assumptions are, however, difficult to validate from the limited number of observations that exist.

2.4.2 Ocean Circulation and Melting in the Ice Shelf Cavity

General Overview of the Cavity System

Beneath an ice shelf is a body of water whose properties are determined by the processes of melting and freezing at the base of the ice shelf and by the exchange of water with the open ocean. At different locations around Antarctica, the inflowing water entering the cavity originates from different sources, leading to a distinction between so called *cold water* and *hot water* ice shelves. The Ross and Weddell seas are home to cold water ice shelves. Here, the primary water source for ice shelf melting is High Salinity Shelf Water (HSSW). Strong katabatic winds blow sea ice off shore, exposing coastal waters to the cold air. Consequently

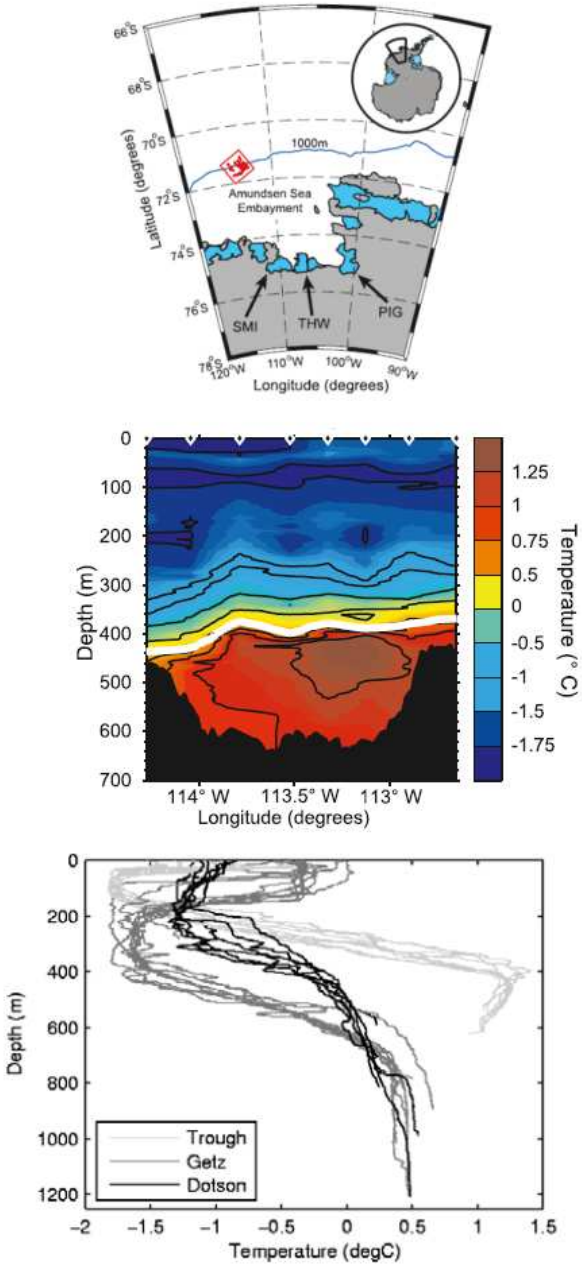

Figure 2.11: Profiles of Amundsen Sea ocean temperature in 2003, from ship surveys of a shelf-break trough and from the fronts of the Dotson and Getz Ice Shelves. Top panel, location map; red box marks trough survey. Middle panel, data across the shelf-break trough, from Walker *et al.* (2007); white line marks upper boundary of CDW. Bottom panel, comparison of water temperature profiles from the shelf break and from the fronts of the Dotson and Getz Ice Shelves, from Shoosmith and Jenkins (2006). Water column properties vary significantly between the shelf break and the coastline, indicative of the presence of increased melt-water in the water column close to the ice shelves.

sea ice forms, which through the process of brine rejection increases the salinity, and hence density of the surface waters. These waters sink and then flow along the inward-sloping seabed to the grounding lines beneath the ice shelves. The increase in pressure with depth suppresses the freezing point, and so these waters have sufficient heat to melt ice where they contact the ice shelf base. Because of the mechanism of HSSW formation, the maximum temperature of HSSW is limited to the surface freezing point. The heat available for melting is therefore dependent upon the influx of HSSW, which is governed by the rate of sea ice formation, and hence the strength of katabatic winds. At hot water ice shelves, such as those in the Amundsen Sea, there is an alternative ocean source of heat. Here, warm, dense CDW which normally resides at depth off the continental shelf, breaches the shelf break and flows along the deep troughs in the continental shelf. The temperature of CDW is typically 3-4°C above the in situ melting point and is therefore capable of driving high rates of basal melting where it meets the base of an ice shelf. As with cold water ice shelves, it has been suggested that the flux of CDW onto the continental shelf is controlled by surface winds, although this time operating at the continental shelf edge to drive CDW upwelling onto the shelf (Thoma *et al.*, 2008).

Regardless of the origin of the warm water flowing into the ice shelf cavity, the subsequent melting that occurs where it contacts the ice drives a thermohaline circulation of water in the ice shelf cavity. Melting near the grounding line (the deepest part of ice shelf) causes a cooling and freshening of the water, which decreases its density. This buoyancy drives a turbulent plume of Ice Shelf Water (ISW), which flows along the base of the ice shelf as it strives to reach shallower depths and neutral buoyancy (Payne *et al.*, 2007; Jenkins *et al.*, 2010). As it flows, the ISW plume interacts with the ice above, driving melting or refreezing, according to its depth, temperature and salinity. Where refreezing occurs, brine rejection causes a densification of the water, allowing it to sink and once again

acquire the potential to melt ice at depth. At the base of the plume, the turbulent flow entrains the warmer water below, providing a further source of heat to melt ice. The rate at which water is entrained is dependent upon the velocity of the plume, which in turn is determined by the density contrast between the plume and the surrounding water. Consequently the entrainment of warmer water, and thus the continued supply of heat for melting, lessens as the plume rises along the underside of the ice shelf. As the plume travels towards its exit from beneath the ice shelf, its path is affected by both the topography of the underside of the ice shelf and the Coriolis effect (Payne *et al.*, 2007).

In addition to the basic thermohaline-driven system described above, ocean tides can enhance circulation and melting in the sub-ice shelf cavity, by increasing the flux of inflowing warm water (Makinson *et al.*, 2011). Tides can also increase the turbulent mixing of the water column and thus the heat available to melt ice. At locations where tidal velocities are larger than those generated by the thermohaline circulation, tidal forcing can become the dominant process governing cavity circulation and melting. This is likely to be most apparent at cold water ice shelves which exhibit a weaker thermohaline circulation, and also at locations that experience large ocean tides, such as the Weddell Sea. In rare cases, tidal mixing can completely homogenise the water column, thus destroying the thermohaline circulation (Holland *et al.*, 2008).

Ocean-Driven Melting Beneath Amundsen Sea Ice Shelves

To better understand the role of the ocean in driving glaciological change in the Amundsen Sea sector of the WAIS requires data detailing interactions at the ice-ocean interface. It is difficult and expensive to directly measure melting at the base of ice shelves and so indirect methods, using satellite data and assumptions of mass conservation, have been developed. Rignot (1998) differenced

ice flux estimates from two across-glacier transects to estimate that, between the grounding line and the ice front, the Pine Island Glacier ice shelf had a mean basal melt rate of 24 ± 4 m yr^{-1}. This calculation was based on the assumption that the ice shelf was in steady state (i.e. not gaining or losing mass). The basal melt rate was found to be substantially higher (44 ± 6 m yr^{-1}) immediately seaward of the grounding line (Rignot, 1998; Rignot and Jacobs, 2002), and an order of magnitude higher than basal melt rates found underneath other Antarctic ice shelves (Jacobs *et al.*, 1996; Rignot and Jacobs, 2002). Rignot and Jacobs (2002) extended the same method to estimate steady-state basal melting immediately downstream of the grounding lines of other Amundsen Sea ice shelves, recording values for the Thwaites (34 ± 9 m yr^{-1}), Dotson (20 ± 5 m yr^{-1}), Crosson (18 ± 8 m yr^{-1}) and Getz (19 ± 6 m yr^{-1}) ice shelves. Shepherd *et al.* (2004) used these estimates, in conjunction with altimeter-derived ice shelf thinning rates and information regarding the likely spatial distribution of basal melting (Joughin *et al.*, 2003), to calculate non-steady-state basal melt rates, averaged over the entire ice shelf (figure 2.12). Shepherd *et al.* (2004), in agreement with Rignot and Jacobs (2002), found that rates of melting underneath the Pine Island and Thwaites ice shelves were substantially higher than underneath other ice shelves in the Amundsen Sea. Both studies found that basal melt rates were positively correlated with nearby estimates of ocean temperature (Giulivi and Jacobs, 1997). This further supported the argument that current glaciological change in this region is being driven by warm ocean waters.

2.4.3 Tidal Influence on Ice Shelf Dynamics

Earlier in this chapter I discussed the effect of tides upon the ocean circulation within the ice shelf cavity. When considering the influence of tides within a coupled ice-ocean system, tides have a more obvious impact; driving the

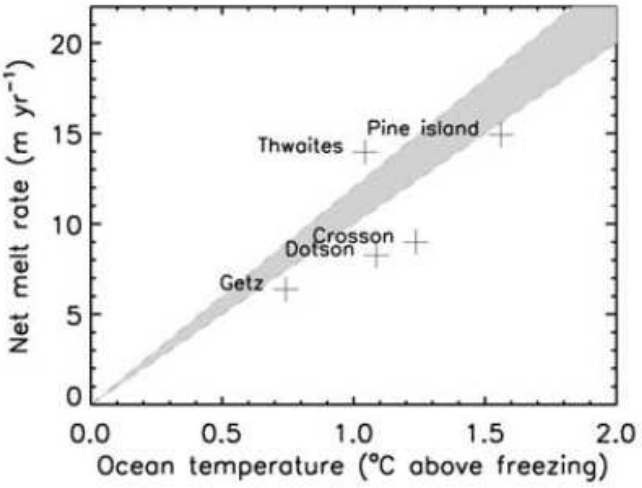

Figure 2.12: Estimated net melt rate at the base of Amundsen Sea ice shelves versus ocean temperature above *in situ* freezing, from Shepherd *et al.* (2004). Net melt rate includes both steady-state rate computed from equations of mass conservation, and thinning rate determined from altimetry data. The shaded area bounds empirical relationships for ice melting determined for a selection of Antarctic glaciers (lower curve, from Rignot and Jacobs (2002)) and laboratory samples (upper curve, from the data of Russel-Head (1980)).

displacement of the ice shelf as it responds to the tidal motion of the ocean. The tidally-driven movement of water in and out of the ice shelf cavity induces an oscillation in the vertical position of the ice shelf. Additionally, tides can influence the motion of an ice shelf in the horizontal plane, in both the longitudinal (aligned with flow) and transverse (perpendicular to flow) directions. Several studies have used GPS data to resolve these processes. The tidal effect on longitudinal displacement is to produce a modulation in the flow speeds of the ice shelf. Through longitudinal coupling, this effect propagates upstream of the grounding line, so that both ice shelf and inland ice stream experience a tidal modulation of flow at a range of frequencies (Doake, 2002; Anandakrishnan, 2003; Gudmundsson, 2006; Murray *et al.*, 2007). Various phase lags between the tidal displacement and ice velocity oscillations have been recorded at different ice shelves, and have led to a range of mechanisms being proposed to explain the modulation of ice flow. These include the reduction in basal drag experienced by the ice shelf as pinning points

become partially ungrounded, increases in water pressure beneath the grounded ice stream and variations in the force exerted by tidal currents passing across the rough underside of the ice shelf.

In addition to the tidally-driven modulation of ice shelf flow, oscillations in the transverse direction have also been recorded at the Brunt Ice Shelf (Doake, 2002) and the Mertz Glacier Ice Tongue (Legresy *et al.*, 2004). The exact causal mechanism is not well understood, but it is possible that this effect results from tidal currents acting on the rough base of the ice shelf / ice tongue. In both cases, the floating ice is unconstrained by land at its lateral margins and so it is plausible that tidal currents flowing along the coast could pass in a transverse direction underneath the floating ice, thus producing the observed transverse motion.

Observations of the complex 3-d response of ice shelves to tidal forcing and the associated modulation of inland ice flow highlight the important role ocean tides play in controlling the short-period dynamics of ice shelves and the ice streams that feed them. In studying the longer term evolution of these systems, such as the changing dynamics of glaciers draining the Amundsen Sea Sector of West Antarctica, it is therefore important to account for these tidal effects.

2.5 Spatial and Temporal Variability in the Amundsen Sea

In this chapter I have detailed a complex picture of glaciological behaviour in the Amundsen Sea sector of the WAIS. It is likely that the ice sheet is responding to a range of forcing mechanisms which operate over varying timescales. Furthermore, there is spatial variability in the response of individual glacier catchments, likely due to a combination of the subtleties in the forcing mechanisms and the different

geometries of each catchment. Separating the relative influence of these factors is challenging, yet it is essential for understanding the processes driving recent glaciological change.

2.5.1 Causes of Temporal Glaciological Variability

As we have seen, ocean processes may control much of the temporal glaciological variability in the Amundsen Sea Sector of the WAIS. However, ship-based surveys provide only spatially and temporally sparse details of the variability in the ocean properties of the Amundsen Sea. As a result, they cannot alone adequately resolve the causes of the glaciological change witnessed in the region. For example, we cannot determine the extent to which temporal changes in ocean properties (e.g. CDW warming or circulation changes) have driven glacier evolution. It remains uncertain how spatially and temporally representative the sparse oceanographic observations are, and as a result their interpretation and significance is unclear.

In view of the limited temporal record provided by oceanographic surveys, modelling studies have been used to simulate oceanographic variability in the Amundsen Sea. To investigate the role of CDW variability, Thoma *et al.* (2008) conducted oceanographic model simulations for the period 1980-2004. This study found both seasonal and inter-annual variations in CDW intrusion onto the continental shelf, and in broad terms, the modelled influx of CDW correlated well with periods of glaciological stability and change (Rignot, 1998; Joughin and Padman, 2003; Shepherd *et al.*, 2004). These model simulations indicated that temporal variability in CDW influx was related to regional wind forcing, with stronger offshore westerly winds driving increased upwelling of CDW onto the continental shelf.

The work of Thoma *et al.* (2008) suggests a possible indirect link between glaciological change in the Amundsen Sea Sector and atmospheric forcing. Decadal-scale atmospheric variability may drive ocean variability, which in turn could affect glacier dynamics. Whether such changes can be attributed to anthropogenic forcing or merely result from natural decadal variability in weather patterns remains uncertain. For example, there is evidence that anthropogenically-driven climate warming and stratospheric ozone depletion may have caused a southward shift, and strengthening, in the westerly winds that drive the ACC (Thompson and Solomon, 2002; Fyfe and Saenko, 2006). This is turn may have driven the ACC south, bringing it closer to the continental shelf break and increasing CDW delivery onto the Amundsen Sea continental shelf. Such behaviour would be consistent with observations of ACC warming in recent decades (Gille, 2002), but at present the reality of such a mechanism driving glaciological change in the Amundsen Sea remains speculative.

2.5.2 Causes of Spatial Glaciological Variability

Alongside the search to explain temporal glaciological variability, lies a need to explain the varying behaviour of different glaciers draining into the Amundsen Sea. What controls the spatial variability in recent rates of ice thinning and retreat? Bedrock topography is likely to have a strong influence upon glacier behaviour in several ways; (1) ocean bathymetry will determine the volume of CDW reaching each ice shelf and, in part, the mixing that occurs underneath each ice shelf, (2) grounding line depth will determine the availability of ocean heat for ice shelf melting (via the melting point dependency upon pressure), and (3) subglacial topography will modulate the glaciological response to any forcing (e.g. bedrock slope determines the sensitivity of a glacier's retreat rate to its thinning rate). It may be no coincidence that the glaciers that have undergone the greatest

acceleration (Pine Island and Smith) both sit in deep, narrow subglacial troughs (see figures 2.2 and 2.3) (Vaughan *et al.*, 2006; Holt *et al.*, 2006). The relative influence of these factors upon ice dynamics is not, however, well understood.

Additionally, the influence of bedrock topography has important implications for the wider evolution of the ice sheet in this region. In particular, geometrical differences between individual catchments (figures 2.2 and 2.3) are likely to affect the outcome of retreat in each catchment. The Pine Island Glacier sits in a confined inward-sloping bedrock trough, which extends $\sim$ 200 km inland of the grounding line (figure 2.2). It therefore seems plausible that unstable retreat could lead to an ungrounding and retreat of the main Pine Island Glacier but not to the widespread collapse of the WAIS. The Smith Glacier similarly sits in a confined trough which is smaller in length than the Pine Island Glacier trough. In contrast to these geometrical configurations, the Thwaites Glacier lies on a topographically-unconstrained inward-sloping bed (figure 2.3), which gives access to the deep interior of the WAIS. As such, retreat of the Thwaites Glacier has a greater potential to initiate a wider WAIS collapse. Thus glaciers which sit in deep confined troughs may provide a greater contribution to sea level in the short term, but it is a retreat of the catchments which lie in more open topgraphic basins that may pose the greatest risk to the long term stability of the WAIS as a whole.

2.6 Summary of Current Understanding

The following points broadly summarise our current understanding of the behaviour of glaciers draining into the Amundsen Sea Sector of the WAIS:

- Satellite observations show that glaciers draining into the Amundsen Sea are currently suffering high rates of mass loss.
- Oceanographic surveys, satellite data and modelling studies implicate warm CDW as the principle driver of this glaciological imbalance.
- Oceanographic models suggest that decadal atmospheric variability may regulate CDW delivery onto the continental shelf, and so be ultimately responsible for temporal variability in glaciological behaviour.
- Surveys suggest that bedrock topography plays a role in controlling the spatial variability of glacier behaviour.

These points demonstrate a broad understanding of what drives change in the glaciological system in the Amundsen Sea, but at present the details required to be able to predict its future evolution are lacking. Observations and models have identified multiple factors which may contribute to the spatial and temporal variability of glaciological change in this region. These include bedrock topography, ocean circulation, the spatial and temporal variability of ocean properties, and temporal variability in atmospheric conditions. Because of current limits in understanding, arising from sparse observations and model limitations, the relative importance of these factors remains uncertain. Consequently, separating the effect of factors that could change over decadal timescales (e.g. CDW inflow), and indeed could be influenced by humans, from those which will not (e.g. bedrock topography) is difficult.

To address these limitations, and to understand the wider implications of ongoing changes for the future evolution of this region, requires the extension of existing ice-dynamic models to include the oceanic and atmospheric domains. These models must run at the spatial and temporal resolution required to accurately simulate the complex interactions between the ice, the ocean and the atmosphere.

The development of such models requires similar scale observations, to provide constraint and validation. In remote regions such as the Amundsen Sea Sector of the WAIS, satellites are well suited to providing these observations.

Chapter 3

Review of Methods

In this chapter I review the methods employed in this thesis, so as to provide a brief history of the development of the methods that I use and extend, and also to place these methods within the wider context of current research. Further detailed descriptions of the processing methods are given in each of the results chapters, which are presented as journal articles, and so not repeated here.

3.1 Bathymetric Prediction from Sparse Ship Surveys and Marine Gravity Data

Accurate bathymetric maps are vital for numerous applications in the fields of geology, oceanography, glaciology and biology. Around Antarctica, bathymetric data provide evidence of past ice sheet behaviour and extent (Lowe and Anderson, 2002; Evans *et al.*, 2006), and of current delivery of ocean heat to the base of ice shelves (Walker *et al.*, 2007; Thoma *et al.*, 2008). However, the oceans are vast and ship-based surveys are time-consuming and expensive. As a result, much

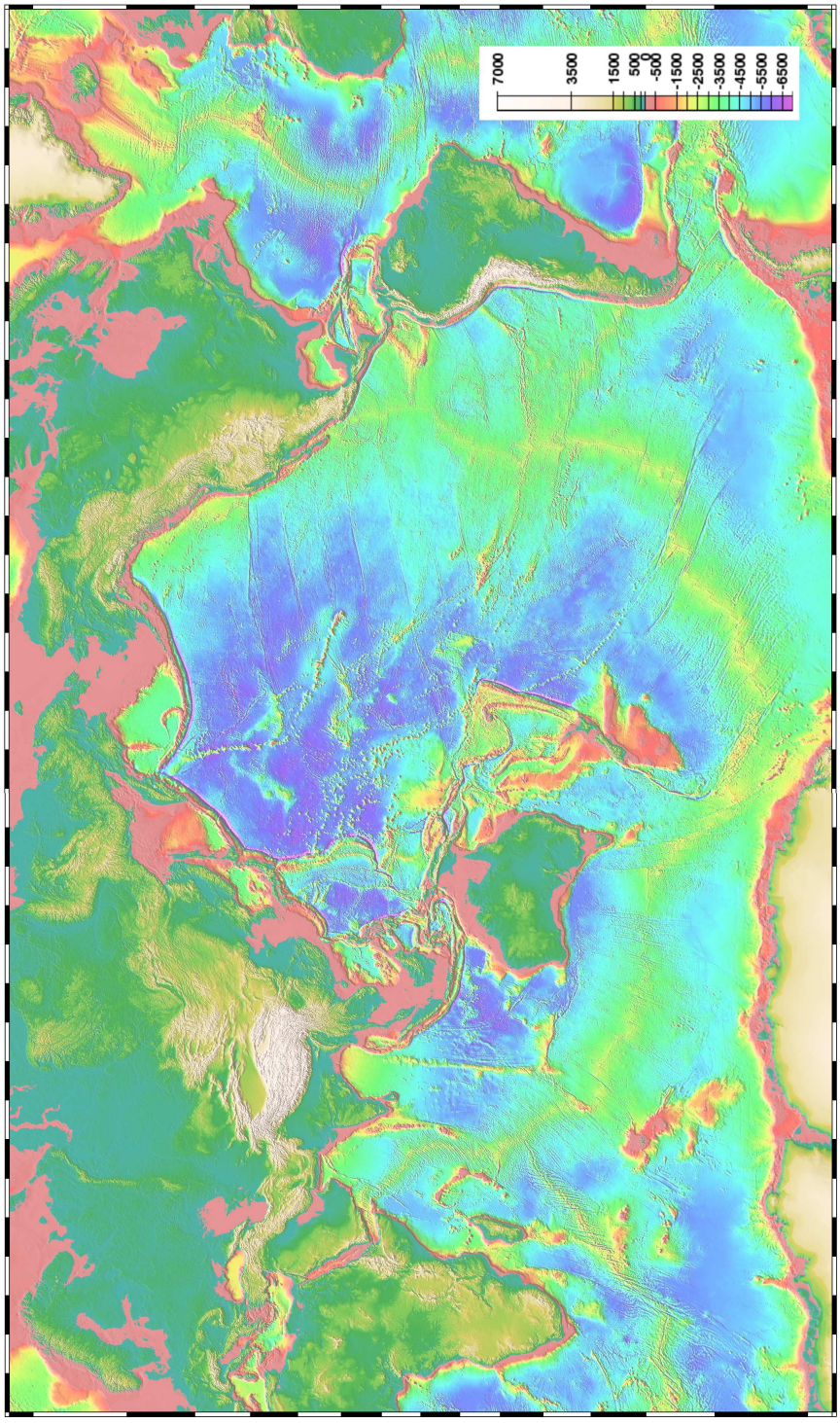

Figure 3.1: Bathymetric prediction from satellite altimetry and ship-based depth soundings, from Smith and Sandwell (1997). Bathymetric coverage does not extend beyond 72°S, and so the coastal waters of the West Antarctic Ice Sheet remain unmapped.

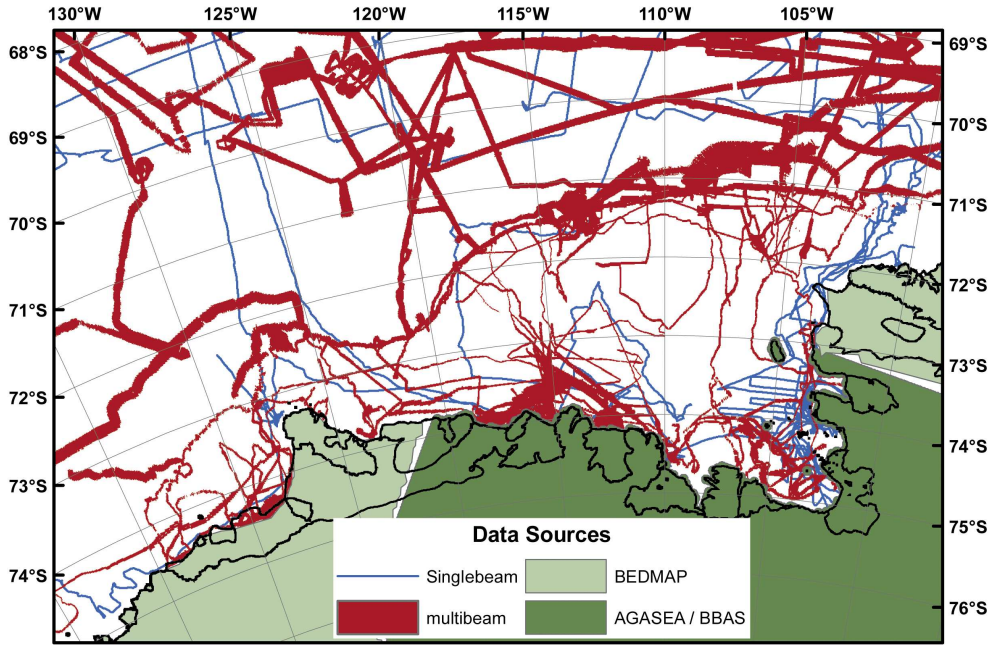

Figure 3.2: Distribution of ship-based surveys in the Amundsen Sea Sector of West Antarctica, from Nitsche *et al.* (2007). Bathymetric detail is still lacking over a large proportion of this region.

of the ocean remains unsurveyed by ships, and maps based solely upon these sparse data must resort to extensive interpolation to fill unsurveyed regions. This is particularly true in the remote Southern Ocean. In the 1970's, several studies (Dorman and Lewis, 1970; Lewis and Dorman, 1970; McKenzie and Bowin, 1976) demonstrated that marine gravity anomalies were correlated with sea floor topography over a limited range of length scales. Gravity anomalies cause distortions in the geoid, which can be mapped from measurements of sea surface slope. With the advent of satellite-based altimeters came the potential to acquire such data over a large proportion of Earth's oceans, and so provide bathymetric detail in the vast regions devoid of ship-based surveys (Dixon *et al.*, 1983). Following these proof-of-concept studies, Smith and Sandwell (1994, 1997) developed a global-scale bathymetric map, using a combination of sparse ship surveys and gravity data derived from the altimeters on-board the Seasat, Geosat and ERS-1 satellites (figure 3.1).

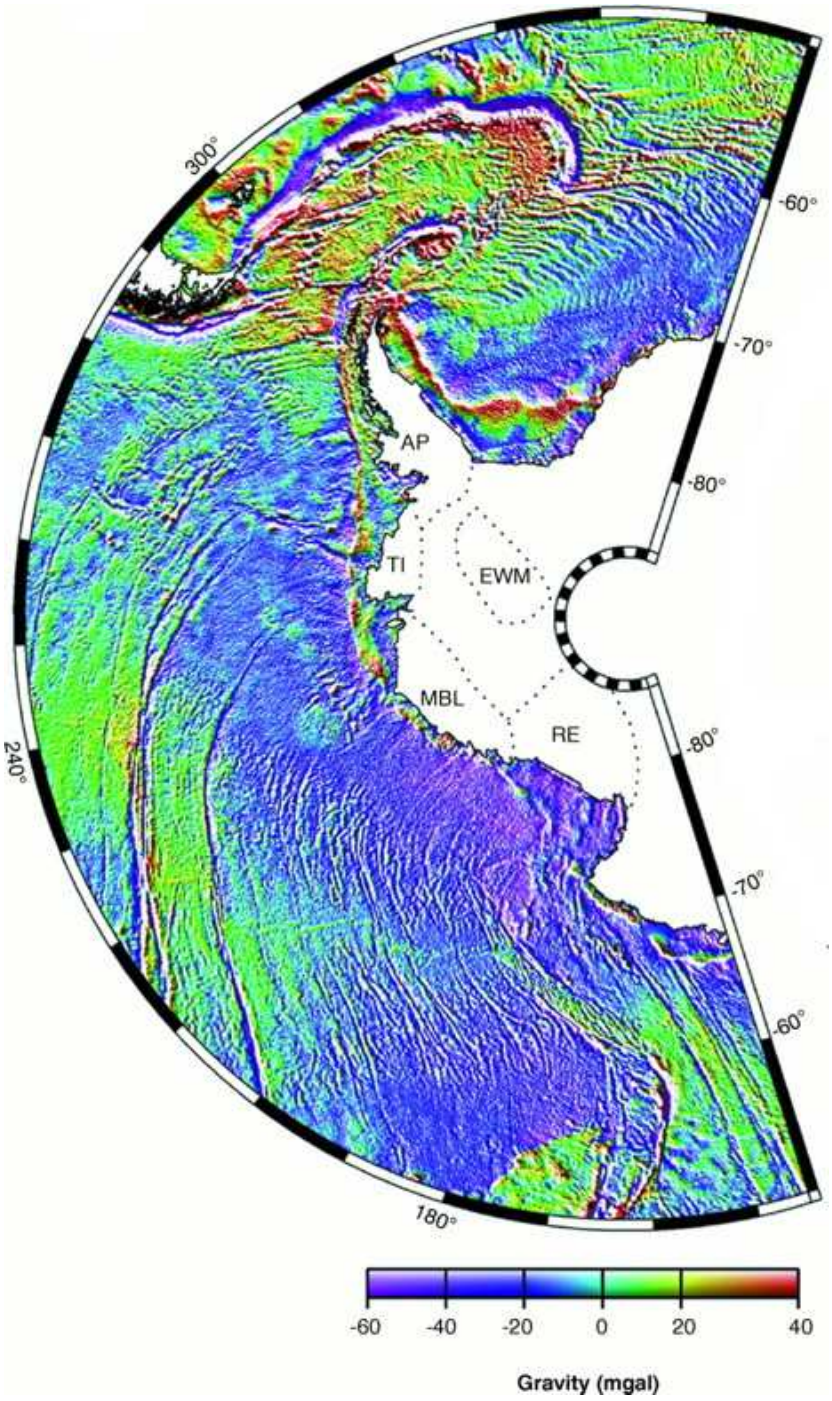

Figure 3.3: Marine gravity field adjacent to West Antarctica, determined from altimeters on-board the ERS-1 and Geosat satellites, from McAdoo and Laxon (1997). West Antarctic crustal blocks shown are Antarctic Peninsula (AP), Thurston Island (TI), Ellsworth-Whitmore Mountain (EWM), Marie Byrd Land (MBL), and the Ross Sea Embayment (RE).

This bathymetric solution (Smith and Sandwell, 1994, 1997) did not, however, cover Antarctica's coastal waters south of 72°S, because the presence of sea ice made gravity retrieval unreliable in this region. Consequently, polar bathymetric maps (Nitsche *et al.*, 2007) are still based solely on ship-based surveys, which because of the difficulty and expense of accessing such remote regions, are relatively sparse (e.g. figure 3.2). As a result, much of the bathymetric detail required to understand the oceanic processes affecting AIS glaciological change is lacking. Several years after Smith and Sandwell (1994) published their bathymetric map, altimetry processing techniques were developed so that polar marine gravity could be resolved with confidence (McAdoo and Laxon, 1997; Laxon and McAdoo, 1994) (figure 3.3), albeit with lesser accuracy than was achievable over the open ocean. This has provided the potential for the method of Smith and Sandwell (1994) to be extended to add additional gravity-derived detail to polar bathymetric maps. Alongside any such attempt, is a need to assess the impact of reduced gravimetric accuracy on bathymetric prediction, and the viability of applying this technique to sparsely surveyed polar regions.

3.2 Tide Model Validation in Antarctic Waters

Signals arising from the ocean tide effect measurements of the Antarctic Ice Sheet made by a range of satellite sensors, including ice shelf thinning rates from altimetry (Shepherd and Peacock, 2003), ice shelf velocity from interferometric synthetic aperture radar (Goldstein *et al.*, 1993) and ice mass changes from gravimetry (Ray *et al.*, 2003). Tides also affect melting and re-freezing at the base of ice shelves (MacAyeal, 1984; Joughin *et al.*, 2003; Makinson *et al.*, 2011) and so the inclusion of accurate tidal forcing improves studies that model ice-ocean interactions. In all of these applications, tide models have been used to

simulate the effect of the tide, and so the accuracy of these studies is affected by the quality of tide model predictions.

In non-polar oceans, tide model accuracy is good - typically 2-3 cm (Andersen *et al.*, 1995; Shum *et al.*, 1997), primarily because models assimilate satellite data covering this area. The coastal waters of Antarctica, however, lie beyond the limits of these data and so, in combination with a lack of *in situ* tidal records, relatively shallow waters and sparse bathymetric data, they represent a much greater challenge for tide models. In this context, ascertaining the accuracy of tide models in Antarctic waters is an important task, yet it is hampered by the limited *in situ* data available for validation. King and Padman (2005) performed such a validation, based upon the data shown in figure 3.4, and estimated the accuracy of the best performing tide model to be $\sim$ 7.5 cm. However, the distribution of these tidal records around the Antarctic coastline was not uniform (figure 3.4). In particular, the data used to validate the tide models tended either to be situated close to the data assimilated into the models, or may themselves have been assimilated into the models. Consequently, this measure of tide model accuracy may not be representative of model accuracy at remote locations which are far from *in situ* records. In the absence of *in situ* data, remote sensing observations, and in particular interferometric synthetic aperture radar, can be used to assess tide model accuracy.

3.2.1 Validating Tide Models with Interferometric Synthetic Aperture Radar

For the last fifteen years, satellite-based Interferometric Synthetic Aperture Radar (InSAR) has provided precise, spatially extensive observations of ice motion (Goldstein *et al.*, 1993; Joughin *et al.*, 1995, 1996a; Kwok and Fahnestock, 1996; Rignot, 1996; Rignot *et al.*, 2008). InSAR measures differences in the phase of

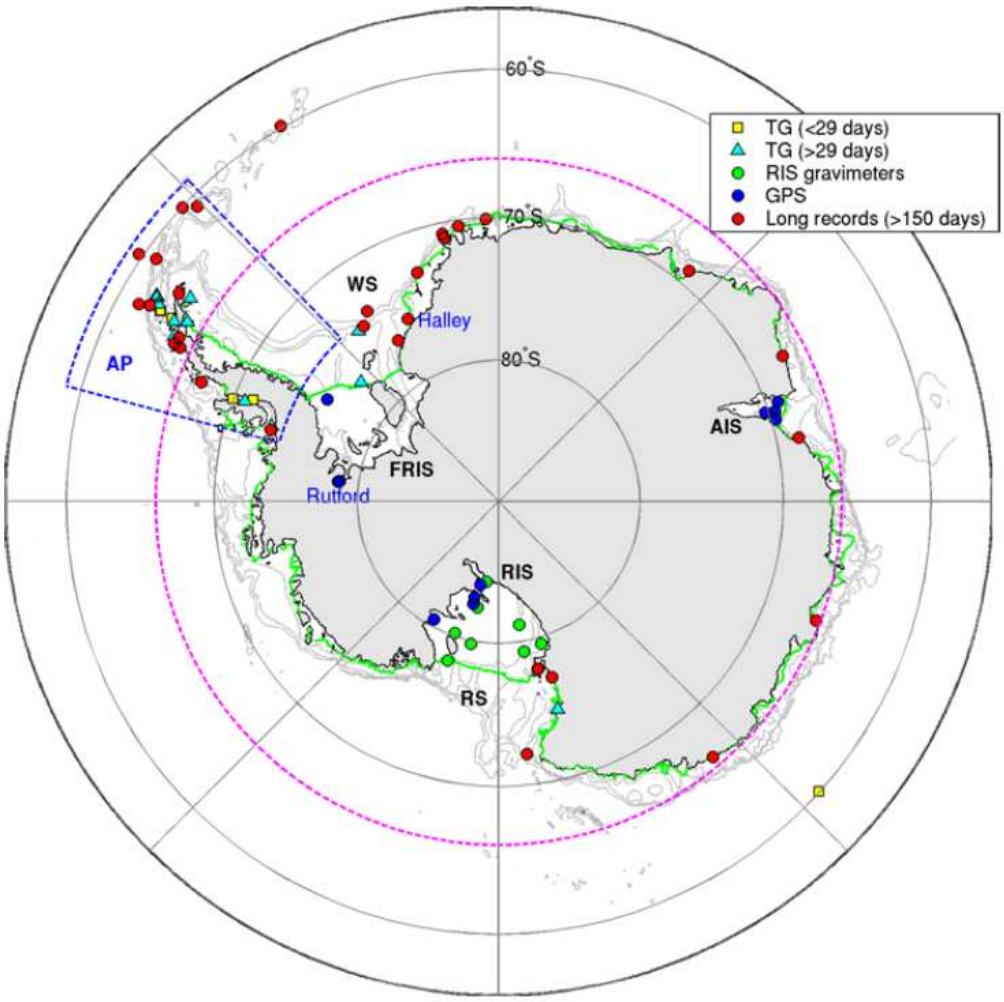

Figure 3.4: Distribution of *in situ* tidal records around Antarctica, from King and Padman (2005). *TG*, tide gauge; *WS*, Weddell Sea; *RS*, Ross Sea; *RIS*, Ross Ice Shelf; *FRIS*, Filchner-Ronne Ice Shelf; *AIS*, Amery Ice Shelf; *AP*, Antarctic Peninsula (encompassed by blue dashed line); pink dashed line indicates southerly limit of TOPEX/Poseidon altimetry commonly assimilated into tide models; green line indicates extent of floating ice; grey lines are bathymetric contours.

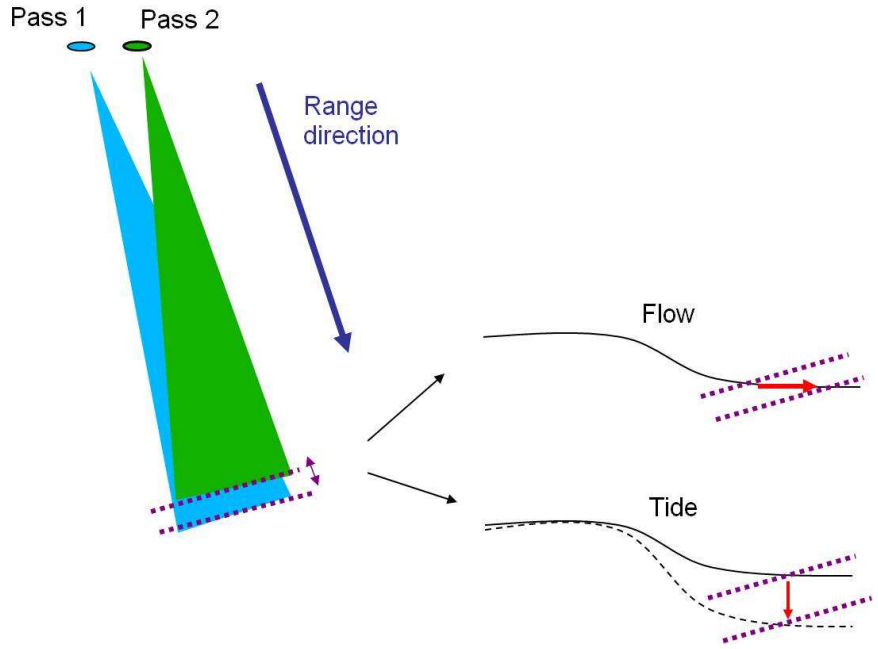

Figure 3.5: Diagram illustrating how horizontal (ice flow) and vertical (e.g. tidal) ice shelf motion both contribute to the range change detected by InSAR.

the signal recorded in pairs of SAR images, and converts these into changes in the distance between the satellite and the ice surface. These observations are used to estimate surface displacement in the satellite's viewing direction (*line of sight*), over the period of the interferometric acquisition, which is typically several days. The wavelength at which SAR's operate is well-suited to measuring centimetre-scale surface displacement via changes in phase, and so SAR's are capable of detecting surface height changes caused by ocean tides. InSAR cannot directly detect the tidal motion of the ocean surface because the water surface never remains sufficiently stable. However, an ice shelf does provide a surface which is often stable enough to allow InSAR to detect surface motion. To avoid directional ambiguities SAR's are pointed off nadir, and so the detected signal is sensitive to both horizontal and vertical motion. Consequently, InSAR displacement measurements of an ice shelf consist of components due both to ice flow (approximately in the horizontal plane) and the action of the ocean tide (Goldstein *et al.*, 1993) (figure 3.5). By differencing InSAR displacement

measurements (so called *differential InSAR*), the steady component of ice flow is removed and any non-steady motion isolated (Hartl *et al.*, 1994; Rignot, 1996; Schmeltz *et al.*, 2001) (figure 3.6). Under the assumption that all non-steady motion of an ice shelf is a vertical response to the ocean tide, this method has provided a means to estimate tidal displacement and validate tide model predictions. As described in section 2.4.3, observations have shown that not all tidally-driven ice shelf motion is in a vertical direction, and there is often also a component in the horizontal plane. Thus the signal recorded by InSAR and the tide model predictions are not entirely comparable. However, unlike the vertical component, tidal modulation of flow is a long wavelength signal, extending tens of kilometers inland (Gudmundsson, 2006) and so by measuring tidal displacement relative to grounded ice close to the grounding line, the effect of flow modulation can be minimised. InSAR observations have been used to evaluate tide models at several locations around Antarctica, including the Ross Ice Shelf (Padman *et al.*, 2003a), the Filchner-Ronne Ice Shelf (Hartl *et al.*, 1994; Rignot *et al.*, 2000) and the Pine Island Ice Shelf (Rignot, 2002a). At these locations, models have been able to produce the tidal signal recorded by differential InSAR with an accuracy of the order of 10 - 20 cm.

Whilst differential InSAR can be used to provide a general validation of a tide model, it only assesses a model's ability to reproduce the difference between two displacements, and not the ability of a model to simulate the tidal displacement itself (figure 3.7). This method does not, therefore, quantify the accuracy with which a model can simulate the tidal signal recorded within an interferogram. Consequently, differential InSAR cannot quantify the effect of tide model error on InSAR-based ice shelf velocity estimates that utilise tide model predictions to remove the tidal signal. Furthermore, these methods have not determined what proportion of the mismatch between tide model predictions and observations is due to tide model inaccuracies, and what part is due to other non-tidal, non-steady

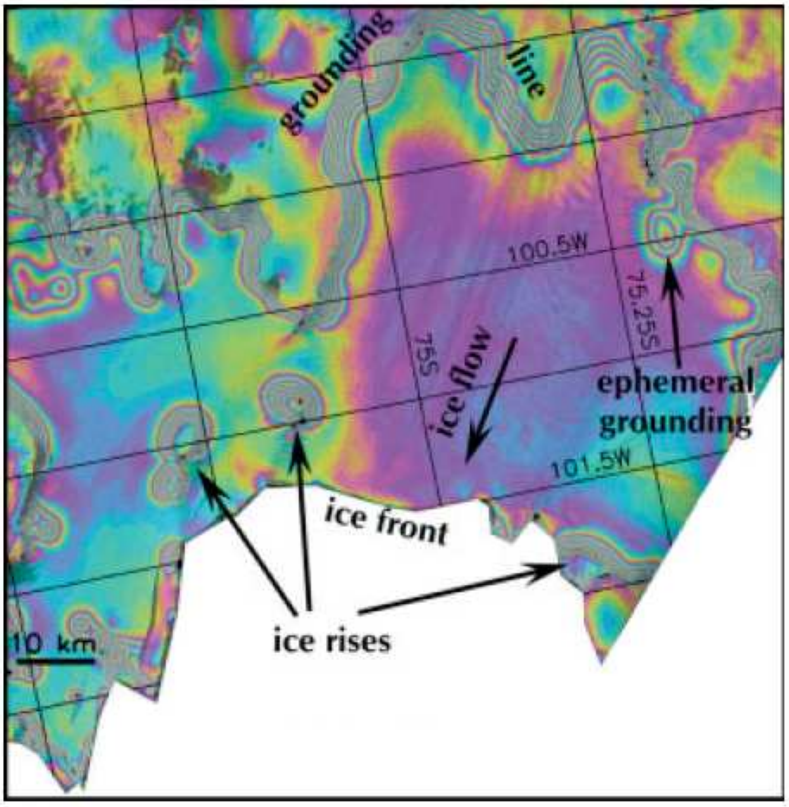

Figure 3.6: Differential interferogram of the Pine Island Ice Shelf in the Amundsen Sea Sector of West Antarctica, from Schmeltz *et al.* (2001). Each colour cycle (*fringe*) represents a 12 radians phase shift, equivalent to $\sim$ 6 cm vertical displacement of the surface. The ice shelf lies between the ice front and the densely-spaced fringes running along the top of the image, which are indicative of the transition from freely-floating to grounded ice.

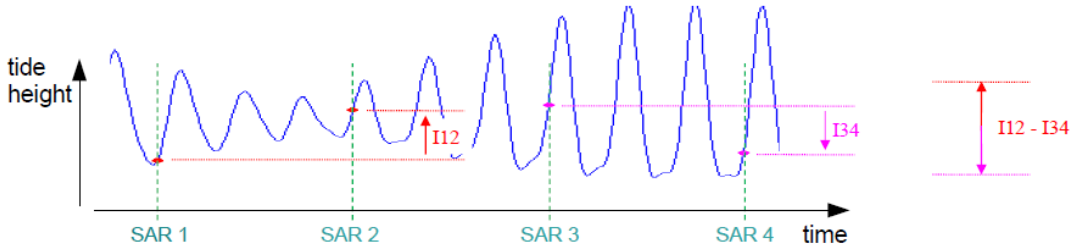

Figure 3.7: The tidal signal recorded in a differential interferogram. *SAR 1-4* denote the acquisition times of the four synthetic aperture radar images, *I12* and *I34* indicate the tidal displacement captured in each interferogram, and *I12 - I34* indicates the displacement signal recorded in a differential interferogram.

ice shelf motion, such as changes in ice shelf height resulting from fluctuations in atmospheric pressure (the so called *Inverse Barometer Effect* or *IBE*). Finally, there are only a few studies to date that have utilised InSAR observations to validate tide models and so tide model accuracy in remote regions of Antarctica, such as the Amundsen Sea, is still relatively uncertain. Because of the importance of tide model accuracy to a range of applications, there is a need to (1) develop further InSAR methods to quantify the error associated with model predictions of tidal displacement, and (2) conduct further, comprehensive assessments in remote regions to supplement the few studies to date.

3.3 Satellite-based Methods for Mapping Ice Shelf Flow

Mapping ice shelf flow provides a means to monitor (1) the stability of ice shelves and their inland catchments (Rignot *et al.*, 2004; Vieli *et al.*, 2007), (2) the processes through which ice shelves interact with their surrounding environment (Joughin and Padman, 2003), and (3) the coupling between floating and grounded ice (Payne *et al.*, 2004). Satellite-based observations are well suited for mapping ice shelf flow and for monitoring ongoing changes, as they provide regular and

spatially extensive coverage. Early studies used data from sensors operating at optical frequencies to develop techniques to map the flow of inland (grounded) (Bindschadler and Scambos, 1991) and floating (Lucchitta and Ferguson, 1986) ice. These studies demonstrated that ice flow speeds could be determined by tracking the movement of surface features in co-registered pairs of satellite images. However, usable data acquired over this waveband was limited because (1) the ice surface was often hidden by cloud cover, (2) data acquired at night was not usable, and (3) the ice surface was featureless over much of the ice sheet. In view of these limitations, synthetic aperture radar (SAR) provides a valuable alternative source of data. Operating at microwave frequencies allows the penetration of clouds, reveals trackable patterns over apparently featureless ice surfaces and allows meaningful surface displacement information to be derived from phase changes in the returned signal. Being an active system (i.e. emitting its own radiation), it is not reliant upon ambient solar radiation, and so can also operate at night. Several different SAR techniques have been utilised to map ice shelf flow from SAR imagery. These are described below.

3.3.1 Mapping Ice Shelf Flow with Synthetic Aperture Radar Feature Tracking

Using methods analogous to those employed to track features in optical imagery, estimates of ice flow have been determined from pairs of SAR images by measuring the displacement of features, such as crevasses, recorded in the amplitude of the returned signal (Werner *et al.*, 2001; Strozzi *et al.*, 2002; Luckman *et al.*, 2003; Luckman and Murray, 2005; Luckman *et al.*, 2006) (figure 3.8). When the pair of SAR images are *coherent* (i.e. there is a good degree of correlation between the signals recorded at each acquisition), two additional tracking methods can be used. These offer improved spatial and temporal precision, and can detect

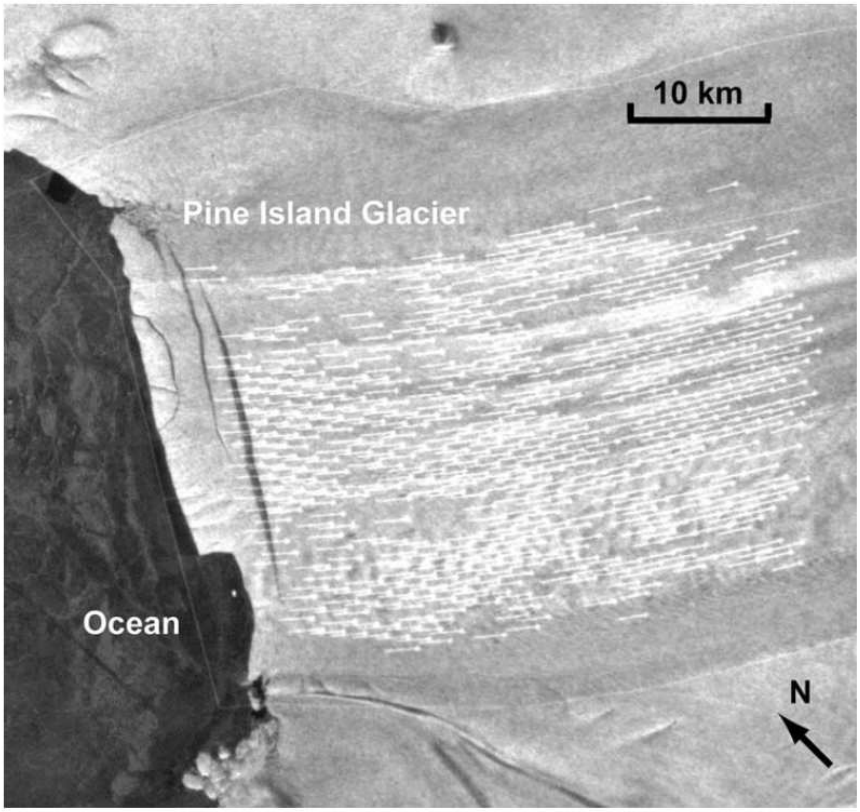

Figure 3.8: Surface velocity vectors (white arrows) of the Pine Island Ice Shelf, determined using the technique of SAR intensity tracking, from Lucchitta and Rosanova (1997).

displacement over apparently featureless terrain. Speckle tracking matches small-scale trackable patterns (referred to as *image speckle*) in either the backscatter amplitude, or the complex (amplitude and phase) images (Gray *et al.*, 1998; Michel and Rignot, 1999; Gray *et al.*, 2001; Joughin, 2002). Coherence tracking matches similar patterns based purely on the phase of the returned signal (via an optimisation of the phase coherence between patches of the SAR image pair) (Derauw, 1999; Werner *et al.*, 2001; Pattyn and Derauw, 2002). With both techniques, the patterns that are tracked relate to the configuration of individual scatterers within a resolution cell. These patterns only persist for as long as the scatterer configuration remains stable and so limit these coherence-based techniques to measuring displacement over typically daily to weekly timescales. Using these techniques, displacement can be measured with an order of magnitude improvement in accuracy, as compared to methods that track features in optical imagery (Gray *et al.*, 1998). These techniques for mapping ice flow from SAR data have been readily applied to map ice shelf flow speeds (Luckman and Murray, 2005; Rignot, 2008).

3.3.2 Mapping Ice Shelf Flow with Interferometric Synthetic Aperture Radar

Synthetic aperture radar data can also be used to map ice flow using the technique of radar interferometry (Goldstein *et al.*, 1993; Joughin *et al.*, 1995, 1996a; Kwok and Fahnestock, 1996; Rignot, 1996; Luckman *et al.*, 2002; Rignot *et al.*, 2008). This technique has the potential to provide a higher spatial resolution, precision and accuracy than the tracking methods described above (Werner *et al.*, 2001; Joughin, 2002; Massom and Lupin, 2006). As described in section 3.2.1, when a SAR images an ice shelf, the measured displacement consists of motion from ice flow, the action of the ocean tide and variations in atmospheric pressure. To

map ice flow, these other signals must be removed. Commonly, in the case of the tidal signal, this has been achieved by using a tide model to simulate the difference in tide height at the times of the SAR acquisitions (Rignot and Jacobs, 2002; Joughin *et al.*, 2003; Rignot *et al.*, 2004; Vieli *et al.*, 2006). An alternative technique was proposed by Rignot (1996), whereby ice shelf flow speeds at a limited number of locations were determined by tracking crevasses in a pair of SAR backscatter images. This allowed the tidal signal to be isolated at these locations. In both methods, the predicted tidal amplitude was combined with a map detailing the pattern of tidal displacement (determined using differential InSAR, see section 3.2.1), to estimate tidal displacement over the whole ice shelf. This signal was then removed from the original interferogram, producing a map of ice flow, with any IBE signal ignored. Both of these methods for isolating the flow component of the InSAR displacement signal have limitations. In the case of the method which uses model predictions, errors arise from the limited accuracy of model simulations of the tidal signal. In the case of the method that uses tracking displacement estimates (Rignot, 1996), there is a reliance upon tracking data, which has an inferior accuracy and precision to InSAR (Werner *et al.*, 2001). For example, in the study of Rignot (1996) tracking velocities were calculated over a one year period, and as such these velocity estimates may vary from the daily-scale displacement recorded in an interferogram. In both methods, because displacement is measured over a short time period, an anomalous period of flow may be captured (e.g. because of tidal modulation of flow) and this may lead to inaccuracies when scaling to an annual velocity.

3.3.3 Comparison of SAR Techniques for Mapping Ice Shelf Flow

The methods described above for mapping ice shelf flow each have advantages and disadvantages. Typically, when mapping ice flow, InSAR provides the greatest accuracy, precision and spatial resolution, followed by coherence-based tracking approaches (coherence tracking and speckle tracking), followed in turn by incoherent tracking approaches (incoherent intensity tracking) (Werner *et al.*, 2001; Joughin, 2002; Strozzi *et al.*, 2002; Massom and Lupin, 2006). All coherence-based techniques (InSAR and tracking) are ineffective when coherence is not maintained. This constraint limits the quantity of data available; both in the exclusion of regions which do not exhibit a coherent signal (e.g. because of high precipitation rates), and because only image pairs separated by a short time period can be used. Incoherent tracking approaches, on the other hand, do not suffer these constraints, but do instead require larger scale (i.e. spanning multiple pixels) surface features, such as crevasses, that can be tracked. Also, because incoherent techniques typically track features over a much longer time period, they suffer less contamination from short period effects, such as from tide- and atmospheric pressure-related motion of the ice shelf. Unlike tracking methods, InSAR only measures ice flow in a single dimension and so, without additional information, a second viewing direction is needed to determine ice flow velocity vectors. Often there is insufficient data to achieve this, and so a tracking solution must be used to provide a second component of the velocity field. In light of these considerations, the most suitable technique will vary depending upon the application, data availability and region of study, and often a combination of approaches (Joughin, 2002) will provide the most effective solution.

3.4 Summary

In this chapter I have provided a brief review of the techniques employed in this thesis. The following three chapters describe the work undertaken in this thesis. Each of these chapters takes the form of a journal article, and details of the publication status of each article precede each chapter. Chapter 4 details work to produce a new bathymetric map, Chapter 5 provides an assessment of tide models and Chapter 6 outlines a new method for mapping ice shelf flow. Each study focuses upon the Amundsen Sea, and demonstrates the utility of satellite-based radar data to studying ice-ocean interactions. In Chapter 7 I describe how the three results chapters address the aim of my thesis and provide new datasets and methods that will contribute to an improved understanding of ice-ocean interactions in the Amundsen Sea.

Chapter 4

Amundsen Sea Bathymetry: The Benefits of Using Gravity Data for Bathymetric Prediction

Malcolm McMillan[1], Andrew Shepherd[2], David G. Vaughan[3], Seymour Laxon[4] and David McAdoo[5]

A modified version of this chapter has been published in IEEE Transactions on Geoscience and Remote Sensing, Vol. 47, No. 12, p. 4223-4228, December 2009.

Acknowledgement of contribution: D. Vaughan provided the ship-based survey data, S. Laxon and D. McAdoo provided the gravity data. D. McAdoo drew figures 4.1 and 4.3.

[1]The University of Edinburgh, Drummond Street, Edinburgh, EH8 9XP, UK
[2]The University of Leeds, Leeds, LS2 9JT, UK
[3]The British Antarctic Survey, High Cross, Madingley Road, Cambridge, CB3 0ET, UK
[4]University College London, Gower Street, London, WC1E 6BT, UK
[5]National Oceanic and Atmospheric Administration, Silver Spring, Maryland 20910, USA

4.1 Abstract

Bathymetric charts are essential for modelling oceanic processes, yet in remote areas direct measurements of seafloor depth are often scarce. It is possible to augment sparse depth soundings with dense, satellite-derived gravity data, to provide additional bathymetric detail in regions devoid of sounding data. We demonstrate this method by using marine gravity derived from the European Remote Sensing (ERS-1) satellite altimeter, combined with depth soundings, to form a bathymetric prediction of the Amundsen Sea, West Antarctica. We estimate the root mean square error of depth estimates at un-surveyed locations in our solution to be $\sim$ 120 metres. We use a Monte Carlo method to assess the value of gravity as a bathymetric predictor in sparsely surveyed regions, by comparing our solution to predictions formed from depth soundings alone. When less than $\sim$ 11 % of 10-km grid cells contain depth soundings, inclusion of gravity data improves the depth-accuracy of the solution by up to 17 %, as compared to a minimum curvature surface interpolation of the depth soundings alone. When depth data are sparse, our gravity-derived prediction reveals additional short-wavelength bathymetric features, such as troughs on the continental shelf, which are not resolved by interpolations of the depth soundings alone.

4.2 Introduction

Approximately 70 % of Earth's surface lies below sea-level, yet in comparison to Earth's land-masses, the topography of the ocean floor, especially in the Southern Ocean, is not well known (Smith, 1993). Ship-based surveys of seafloor topography provide incomplete coverage due to the limited opportunities available for acquiring data, and there still exist areas as large as 10^5 km^2 with no sounding data (Marks and Smith, 2006). Because bathymetric predictions aid scientific

advancement across a diverse range of fields - oceanography, marine biology and geology, to name a few - it is important that, in sparsely surveyed regions, additional techniques are utilised to allow the incorporation of complementary data.

A number of studies (Dorman and Lewis, 1970; Lewis and Dorman, 1970; McKenzie and Bowin, 1976) have shown that, over a restricted range of length-scales, anomalies in the marine gravity field are well correlated with topographic variations. Dixon *et al.* (1983) compared known bathymetry with one-dimensional marine gravity anomalies derived from satellite altimetry and demonstrated that filters could be developed to predict topographic variation from these gravity data. After the declassification of Geosat data (acquired between March 1985 and September 1986), Smith and Sandwell (1994, 1997) combined satellite altimetry from the Geosat, Seasat and European Remote Sensing (ERS) 1 satellites, along with depth sounding data, to map ocean bed topography between 72°S and 72°N. Dense satellite altimetry was used to derive gravity anomalies, and this was converted to seabed topography with the aid of the sparse ship-based depth measurements, which were used for model calibration. This method achieved a far greater uniformity of coverage than was possible with depth sounding data alone and resolved additional bathymetric detail in the areas between sparse ship tracks. Although this published prediction was limited to regions north of 72°S, and so excluded almost all of West Antarctica's coastal waters, an updated version of this dataset is now available (http://topex.ucsd.edu/WWW_html/mar_topo.html), which incorporates ship tracks south of 72°S and an extended gravity field. However, the accuracy of this solution has yet to be determined, and the extent to which gravity data can improve polar bathymetric solutions derived solely from ship-based depth soundings (Nitsche *et al.*, 2007) remains unclear. In this paper, we augment ship-based depth soundings with dense satellite altimeter derived marine gravity data (McAdoo and Laxon, 1997) to produce a bathymetric map

of the Amundsen Sea, and assess the value of gravity as a bathymetric predictor in this region.

4.3 Data and Method

Our area of study comprises the region from 90°W to 120°W, and extends north from the Antarctic coast to 68°S. In this region ship-based depth soundings are more abundant than in other Antarctic waters, and so we were able to form bathymetric predictions using quantities of depth soundings typical of more sparsely surveyed regions, whilst retaining additional data for the purpose of model assessment. Additionally, the bathymetry in this region exhibits a variety of different length-scale features, and the area is of interest to current glaciological and oceanographic studies (see, for example, Thoma *et al.* (2008)). Ship-based depth measurements (figure 4.1a) were acquired from 15 single-beam and multi-beam survey missions (ELT11, ELT17, ELT33, ELT42, DSDP35GC, THB80, DF85, PD190L02, RITS94B, NBP92-08, NBP94-02, NBP95-05, NBP96-02, NBP99-02, NBP00-01). These data are well distributed over our study area, although we note that more recent acquisitions (see Nitsche *et al.* (2007), not available to us) offer greater coverage in some regions.

Several free air gravity anomaly maps for the area of interest exist (McAdoo and Laxon, 1997; Sandwell and Smith, 2005, 2009). We chose to use the map derived by McAdoo and Laxon (1997) (figure 4.1b), because the altimeter waveform re-tracking procedure used to form the solution was optimised for regions covered with sea ice. Consequently this solution has a reduced noise level over such regions (Peacock and Laxon, 2004), as compared to solutions formed using a re-tracker designed for open ocean (Sandwell and Smith, 2009). Variations in the marine gravity field manifest themselves as topographic features on the sea

surface, which can be measured by satellite based altimeters and used to derive marine gravity anomalies (McAdoo and Marks, 1992; Sandwell, 1992; Sandwell and Smith, 1997; Peacock and Laxon, 2004). The gravity anomaly map (figure 4.1b) utilises altimetry data from the ERS-1 satellite, which has a sufficiently high orbit inclination angle (98.5°) to give the coverage required to map the continental shelf region of the Amundsen Sea. Data were collected during the ERS-1 satellite Geodetic Mission (April 1994 - March 1995), and consist of densely spaced ($\sim$ 3 km at 72°S) ground tracks. These were supplemented with five additional cycles of ERS-1 35-day repeat data, which allowed data gaps occurring in any individual cycle of data to be filled, and random errors or noise in individual data profiles to be reduced via temporal averaging. The presence of sea ice on the Amundsen Sea surface increases the uncertainty associated with standard altimeter-derived sea-surface elevation measurements. To minimise this uncertainty, many months of ERS-1 data were averaged, ERS-1 returns from large icebergs were edited out and the full altimeter waveform data were used, which enabled the range difference between the leading edge of the waveform and the range given by the instrument's on-board tracker to be estimated (Laxon and McAdoo, 1994). The resulting offset was used to apply a correction and to reduce the noise associated with the presence of sea ice (Laxon, 1994; Peacock and Laxon, 2004). For the purpose of this study, we chose to grid both the depth sounding data and the gravity data at 10-km resolution.

Flexural isostatic compensation theory describes how the lithosphere acts under a topographic load and can be used to construct a function (termed *gravitational admittance*) that relates variations in seafloor height to gravity anomalies (Smith and Sandwell, 1994). By inverting this function it is possible to predict bathymetry from gravity anomalies. This prediction is limited to a restricted range of length scales (between $\sim$ 15 km and the flexural wavelength of the lithosphere), over which the relationship between gravity and topography is adequately

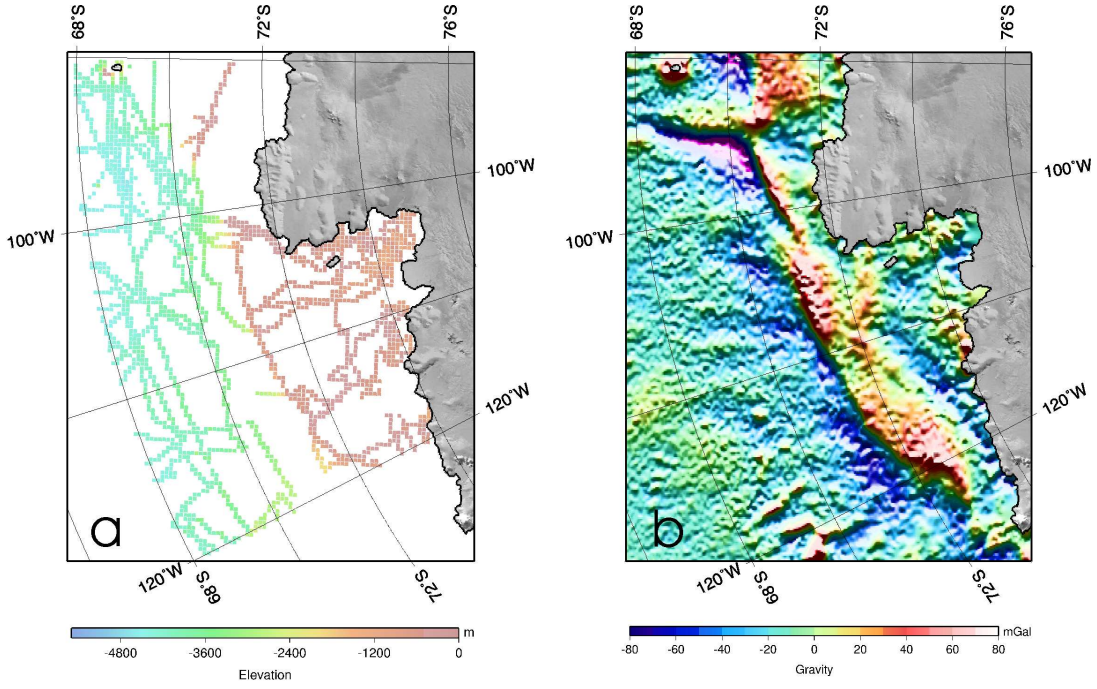

Figure 4.1: a. Gridded depth sounding tracks; b. Gravity anomalies derived from satellite altimetry (large anomalies omitted from colour scale).

characterised by a linear approximation (Smith and Sandwell, 1994). At wavelengths longer than the flexural wavelength of the lithosphere, which is typically between 135 and 800 km (Smith and Sandwell, 1994), lithospheric isostatic compensation almost completely cancels any topographic effect on the gravity field, and so variations in bathymetry do not correspond to variations in the gravity anomaly. At short (sub 15 km) wavelengths, the signal to noise ratio of the gravity field is small, and so variations in the measured gravity anomaly do not necessarily represent topographic variation (Smith and Sandwell, 1994). Consequently, outside of this restricted waveband, gravitational admittance tends towards zero and bathymetric prediction is unreliable. Following the method of Smith and Sandwell (1994), we construct high- and low-pass filters (equations 4.1 and 4.2, respectively, and figure 4.2) to remove long- and short-wavelength features that fall outside of this restricted waveband.

$$W_1(k) = 1 - \exp[-2(\pi k s)^2] \tag{4.1}$$

$$W_2(k, d) = [1 + 9500k^4 \exp(4\pi k d)]^{-1} \tag{4.2}$$

Equation 4.1 defines a Gaussian high-pass filter as a function of wavenumber, k, which is used to suppress wavelengths longer than the flexural wavelength of the lithosphere. s is a parameter that controls the shape of the filter. Because the precise flexural wavelength of the lithosphere in this region is not well constrained within the 135-800 km range, we choose a value of 60 km for the parameter s (as compared to a value of $s = 30$ km in Smith and Sandwell (1994)), and consequently W_1 has half amplitude when $\mathrm{k}^{-1} = 320$ km. This choice of s maximised the improvement gained by the inclusion of the filtered gravity data. Equation 4.2 is a function of wavenumber, k, and the regional water depth (in km), d. For a regional depth of 2.5 km (the mean of our depth sounding dataset) W_2 has a half amplitude when $\mathrm{k}^{-1} = 16$ km. The combined band pass filter, $W_1 W_2$, is shown in figure 4.2.

We calculate the relationship, S, between the filtered gravity and topography on a coarse (135 km) grid, using a method similar to that of Smith and Sandwell (1994). At every point we form a linear regression between all depth sounding data within a 135 km radius and the corresponding gravity data. We use this regression to estimate the relationship between gravity and topography at that location. Where there is insufficient depth sounding data nearby, or there is a poor correlation between depth soundings and gravity anomalies, a global solution based upon all depth soundings in the study area is used. The magnitude of the correlation between all depth soundings and the corresponding gravity anomalies is 0.58. The resulting grid is re-sampled to the resolution of the gravity data

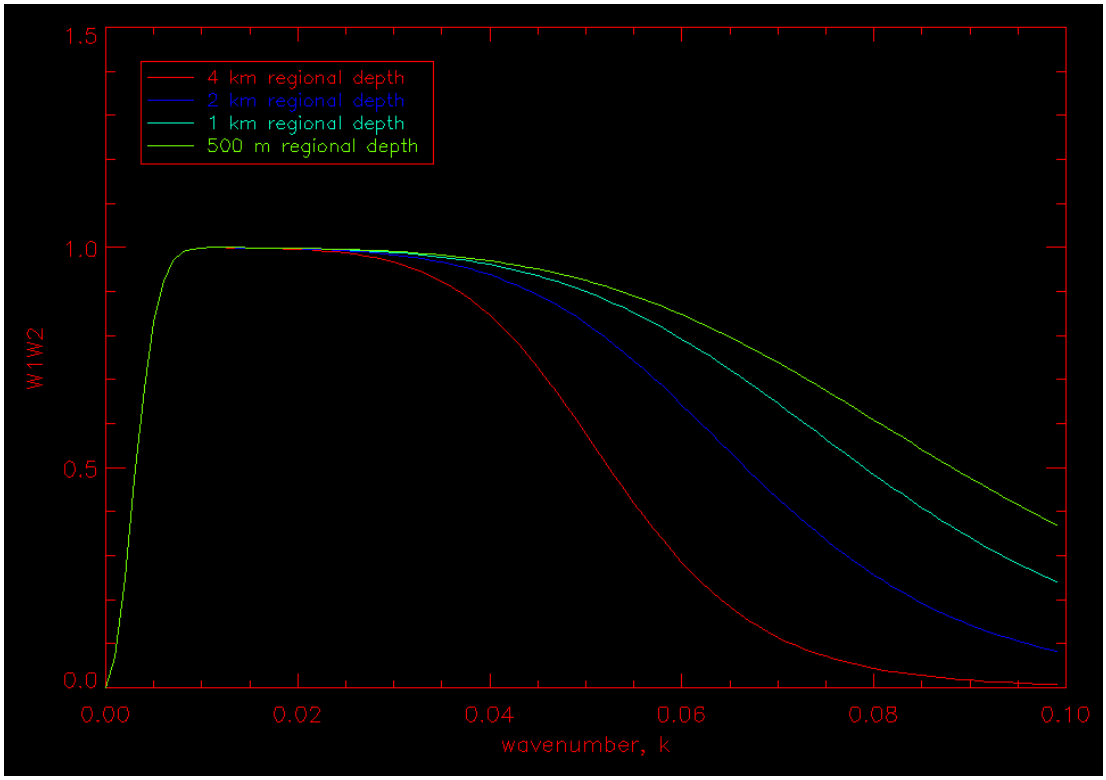

Figure 4.2: The band-pass filter W_1W_2 (equations 4.1 and 4.2) plotted as a function of wavenumber, k (km^{-1}), for a range of regional sea floor depths.

and then multiplied by the gravity data to estimate seafloor topography over the same waveband. By allowing S to vary, it is possible to account for regional differences in ocean floor density, caused by variations in ocean bed material and, in particular, the depth of sediments on the seabed. Long (greater than 320 km) wavelength topography is added to our prediction by low-pass filtering an interpolation based upon our depth sounding dataset. Finally, we force our prediction to fit the depth sounding data.

4.4 Results and Model Assessment

We use the method described above to generate a bathymetric map of the Amundsen Sea, West Antarctica (figure 4.3). This map utilises data with a uniformity of coverage not offered by the depth sounding data alone. Our prediction resolves a varying continental shelf break gradient and mounds extending seawards of the shelf break. On the continental shelf, deep (exceeding 600 metres) troughs extend from beneath the Pine Island, Thwaites, Crosson, Dotson and Getz ice shelves, all of which have undergone thinning in recent years (Shepherd *et al.*, 2004).

To assess the performance of our model, and the benefits of using gravity data to reduce bathymetric uncertainty in sparsely-surveyed polar waters, we used several different interpolation schemes to form solutions based solely on the depth sounding data. We constructed a triangulation network and used a bilinear interpolation scheme to form a bathymetric solution. We also used a natural neighbour interpolation scheme and a minimum curvature surface (MCS) interpolation scheme to form alternative solutions. These interpolations were implemented using standard interactive data language (IDL) routines. We ran a Monte Carlo simulation to compare our gravity-derived prediction with these interpolations. In each case, we ran all models with the same, randomly selected,

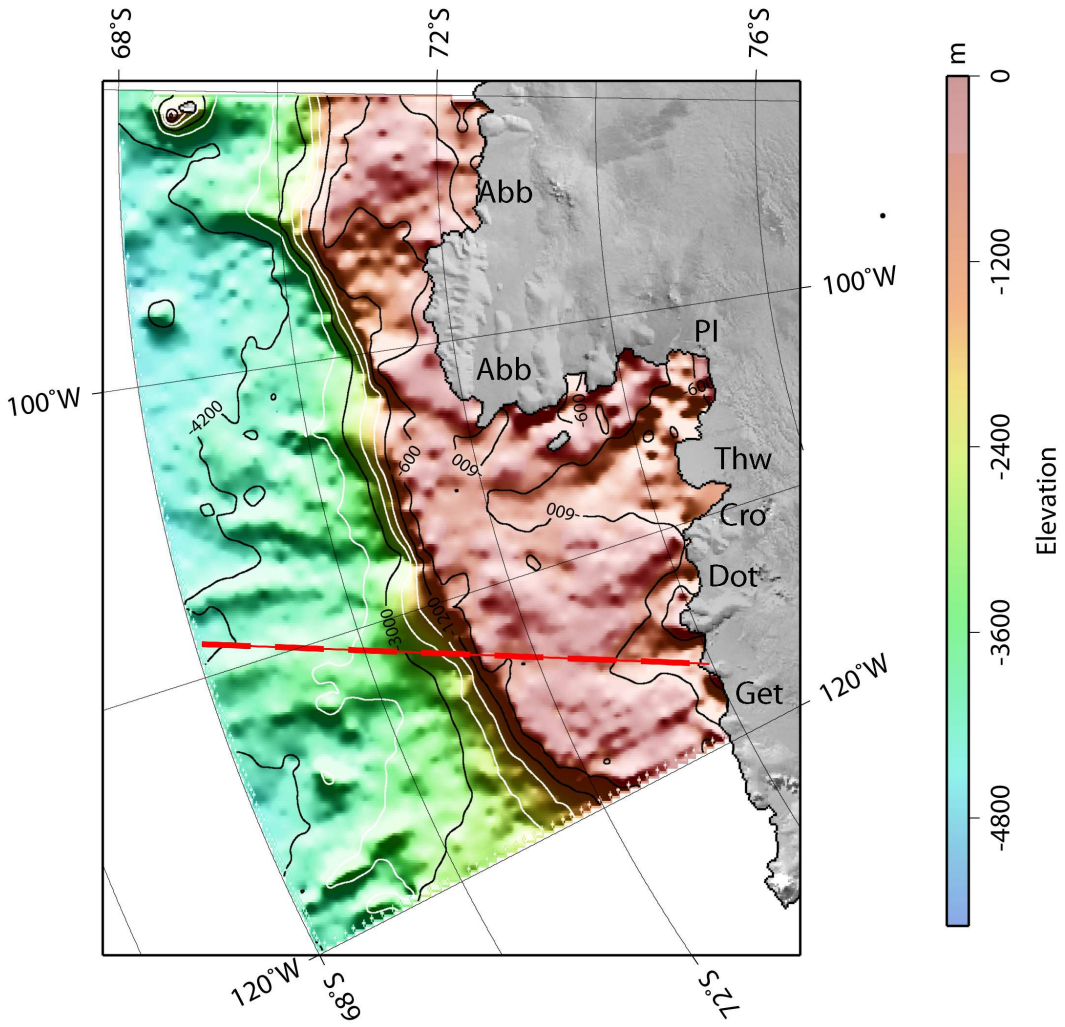

Figure 4.3: Bathymetric prediction from gravity anomalies and ship-based depth soundings, Amundsen Sea, West Antarctica. Dashed red line indicates the location of the transect shown in figure 4.5; Abb, Abbot Ice Shelf; PI, Pine Island Ice Shelf; Thw, Thwaites Ice Shelf; Cro, Crosson Ice Shelf; Dot, Dotson Ice Shelf; Get, Getz Ice Shelf.

subset of the gridded depth sounding data. We then compared a randomly selected fraction of the remaining gridded depth soundings (equating to ~ 400 grid cells) with each model's estimate of depth at those locations. We repeated this process, running the models with ten different random selections of sounding data and defined the model error to be the root mean square deviation (RMSD) of all (~ 4000) model estimates from the coincident observed depth values. We adopted the RMSD of the predicted depth from the withheld data as a measure of model accuracy because this function penalises increases in both the magnitude and the range of a model's deviation from the actual depth (both factors are important in assessing the performance of a model). We repeated this comparison, using varying fractions of the depth sounding dataset as model input, to investigate how the density of depth soundings affected model performance. During this process, the proportion of 10-km ocean grid cells containing at least one ship-based depth sounding observation (hereafter referred to as the density of sounding data) ranged from 0.5 % to 11.1 %. The fraction of sounding data used to validate each model was kept constant throughout.

Our assessment (figure 4.4) indicated that the accuracy of solutions based solely on depth soundings was highly sensitive to the choice of interpolation scheme. For example, the solution based on a MCS interpolation scheme returned, on average, a 36 % improvement in accuracy as compared to a bilinear interpolation of the depth soundings. The accuracy of the natural neighbour interpolation scheme varied greatly as a result of occasional instances where there was a very large deviation of the solution from the measured depth. Of the bathymetric predictions based on depth soundings alone, we found that the solution formed using a MCS interpolation scheme gave the most accurate results, regardless of the density of depth soundings used for the interpolation. Next, we compared the MCS solution with our gravity-derived prediction (figure 4.4). For all densities of depth sounding data analysed in this assessment (0.5 % - 11.1 %), the inclusion of gravity data

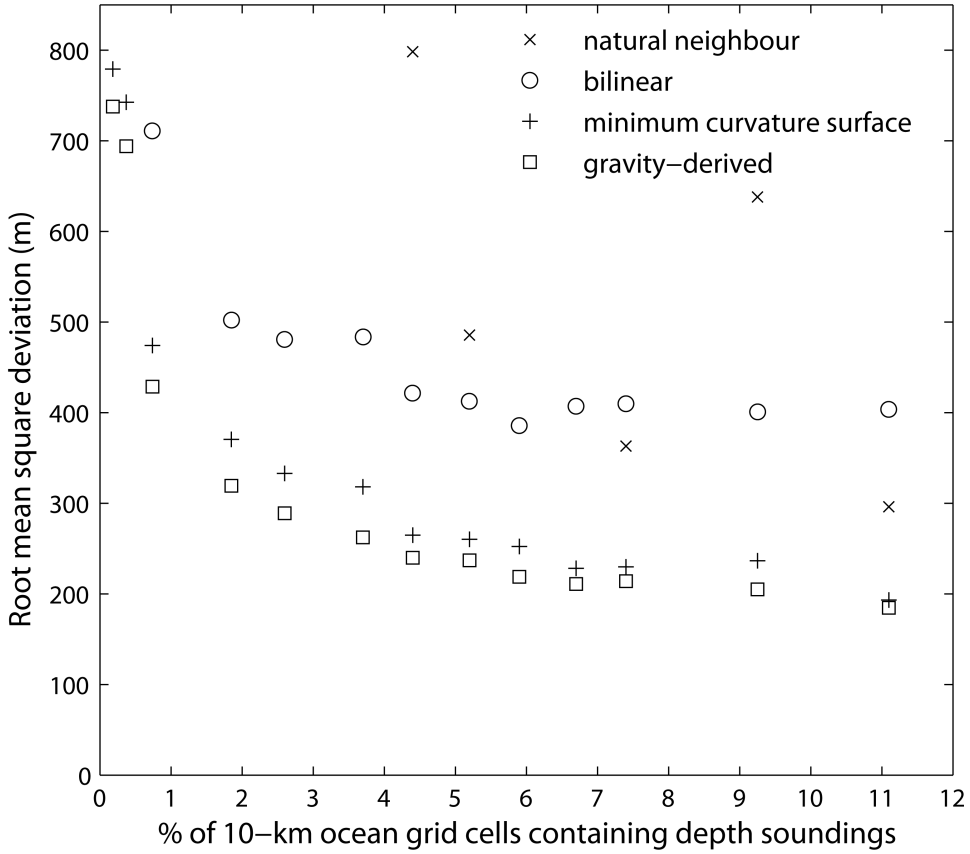

Figure 4.4: Comparison of the accuracy of the gravity-derived Amundsen Sea bathymetry, with the accuracies of bathymetries formed using different interpolations of the depth sounding data alone. The root mean square deviation of the model from withheld depth soundings is used to assess model accuracy. Each data point is calculated from $\sim$ 4000 grid cells, collected over ten model runs, where model estimates of depth are compared to withheld depth soundings. Root mean square deviations greater than 800 metres are not shown.

improved the accuracy of the solution. The mean and maximum improvement offered by our gravity-derived solution over the MCS interpolation was 10 % and 17 %, respectively. For densities of depth sounding data close to zero, the accuracy of the gravity-derived model was relatively low, reflecting a lack of data with which to calibrate the model. As the density of data increased, the accuracy of the gravity-derived solution rapidly improved, suggesting that a reasonable degree of certainty can be achieved with sparse depth sounding data. In other regions around Antarctica, ship-based depth data are considerably less abundant than in the Amundsen Sea, and so it is encouraging that our model reduces the level of uncertainty at low data densities. Furthermore, as the depth sounding density increased, the accuracy of the gravity-derived prediction improved at a higher rate than the MCS solution, with the inclusion of gravity data offering the greatest benefit (relative to the MCS solution) when the density of depth soundings was $\sim$ 3 %. As the density of depth soundings increased further, our gravity-derived solution continued to outperform the MCS solution, but the margin of improvement tended to decrease - a consequence of the diminishing impact of gravity data once a large number of depth soundings are available to guide the model. Consequently, our study indicates that when the density of gridded depth sounding data is less than $\sim$ 11 %, (1) the choice of interpolation scheme can greatly affect the RMSD-accuracy; and (2) incorporating gravity data into a bathymetric prediction will give further benefits. We note that, when this technique is applied elsewhere, both the range of data densities over which gravity adds value, and the magnitude of the improvement achieved, may vary as a result of the quality of the gravity data and the topography of the area being mapped. To obtain an estimate of the accuracy of our final bathymetric prediction, we modelled the relationship between the density of depth soundings and the RMSD of our gravity-derived model. This relationship was well approximated ($R^2 = 0.98$) by a power law and indicated that our bathymetric prediction, when formed using

our entire depth sounding dataset, could be expected to have a RMSD of $\sim$ 120 metres.

Several authors (Rignot and Jacobs, 2002; Payne *et al.*, 2004; Shepherd *et al.*, 2004; Walker *et al.*, 2007) have concluded that recent glaciological changes in the Amundsen Sea sector of the WAIS (Shepherd *et al.*, 2002; Davis and Ferguson, 2004; Rignot, 1998) have been caused by high rates of ocean-driven ice shelf melting, resulting from the flow of relatively warm Circumpolar Deep Water (CDW) to the coast (Jacobs *et al.*, 1996). The routing of CDW is dependent upon troughs on the continental shelf sea floor and so models of CDW flow require accurate maps of the structure and extent of these troughs. The length-scales of these troughs are such that they typically fall within the waveband over which gravity adds bathymetric detail. Consequently, gravity-derived bathymetric solutions are well suited for mapping these features, in particular in regions around Antarctica where depth soundings are sparse. Figure 4.5 illustrates such a scenario from our study area, whereby the addition of gravity data resolves a trough (of width $\sim$ 100 km) on the continental shelf. Both the gravity-derived solution and the MCS interpolation transects shown in figure 4.5 were obtained using the same subset of depth soundings, which occupied $\sim$ 1 % of grid cells in our study area. In each case, the transect was obtained from the full 2-dimensional solution, and was thus constrained both by data along the transect and by nearby data on either side of the transect. Further depth soundings located along the transect, which were not used to constrain either model, were used to assess model performance. Although both models provide an accurate map of the large, long-wavelength depth variation of the continental shelf break (figure 4.5a), the gravity-derived solution provides greater mid- and short-wavelength topographic detail (figure 4.5b, long-wavelength topography removed). In particular, the gravity-derived solution resolves the $\sim$ 500 metre deep, 100 km wide trough on the continental

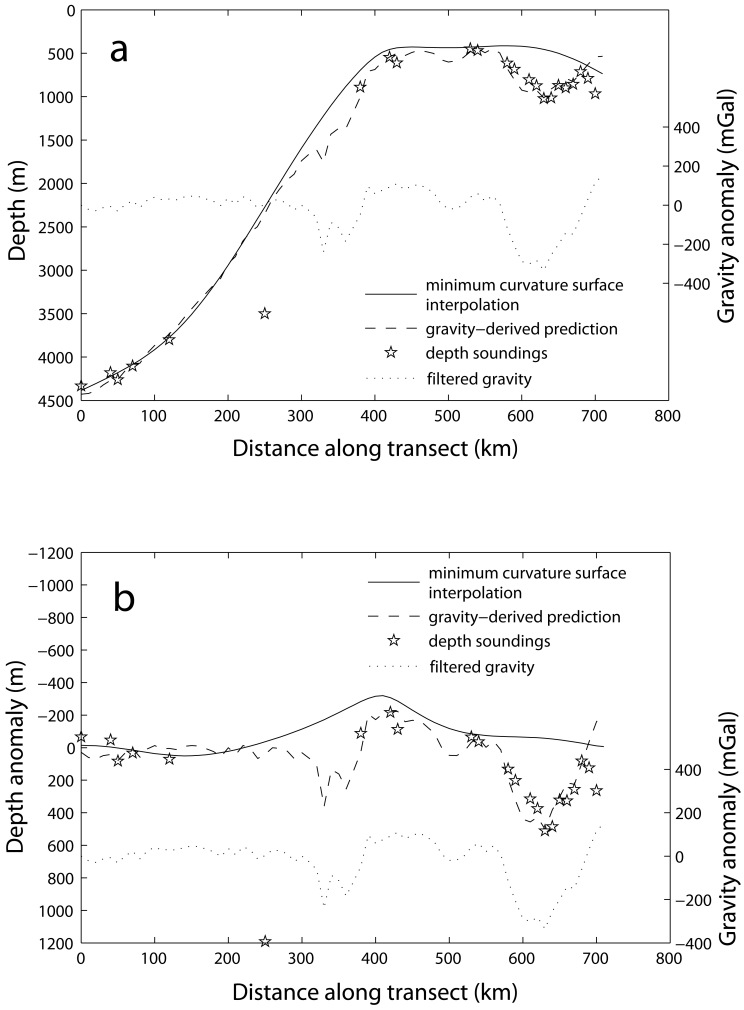

Figure 4.5: Comparison of gravity-derived Amundsen Sea bathymetry, with a bathymetry determined by a minimum curvature surface interpolation of depth soundings alone, along a transect (location shown in figure 4.3). Also shown are ship-based depth soundings that were excluded from both predictions and used to validate both models, and the gravity anomaly along the transect. a. sea-floor depth. b. local topographic variation, formed by removing long-wavelength topography.

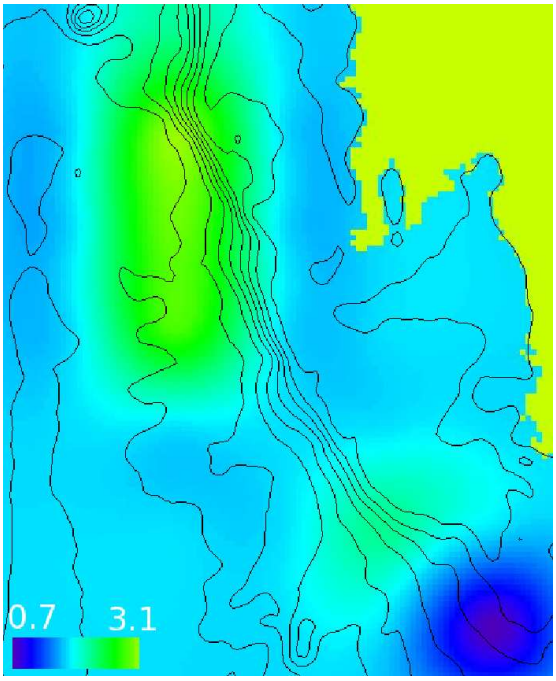

Figure 4.6: The ratio, S, of band-passed topography over gravity. For reference, bathymetric contours are shown (black lines, from figure 4.3). The ice sheet has been masked in yellow.

shelf floor (600-700 km along the transect), which the MCS interpolation fails to predict.

The presence of sediment can diminish the effectiveness of gravity as a bathymetric predictor, as the assumption is made that topographic variations correlate with variations in ocean floor mass. For example, if sediments (of a typically lower density than the underlying bedrock) preferentially fill topographic hollows (e.g. troughs on the continental shelf) then the bed topography will become flatter, whilst the gravity anomaly will reflect the steeper topography of the underlying bedrock. In such cases, the correlation between topography and gravity will be low and consequently we reject our local value of S in favour of the S value estimated from all data. S is plotted in figure 4.6. We find that low correlations in the locally-calculated S occur close to the coast in Pine Island Bay and in the deep ocean seaward of the continental shelf break. Close to the Pine Island Bay

shoreline, this may be because glacial sediments mask complex underlying bedrock topography. In the deep ocean, the lack of correlation may be accentuated by the decreased topographic relief, which will result in a relative increase in the influence of noise in the gravity field. At locations where there is a high local correlation between gravity and topography, S will vary as a function of the sea floor density. Specifically, increases in S are likely to be indicative of areas where the sea floor is less dense. There is a region of higher S just seaward of the continental shelf break, which I speculate may reflect the off-shelf sediment mounds that have been mapped in this region (Dowdeswell *et al.*, 2006). However, if this is the case, it is unclear why S is not elevated along the entire shelf break, and what causes the depressed value of S in the Western sector.

4.5 Conclusions

We have developed and evaluated a bathymetric prediction of the Amundsen Sea, West Antarctica, which incorporates ship-based depth soundings and satellite-derived gravity data. We estimate the root mean square depth deviation of our solution from the actual depth at un-surveyed locations to be $\sim$ 120 metres. Our prediction resolves a varying continental shelf break gradient, mounds extending seaward of the continental shelf break and troughs in the continental shelf that exceed 600 meters depth for much of their length. We perform a Monte Carlo simulation to assess the improvement in depth-accuracy offered by incorporating gravity data into our solution. We find that (1) in sparsely surveyed regions (where less than 11 % of 10-km grid cells contain depth soundings), incorporating gravity data into the bathymetric prediction improves model accuracy; (2) in sparsely surveyed regions, the accuracy of bathymetric predictions is highly dependent upon the choice of interpolation scheme; (3) the inclusion of gravity data offers the greatest benefit when $\sim$ 3 % of 10-km grid cells contain depth-soundings; and

(4) although an interpolation based solely on sparse depth soundings accurately resolves large-scale features, it omits shorter wavelength features that are not covered by depth sounding data, and that can be resolved with the inclusion of gravity data. Our study demonstrates that gravity data can retrieve bathymetric detail beneath polar seas, and so can improve bathymetric mapping in such regions where depth soundings are scarce, such as sparsely surveyed Antarctic coastal waters.

Chapter 5

Tide Model Accuracy in the Amundsen Sea, Antarctica, from Radar Interferometry Observations of Ice Shelf Motion

Malcolm McMillan[1], Andrew Shepherd[2], Peter Nienow[1], Amber Leeson[2]

A modified version of this chapter has been published in Journal of Geophysical Research, Vol. 116, C11008, November 2011.

Acknowledgement of contribution: A. Leeson provided the atmospheric pressure data.

[1]The University of Edinburgh, Drummond Street, Edinburgh, EH8 9XP, UK
[2]The University of Leeds, Leeds, LS2 9JT, UK

5.1 Abstract

This study assesses the accuracy of tide model predictions in the Amundsen Sea Sector of West Antarctica. Tide model accuracy in this region is poorly constrained, yet tide models contribute to simulations of ocean heat transfer, and to the removal of tidal signals from satellite observations of ice shelves. I use two satellite-based interferometric synthetic aperture radar (InSAR) methods to measure the tidal motion of the Dotson Ice Shelf at multiple epochs; a *single-difference technique* that measures tidal displacement, and a *double-difference technique* that measures changes in tidal displacement. I use these observations to evaluate predictions from three tide models (TPXO7.1, CATS2008a_opt and FES2004). All three models perform comparably well, exhibiting root mean square deviations from the observations of ~ 9 cm (single-difference technique) and ~ 10 cm (double-difference technique). Care should be taken in generalising these error statistics because (1) the Dotson Ice Shelf experiences relatively small semidiurnal tides, and (2) my observations are not sensitive to all tidal constituents. An error analysis of my InSAR-based methods indicates measurement errors of 7 cm and and 4 cm for the single- and double-difference techniques, respectively. A model-based correction for the effect of fluctuations in atmospheric pressure yields a ~ 6 % improvement in the agreement between tide model predictions and observations. This study suggests that tide model accuracy in the Amundsen Sea is comparable to other Antarctic regions where tide models are better constrained. These methods can be used to evaluate tide models in other remote Antarctic waters.

5.2 Introduction

Floating ice shelves fringe around one third of Antarctica's coastline (Sugden, 2009) and regulate the rate at which ice mass is lost from the continent. As a

consequence of being in contact with both the ocean and the warmer air around the ice sheet's margin, they are particularly sensitive to changes in atmospheric (Vaughan and Doake, 1996) and oceanic (Rignot and Jacobs, 2002; Shepherd *et al.*, 2004) conditions. Many studies have documented late-twentieth century ice shelf retreat (Vaughan and Doake, 1996; Rignot, 1998; Cook and Vaughan, 2010) and collapse (Rott *et al.*, 1996; Scambos *et al.*, 2009), and have identified the ocean and atmosphere as having driven these changes. Although the steric effect of ice shelf mass loss upon sea level is small (Shepherd *et al.*, 2010), an indirect dynamical response (De Angelis and Skvarca, 2003; Rignot *et al.*, 2004, 2005) resulting from reduced buttressing of upstream ice may provide a much larger sea level contribution (Payne *et al.*, 2004; Pfeffer *et al.*, 2008). Until this mechanism is incorporated into model predictions of the response of the Antarctic Ice Sheet (AIS) to changing climatic conditions, the future sea level contribution of the AIS remains uncertain. In this context, continued monitoring of ice shelf behaviour is essential.

Tide models contribute to our understanding of the response of the AIS to changes in its surrounding ocean environment. Tides are one of the principle drivers of ocean mixing beneath ice shelves and therefore tide models are an essential component of modelling studies of ice-ocean interactions (Makinson *et al.*, 2011). Tide models are also used to correct for the tidal signal in many satellite-based interferometric synthetic aperture radar (InSAR) methods to estimate ice shelf flow (Rignot and Jacobs, 2002; Joughin *et al.*, 2003; Rignot *et al.*, 2004; Vieli *et al.*, 2006). Such methods are used to assess ice shelf stability and the processes through which ice shelves interact with the atmosphere, the ocean and grounded ice upstream (Joughin and Padman, 2003; Vieli *et al.*, 2007). In a similar fashion, tide models have been used to remove unwanted tidal signals from altimetry-derived estimates of ice shelf surface height (Bamber *et al.*, 2009) and from time

series of satellite-based gravity measurements (Ray *et al.*, 2003). The accuracy of tide models impacts directly upon the accuracy of such observations.

The waters around Antarctica present a challenge for tide models because (1) satellite altimeter observations commonly assimilated into models (Egbert *et al.*, 1994) do not extend to Antarctic coastal waters, (2) in situ tidal records are sparse (King and Padman, 2005), (3) ocean bathymetry is relatively uncertain, and (4) water column thickness beneath ice shelves is generally not well known. Consequently, tide models perform less well around Antarctica than at more northerly latitudes (King and Padman, 2005; King *et al.*, 2011). Where in situ records exist, these can be used to evaluate tide models. However, large portions of the Antarctic coastline lack such records, and in these regions tide model accuracy is less certain. Satellite observations have been used to assess the accuracy of Antarctic tide models, including the techniques of laser altimetry (Padman and Fricker, 2005), radar altimetry (Fricker, 2002; Shepherd and Peacock, 2003) and InSAR (Rignot *et al.*, 2000; Rignot, 2002a; Padman *et al.*, 2003a). The utility of InSAR as a technique for measuring tidal motion was first demonstrated by Hartl *et al.* (1994) in a study of the Filchner-Ronne Ice Shelf. Later studies further developed this InSAR-based approach to (1) evaluate tide models at the Pine Island (Rignot, 2002a) and Ross (Padman *et al.*, 2003a) ice shelves, (2) demonstrate that InSAR could resolve small-scale tidal detail which was useful for model development (Rignot *et al.*, 2000), and (3) describe a theoretical analysis of how individual tidal constituents could be determined from InSAR data (Rignot *et al.*, 2000).

At present, tide model accuracy in the Amundsen Sea Sector of West Antarctica remains relatively uncertain. Only one study (Rignot, 2002a) has performed an assessment of a tide model in this region, which forms part of a 75° arc of coastline lacking (as of 2005) any in situ tidal records (King and Padman, 2005). InSAR-based studies hold the potential to evaluate tide models in this region. However,

a comprehensive assessment of the errors affecting InSAR observations of ice shelf tidal motion has yet to be conducted. Here I investigate the utility of two interferometric methods for evaluating ocean tide models. I firstly quantify the measurement error associated with each interferometric method and then assess the accuracy with which three tide models are able to predict tidal motion of the Dotson Ice Shelf in the Amundsen Sea.

5.3 Theoretical Background

The application of interferometric synthetic aperture radar to mapping ice motion has been well documented (Goldstein *et al.*, 1993; Joughin *et al.*, 1995, 1996a; Kwok and Fahnestock, 1996; Rignot, 1996). Here, I provide only a short overview of the methods relevant to this study. InSAR provides a measurement of ground displacement that is of superior precision and spatial resolution to other remote sensing methods, such as synthetic aperture radar (SAR) intensity tracking (Werner *et al.*, 2001; Massom and Lupin, 2006). It is however limited by its dependency upon surface coherence (i.e. the maintenance of a stable configuration of scatterers within each resolution cell). As such, it performs best over short time periods, typically measuring surface displacement over a period of several days. InSAR utilises SAR image-pairs to measure relative changes in the phase of the signal returned from a scattering surface. For any given pixel in a co-registered SAR image-pair, the unwrapped interferometric phase difference, φ, is related to the difference in the pixel-to-satellite range, Δr, by:

$$\varphi = \frac{4\pi}{\lambda}\Delta r \tag{5.1}$$

where λ is the radar wavelength ($\sim$ 5.7 cm for the European Remote Sensing

(ERS) satellites used in this study). For repeat-pass SAR acquisitions, the interferometric phase signal, φ, consists of a linear combination of terms:

$$\varphi = \varphi_{flat} + \varphi_{topo} + \varphi_{displ} \tag{5.2}$$

which refer to phase variations due to (1) increases in viewing angle across the ground track, φ_{flat}, (as described by the shape of Earth's ellipsoid), (2) surface topography, φ_{topo}, and (3) surface displacement in the radar's line of sight (range) direction, φ_{displ}, which occurs between the two SAR acquisitions. For the remainder of this section I shall assume that the first two terms have been simulated from a digital elevation model (DEM) and knowledge of the satellites' spatial configuration, and removed from the interferometric phase in order to isolate the displacement term (e.g. Joughin *et al.* (1998)). Errors associated with the incomplete removal of these effects will be assessed in section 5.7.

When InSAR images a floating ice shelf, the surface displacement term, φ_{displ}, is commonly separated into steady and non-steady components. Typically (Goldstein *et al.*, 1993; Rignot, 1996; Rignot and MacAyeal, 1998; Rignot *et al.*, 2000), the flow component of the displacement field, due to ice moving downstream, is categorised as a steady motion, approximately in the locally-horizontal plane. In contrast, the tidal component of motion, resulting from the oscillation of the floating ice shelf in response to the action of the ocean tide, is taken to be a vertical non-steady motion. Additionally, over the timescales of the InSAR data used in this study, atmospheric pressure changes can cause variations in sea surface height of the order of 10 cm (Rignot *et al.*, 2000; Padman *et al.*, 2003b). This atmospheric forcing introduces a further source of vertical non-steady ice shelf motion. Because of the viewing angle of the satellites used in this study ($\sim 23^\circ$ from vertical) the interferometer is at least 2.4 times more sensitive to vertical motion than to motion in the horizontal plane. The basis for

this work is that the displacement component of the phase signal (φ_{displ}) may be characterised as a simple combination of these separate flow (φ_{flow}), tidal (φ_{tide}) and atmospheric pressure (φ_{press}) signals:

$$\varphi_{displ} = \varphi_{flow} + \varphi_{tide} + \varphi_{press} \tag{5.3}$$

Here I describe two techniques that exploit differences in the temporal variability of these modes of displacement to separate the steady (flow) and non-steady (tide plus atmospheric pressure) components of ice shelf motion. These techniques provide the basis for two methods of evaluating tide models; one which determines tidal displacement (i.e. the tide-induced change in ice shelf elevation) and the other which measures the difference between two displacements.

5.3.1 Single-Difference Approach

My first method follows a similar approach to that described by Rignot (1996). I aim to directly estimate the non-steady, vertical displacement of the ice shelf, Δz, captured within a single interferogram. This method measures the difference in the ice shelf height between the times of the two SAR acquisitions and so I refer to it as a *single-difference* technique.

First I estimate the flow component of the line of sight displacement recorded by an interferogram, Δr_{flow}. This flow signal is extracted from a 2-d map of ice flow, which is determined by tracking the displacement of surface features in pairs of SAR backscatter intensity images. Because this tracking method measures displacement over a relatively long time period (see table 5.1 for details) it is insensitive to short-period signals and provides a close approximation of the steady flow signal. I then scale this tracking-derived displacement so that it

matches the time-scale of the interferogram. To isolate the non-steady signal within an interferogram, I convert the interferometric phase into a line of sight displacement (equation 5.1), remove the tracking-derived flow component, and convert the remaining non-steady signal into a vertical displacement:

$$\Delta z_{tide} + \Delta z_{press} = \frac{\Delta r - \Delta r_{flow}}{\cos \psi} \tag{5.4}$$

Here ψ is the incidence angle of the radar beam relative to the normal to Earth's ellipsoid, and Δz_{tide}, Δz_{press} denote the vertical change in ice shelf height occurring during the acquisition of the interferogram, due to the tide and atmospheric pressure fluctuations. To isolate the tidal component of this non-steady vertical motion, I use an inverse barometer approximation to correct for the effect of change in atmospheric pressure (Padman *et al.*, 2003b). This single-difference method assumes that the average velocity recorded within an interferogram matches that of the velocity observed using my tracking technique (see table 5.1 for a description of the acquisition periods of these techniques). Otherwise the tracking result will not exactly cancel the flow component of the interferometric signal. The single-difference technique is further limited by its reliance upon the SAR intensity tracking technique, which has an inferior precision and resolution to InSAR (Werner *et al.*, 2000).

5.3.2 Double-Difference Approach

My second method follows earlier work (Hartl *et al.*, 1994; Rignot, 1996, 2002a), whereby two interferograms are differenced in order to cancel the displacement component of the interferometric phase common to both interferograms. If flow velocities remain constant during the acquisition period, then the remaining

phase signal describes the difference in the vertical motion recorded in the two interferograms:

$$\Delta z_{1,tide} - \Delta z_{2,tide} + \Delta z_{1,press} - \Delta z_{2,press} = \frac{\lambda}{4\pi \cos\psi} (\varphi_{1,displ} - \varphi_{2,displ}) \quad (5.5)$$

where the subscripts 1 and 2 refer to the first and second interferograms. As with the single difference technique, an inverse barometer correction is applied to isolate the tidal signal. The resulting tidal signal is the difference between the two height differences captured in the pair of interferograms, and I therefore refer to this method as a *double-difference technique*. This method assumes that identical displacement occurs during each of the interferogram acquisitions. It also, by its nature, requires greater quantities of coherent SAR data.

5.4 Study Area

In this study I focus upon the Dotson Ice Shelf, in the Amundsen Sea Sector of the West Antarctic Ice Sheet (WAIS) (figure 5.1). Holding enough ice to raise sea levels by $\sim$ 1.5 m, the Amundsen Sea sector of the WAIS has the greatest mass deficit of all of Antarctica (Rignot *et al.*, 2008). Over the last two decades, satellite observations of this region have revealed a pattern of thinning of both grounded (Shepherd *et al.*, 2002; Pritchard *et al.*, 2009; Wingham *et al.*, 2009) and floating (Shepherd *et al.*, 2004; Wingham *et al.*, 2009) ice, glacier acceleration (Rignot, 2008) and grounding line retreat (Rignot, 1998). The penetration of warm circumpolar deep water via seabed troughs (chapter 4) to sub-ice shelf cavities (Thoma *et al.*, 2008; Jenkins *et al.*, 2010) suggests that high rates of ice

shelf basal melting (Rignot and Jacobs, 2002; Shepherd *et al.*, 2004) are primarily responsible for the changes witnessed in this region (Payne *et al.*, 2007).

The Dotson Ice Shelf (figure 5.1) occupies an area of ~ 3400 km^2, and is ~ 450 m thick (Shepherd *et al.*, 2004). It is fed by the Smith and Kohler Glaciers, which over recent decades have suffered sustained net mass loss (Rignot, 2006). Close to the grounding line of the Dotson Ice Shelf, grounded ice has been thinning for the past 20 years, at a mean rate that exceeds 1.5 m/yr (Shepherd *et al.*, 2002; Pritchard *et al.*, 2009). Between 1992 and 2001, satellite altimeter observations of ice shelf surface lowering indicated that the ice shelf thinned at an average rate of 3.3 ± 0.4 m/yr (Shepherd *et al.*, 2004). By assessing the contributions from the various processes affecting surface lowering (namely temporal fluctuations in sea level height, ocean density, ice shelf density, surface mass accumulation, and ice mass flux divergence), Shepherd *et al.* (2004) estimated an average net basal melt rate underneath the Dotson Ice Shelf of ~ 8 m/yr.

5.5 Data

5.5.1 Interferometric Synthetic Aperture Radar

In this study I used SAR data acquired by the European Remote Sensing satellites (ERS-1/2) to determine ice shelf motion. The SAR data were acquired during the first and second ice phases of ERS-1 (during early 1992 and early 1994, respectively), and the ERS-1/2 tandem phase (1995-1996) (tables 5.1 and 5.2). The SAR data were acquired in raw format and processed using the Gamma software package (Werner *et al.*, 2000). I used a 5-km Antarctic-wide DEM (Bamber and Bindschadler, 1997) to simulate and remove the topographic

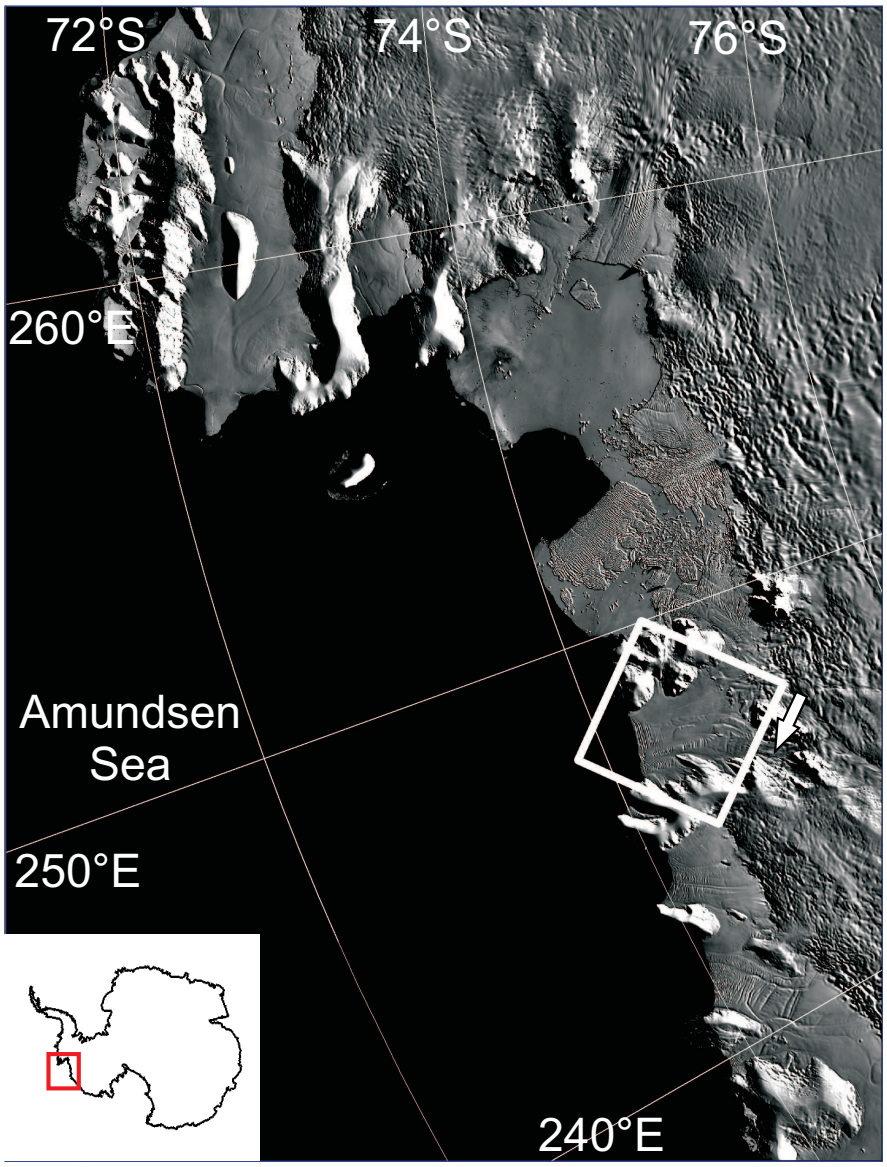

Figure 5.1: The Dotson Ice Shelf, West Antarctica. Thick white outline indicates SAR data coverage over the Dotson Ice Shelf, white arrow indicates the range (across-track) direction of the satellite. Background image is taken from the MODIS mosaic of Antarctica (Haran *et al.*, 2006).

component of the interferometric phase. The effect of DEM inaccuracies is considered in section 5.7.

Table 5.1: Single-difference synthetic aperture radar data, e1 signifies ERS-1 satellite. $B_\perp$ specifies the perpendicular baseline of the interferometer.

A. Interferometric Data					
Image pair (sensor-orbit-frame)	**Ice shelf**	**Reference image acquisition**	**Image pair temporal separation**	**Track**	**$B_\perp$**
e1-13153-5182 / e1-13196-5182	Dotson	20 Jan 1994	3 days	39	17 m
e1-13239-5182 / e1-13282-5182	Dotson	26 Jan 1994	3 days	39	-196 m
e1-13325-5182 / e1-13368-5182	Dotson	1 Feb 1994	3 days	39	44 m
e1-13626-5182 / e1-13669-5182	Dotson	22 Feb 1994	3 days	39	-23 m
e1-13798-5182 / e1-13841-5182	Dotson	6 Mar 1994	3 days	39	-2 m
B. Tracking Data					
e1-13153-5182 / e1-13368-5182	Dotson	20 Jan 1994	15 days	39	-

5.5.2 Tide Models

I used three tide models to simulate the effect of ocean tides on the InSAR observations: the Circum-Antarctic Tidal Simulation, Inverse Model Version 2008a (CATS2008a_opt), TPXO7.1 (Egbert and Erofeeva, 2002) and the Finite Element Solution model FES2004 (Lyard *et al.*, 2006) (hereafter referred to as CATS, TPXO and FES). CATS is an updated version of the regional inverse model described by Padman *et al.* (2002). These models (or their predecessors: CATS02.01 and TPXO6.2) are among the most accurate around Antarctica, with root mean square errors of 6-17 cm, based on a comparison with tidal records (4 major tidal constituents only) (King and Padman, 2005).

The tide models considered here are built on different sized grids. FES and TPXO are both global tide models, with 1/8° and 1/4° resolution respectively (equating to a resolution of the order of tens of kilometres at the latitude of this study). CATS is a high resolution regional model, for the waters around Antarctica only, and operates at a 4 km grid spacing. All 3 models assimilate remotely

Table 5.2: Double-difference synthetic aperture radar data, e1 and e2 signify ERS-1 and ERS-2 satellites. $B_\perp$ specifies the effective perpendicular baseline, and is calculated as the difference between the perpendicular baselines of the two component interferograms.

Image pair (sensor-orbit-frame(s))	Ice shelf	Reference image acquisition	Image pair temporal separation	Track	$B_\perp$
e1-03318-5182 / e1-03361-5182	Dotson	4 Mar 1992	3 days	39	57 m
e1-03404-5182 / e1-03447-5182		10 Mar 1992	3 days	39	
e1-13153-5182 / e1-13196-5182	Dotson	20 Jan 1994	3 days	39	82 m
e1-13196-5182 / e1-13239-5182		23 Jan 1994	3 days	39	
e1-13153-5182 / e1-13196-5182	Dotson	20 Jan 1994	3 days	39	214 m
e1-13239-5182 / e1-13282-5182		26 Jan 1994	3 days	39	
e1-22400-5176 / e2-02727-5176	Dotson	27 Oct 1995	1 day	368	141 m
e1-24404-5176 / e2-04731-5176		15 Mar 1996	1 day	368	
e1-23817-5175-5193 / e2-04144-5175-5193	Dotson	3 Feb 1996	1 day	282	39 m
e1-24318-5175-5193 / e2-04645-5175-5193		9 Mar 1996	1 day	282	
e1-23885-5601 / e2-04212-5601	Crosson	8 Feb 1996	1 day	350	-80 m
e1-24386-5601 / e2-04713-5601		14 Mar 1996	1 day	350	

sensed and ground-based data in order to constrain their physical forward model. FES utilises sparse Antarctic tide gauge data (less than 10 records), along with TOPEX/Poseidon and ERS altimetry. TPXO assimilates TOPEX/Poseidon and TOPEX tandem radar altimetry, and Antarctic tide gauge data. CATS is forced by tide heights from TPXO at its northern boundary, and assimilates TOPEX/Poseidon altimetry, ~ 50 tidal records and ICESat laser altimetry from the Ross and Filchner-Ronne ice shelves. I used the load tide model TPXO6.2_load (Egbert and Erofeeva, 2002) to correct CATS and TPXO for the ocean floor deformation associated with the tidal displacement of water (this correction is included within FES).

5.5.3 Meteorological Model Reanalysis

To account for ice shelf height changes arising from atmospheric pressure fluctuations I used surface level atmospheric pressure data from the European Centre for

Medium-Range Weather Forecasts' (ECMWF) ERA-40 reanalysis (Uppala *et al.*, 2005). These data were acquired from the British Atmospheric Data Centre on a 1° x 1° regularly spaced grid, which was derived from an N80 reduced Gaussian grid. ERA-40 provides surface pressure fields at six-hourly intervals and so I used a linear interpolation between the two closest times to derive pressure estimates at the times of SAR data acquisition.

5.6 Methods

In this section I describe the practical application of the theoretical approach outlined in section 5.3. I begin by detailing the processing steps of my single-difference and double-difference techniques. I then describe how I compare my results to tide model predictions.

5.6.1 Single-Difference Technique

I formed multiple interferograms from co-registered SAR image pairs (table 5.1), and then used estimates of surface displacement determined using SAR intensity tracking to approximate, and remove, the flow signal recorded within each interferogram (equation 6.3). This provided a map of tidal displacement over the ice shelf, subject to the coverage provided by my InSAR and tracking observations. In the following sections I describe the main stages of this process. Maps showing the coverage obtained are shown in section 5.8.

SAR Intensity Tracking

Previous studies (Werner *et al.*, 2001; Strozzi *et al.*, 2002; Luckman *et al.*, 2003) have demonstrated that surface displacement can be mapped from a pair of co-registered SAR backscatter intensity images, by tracking the motion of features in the two images. The data processing can be divided into two main stages; image co-registration and displacement mapping. In the first step, images must be accurately co-registered, in order to minimise the misinterpretation of image co-registration errors as surface displacement. In the second step, small subsections (also known as *patches*) of the two images are matched in order to determine displacement offsets.

Both image co-registration and the estimation of surface displacement utilise the same cross-correlation technique, and so care must be taken in the co-registration step to avoid mistakenly accounting for a component of the surface displacement field. In situations where major sections of the imaged area are stationary during the acquisition period, accurate co-registration can be achieved by estimating the offsets of large-scale features over the entire image, and culling anomalous values which may include ice motion (Pritchard *et al.*, 2005). However, only a small proportion of my study area exhibits such stability, with the majority of the imaged area consisting of moving ice or ocean. Consequently, performing a standard co-registration based upon offsets acquired over the whole image does not satisfactorily eliminate regions of surface motion from the co-registration procedure (figure 5.2).

I therefore applied a mask prior to co-registration so that co-registration was based solely on non-moving areas (figure 5.3). Because these areas were not extensive, I based my co-registration upon offsets compiled from two patch sizes, enabling me to exploit a range of different sized features and increase the number of offsets used. Bilinear functions of range and azimuth pixel number were fitted

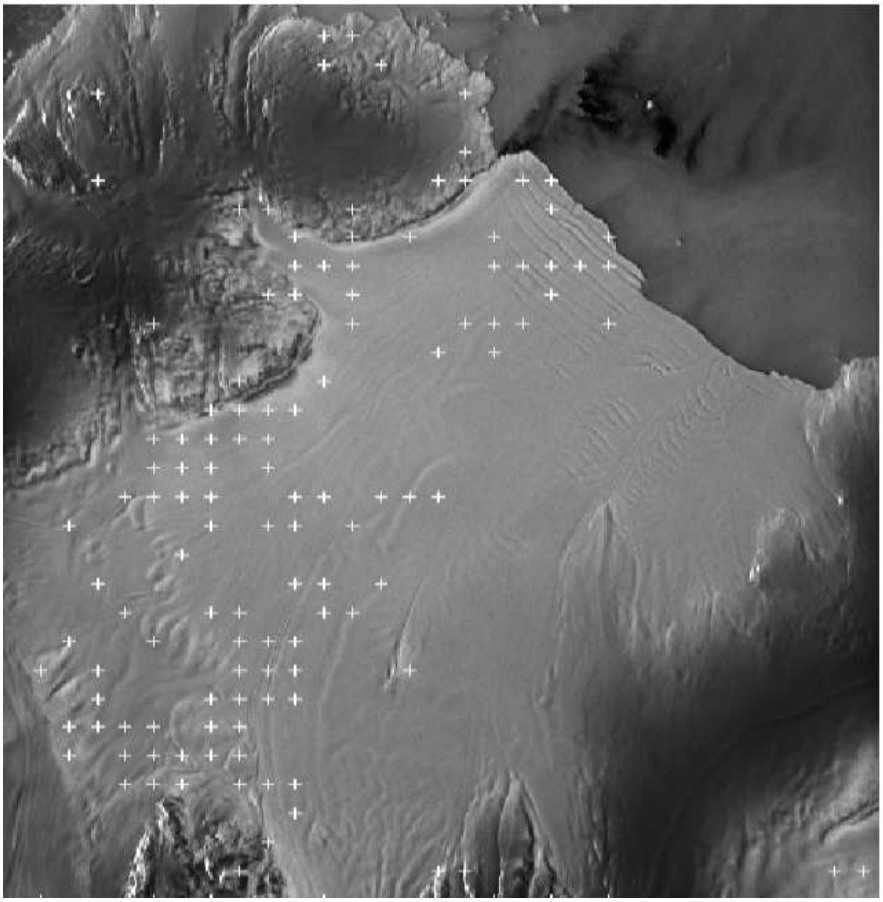

Figure 5.2: Location of co-registration offsets determined using a standard cross-correlation procedure over the entire image domain, for a pair of ERS-1 SAR images acquired on 20th January and 4th February 1994. The white crosses mark locations of co-registration offsets, and the background image is an ERS-1 backscatter intensity image of the Dotson Ice Shelf, displayed in range-doppler co-ordinates. Many of the co-registration offsets are located on moving ice and so surface displacement will affect the co-registration procedure.

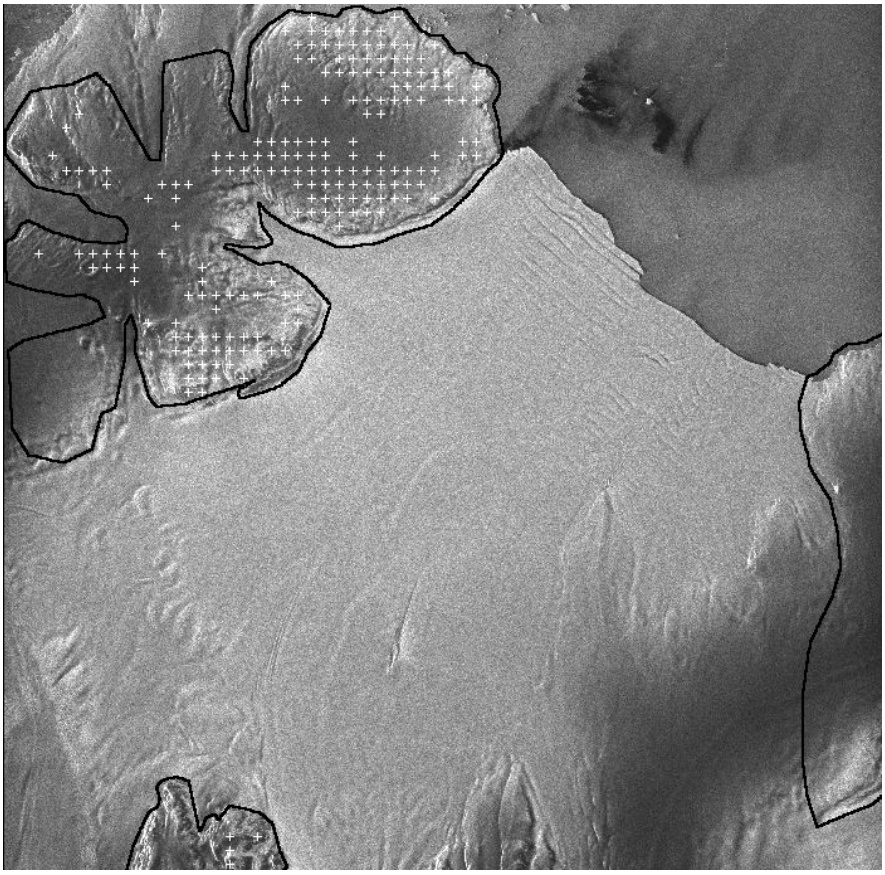

Figure 5.3: Location of offsets used to co-register images acquired on 20th January and 4th February 1994. Offsets were determined only over regions identified as stationary. White crosses mark locations of co-registration offsets, black lines bound the stationary regions which the co-registration was limited to. The background image is a backscatter intensity image of the Dotson Ice Shelf, displayed in range-doppler co-ordinates.

to these offset estimates in order to perform image co-registration. I chose not to fit a higher order polynomial because (1) the data points used to determine the polynomial were limited in extent and irregular in their spatial distribution throughout the image (figure 5.3), and (2) a first-order polynomial is sufficient to represent the principle transformations required to co-register ERS data (namely image shifts, stretches and small rotations).

Once images were co-registered, I performed SAR intensity tracking to produce a displacement map with a nominal pixel spacing of $\sim$ 240 x 200 metres. To determine displacement, I cross-correlated patches with dimensions of 128 pixels in range and 512 pixels in azimuth ($\sim$ 2.6 x 2.0 km in ground co-ordinates). Tracking features of this size maximised the area over which a coherent displacement signal was retrieved. Smoothing of the displacement map was not necessary at this point because I spatially average displacement estimates at a later stage, as part of my method to measure tidal displacement. Finally, I identified and masked regions of noise (i.e. spatially incoherent signal), based upon the deviation of each pixel value from the local mean. During the ice phase of the ERS-1 mission, images of the Dotson Ice Shelf were acquired at regular 3-day intervals, allowing me to form a series of displacement maps from image pairs acquired over a range of time-scales. From these data, I selected the image pair for this study (table 5.1, 15-day separation) that maximised the area over which I obtained a coherent displacement signal.

InSAR

Taking each interferogram, I firstly isolated the displacement component of the interferometric signal (equation 5.2). The simulated topographic component, together with the phase signal originating from the changing look angle across the satellite track (the *flat Earth* signal), was projected into the SAR imaging

geometry and removed from each interferogram. During the simulation of the topographic and flat-Earth phase signals, I used precise orbit information acquired from the Technical University of Delft to determine the imaging geometry. Further baseline refinement was not necessary for this study because I only use image-wide averages of relative displacement (see section 5.7 for a further discussion and assessment of the associated error). Each interferogram was smoothed, unwrapped (Goldstein *et al.*, 1988) and converted to a map of displacement in the range direction. The InSAR map shows only relative displacement, i.e. how displacement varies across the image. To convert to absolute displacement, these relative displacement values were *tied down* to pixels with known displacement. Commonly, non-moving regions of the image are identified, such as bedrock protruding though the ice or areas of known stagnant flow. These must be linked to the ice shelf by a path that does not cross discontinuities in the interferometric phase. Because I was not confident that I could identify such a path I did not tie down my InSAR displacement maps to stationary regions. Instead I used range displacement values derived using SAR intensity tracking, at locations where ice was grounded, to provide $\sim$ 2400 points of known velocity to tie down each InSAR map. Specifically, I used a displacement map derived using the double-difference technique (see section 5.6.2) to identify grounded regions of ice (figure 5.4). At these grounded locations, I retrieved tracking (range component only) and InSAR displacements, calculated the difference between each tracking and InSAR estimate (figure 5.5) and then shifted the InSAR solution so that the mean difference between the set of InSAR-tracking pairs was zero (figure 5.6). In this way I used an extensive dataset to tie down my InSAR-derived displacement map.

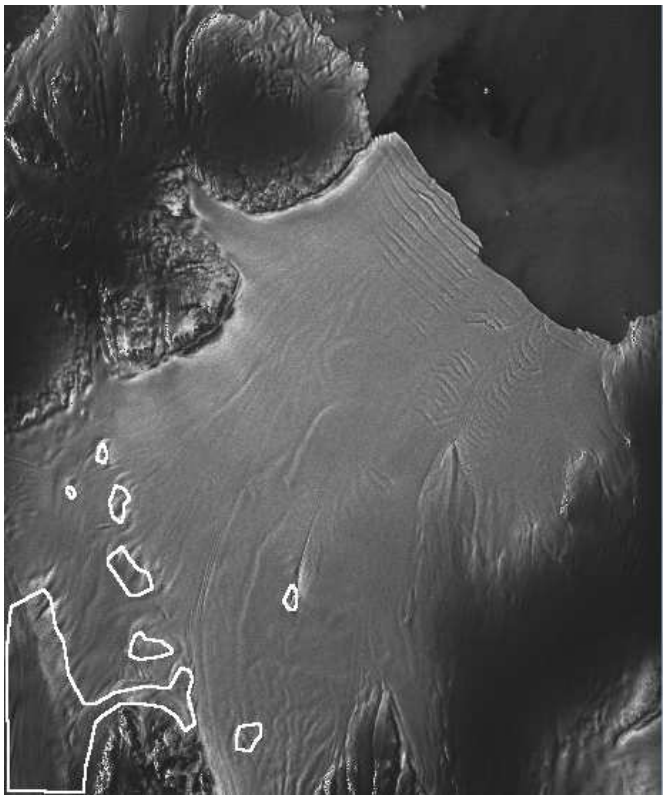

Figure 5.4: Location of grounded regions used to tie down InSAR displacement maps. Grounded regions are the multiple regions bounded by white lines, and were identified using a double-difference technique (see section 5.6.2). The background image is a backscatter intensity image of the Dotson Ice Shelf, displayed in range-doppler co-ordinates.

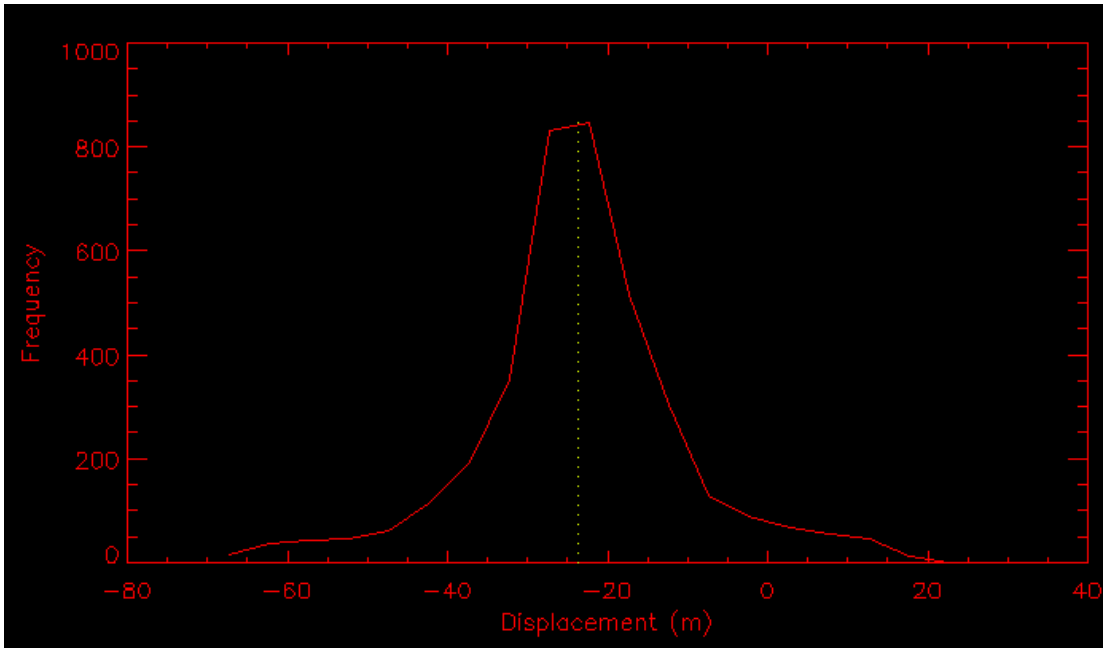

Figure 5.5: Distribution of the differences between tracking and InSAR velocity estimates at grounded locations (figure 5.4). Tracking displacements were calculated over the period 20th January - 4th February 1994 and InSAR displacements over the period 20th - 23rd January 1994. Each have been converted here to equivalent annual displacements. InSAR estimates are tied to an arbitrary point and so these differences are not a measure of the inconsistency between tracking and InSAR estimates. Rather the mean difference, as indicated by the brown dotted line, is used in my method to tie down the InSAR velocities.

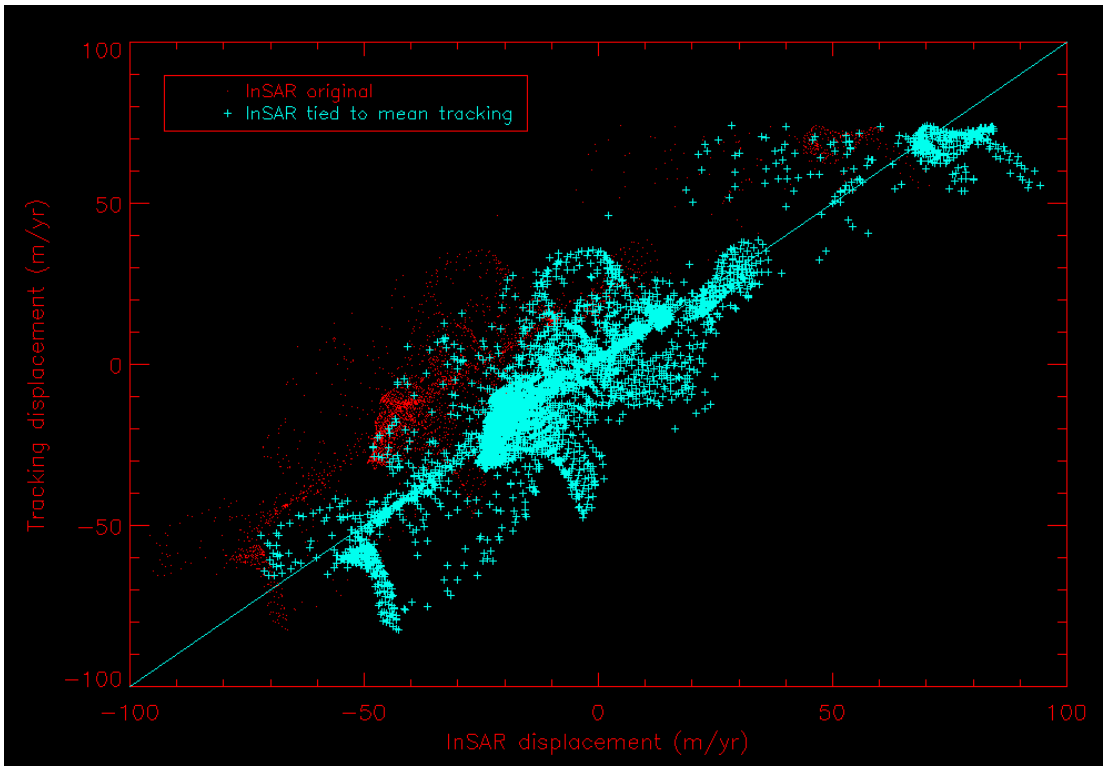

Figure 5.6: Procedure used to tie down InSAR displacements using tracking data. Plotted is a comparison of the InSAR and tracking-derived range velocities derived from the same data as figure 5.5, at locations where the ice was grounded (figure 5.4). The original InSAR data, whose velocities were relative to an arbitrary displacement, are shown in red. To tie down the InSAR velocities, the original velocities were shifted so that the mean difference between tracking and InSAR velocities was zero (blue crosses). This is equivalent to a horizontal shift of the data points so that they are centred on the line of equivalence (blue line).

Removing the Ice Flow Signal

I used the velocities derived by SAR intensity tracking to remove the flow component of the displacement signal from each InSAR displacement map. Because InSAR only measures changes in the satellite's line of sight (range) direction, I used only the component of the tracking displacement in that direction. Differencing each InSAR-derived displacement map and the range component of the SAR intensity tracking displacement map isolated non-steady displacement. This displacement was converted into a vertical motion.

5.6.2 Double-Difference Technique

I formed multiple interferograms from co-registered SAR image pairs (table 5.2), and then differenced pairs of interferograms to isolate the non-steady component of the displacement signal. The procedure outlined in section 5.6.1 was followed to remove topographic and flat-Earth effects, and convert the differenced interferograms to a vertical displacement map.

5.6.3 Tide Model Evaluation

Tide heights were determined from each of the three tide models at the times of the SAR data acquisitions, at a location just seaward of the ice front (74.1°S, 247.5°E, marked in figure 5.1). I did not use model predictions coincident with the ice shelf itself because of inconsistencies between the models at those locations (see section 5.9.2). These predictions were combined so as to give estimates of the tidal signal, as recorded by my single- and double-difference methods. In a similar way, equivalent predictions of the atmospheric pressure signals were formed from the model reanalysis data. These were converted to ice shelf height changes

assuming an inverted barometer response at a rate of -0.95 cm / hPa, which was determined empirically by Padman *et al.* (2003b). These estimates were used to account for ice shelf motion arising from atmospheric pressure fluctuations. The observed mean tidal displacements over a freely-floating portion of the ice shelf (figure 5.7) were then compared to the tide model predictions. Far-range regions (to the right of the black line in figure 5.7) were excluded from my single-difference estimates, because this region suffered from a lack of constraint in the image-pair co-registration used in my tracking solution (figure 5.3). This issue is discussed in further detail in section 5.9. In both the single-difference and double-difference methods of tide model evaluation, I considered only the mean tidal displacement in order to reduce the effect of measurement error (section 5.7). This step sacrifices spatial resolution but allows us to derive a single estimate of tidal displacement with which to characterise each dataset.

5.7 Error Assessment of Single-Difference and Double-Difference Methods

To assess the certainty with which InSAR data can be used to evaluate tide models, and the relative strengths of my two InSAR-based methods, I considered the ability of my methods to completely remove all other signals. I define the error associated with each observation of tide as follows:

$$\varepsilon^2 = \varepsilon_{topo}^2 + \varepsilon_{flat}^2 + \varepsilon_{flow}^2 + \varepsilon_{press}^2 + \varepsilon_{atm}^2 + \varepsilon_{coh}^2 + \varepsilon_{unw}^2 \tag{5.6}$$

where ε_{topo}, ε_{flat}, ε_{flow} and ε_{press} are the errors associated with the incomplete removal of terms in equations 5.2 and 5.3, ε_{atm} is the error arising from atmospheric distortions of the phase signal, ε_{coh} is the error due to loss of signal

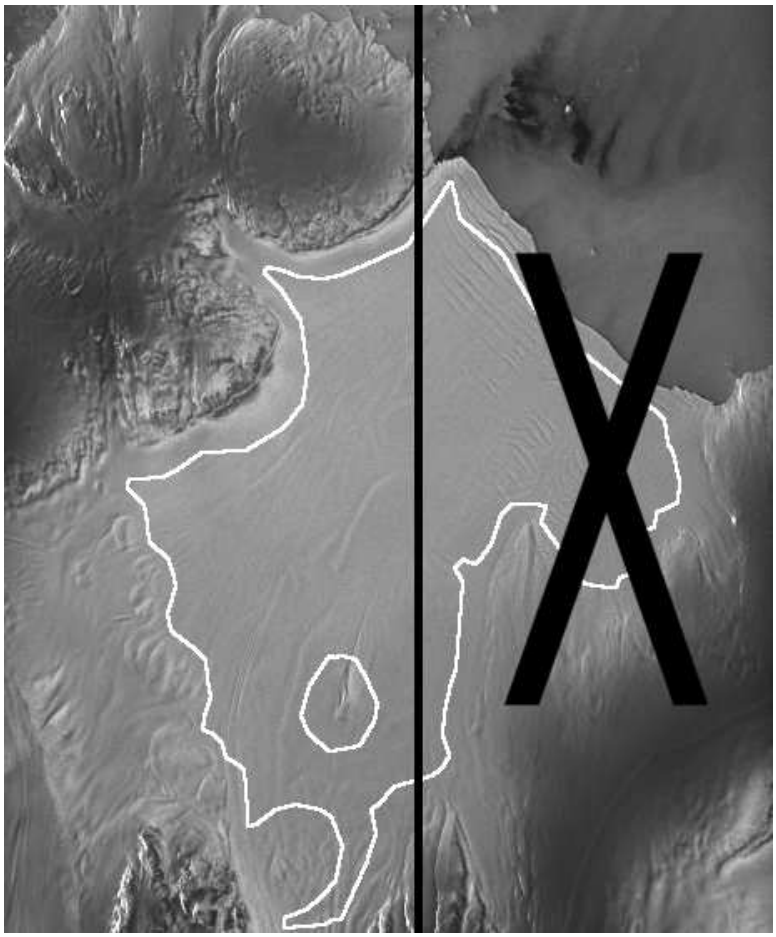

Figure 5.7: Extent of the area of floating ice over which tidal observations were made. The white line bounds the area used in my double difference approach. The black line marks the additional constraint in the range direction placed upon my single difference estimates. This was motivated by the uneven distribution of tracking co-registration offsets (figure 5.3). *X* marks the area discarded, so that the refined area over which single difference observations were made is given by the floating area (bounded by white lines) to the left of the black line. Background image is ERS-1 SAR backscatter intensity image displayed in range-doppler co-ordinates.

coherence between the radar acquisitions and ε_{unw} arises from any error in the unwrapping process. In this section I estimate the magnitude of each of these components; a summary of these error terms is provided in table 3. The errors quoted are the mean values obtained from the datasets used to evaluate each component.

5.7.1 Topographic Error

In this study I have used a DEM to remove the topographic component of the interferometric phase. Spurious topographic phase signals, which will be falsely interpreted as surface displacement, arise from inaccuracies in both the DEM and the baseline estimation (the latter effect causing an incorrect scaling of the DEM when removing the topographic phase). The following analysis of these error terms is based on the work of Joughin *et al.* (1996a). I resolve the baseline, B, into components perpendicular, $B_\perp$, and parallel, $B_\parallel$, to the radar's centre look direction, θ_c. The sensitivity of the interferometric phase to topography can be approximated (Joughin *et al.*, 1996a) as:

$$\varphi_{topo} = \frac{4\pi B_\perp}{\lambda r \sin\theta_c} z \tag{5.7}$$

where r denotes the range from the satellite to the target pixel, and z the elevation of the target pixel above Earth's ellipsoid. If z is determined from a DEM, with an associated error ε_z, then the corresponding error in the interferometric phase will be given by:

$$\varepsilon_z^\varphi = \frac{4\pi B_\perp}{\lambda r \sin\theta_c} \varepsilon_z \tag{5.8}$$

Falsely interpreting this topographic phase error as a surface displacement in the satellite's line of sight direction, and converting to a vertical tidal motion yields:

$$\varepsilon_z^{\Delta z} = \frac{B_\perp}{r \sin\theta_c \; cos\; \psi} \, \varepsilon_z \tag{5.9}$$

where ψ is the incidence angle of the radar beam relative to the normal to Earth's ellipsoid. Taking typical values for the ERS satellites for θ_c, ψ and r of 23°, 26° and 862.5 km respectively, and a relative DEM error of 5 m (Bamber and Gomez-Dans, 2005), based on the average surface slope of ice in my study area, gives the vertical displacement error arising from the DEM as a function of perpendicular baseline:

$$\varepsilon_z^{\Delta z} = 1.65 \; \times \; 10^{-5} \, B_\perp \tag{5.10}$$

This yields mean (maximum in parenthesis) vertical displacement errors, resulting from DEM inaccuracies, of 0.1 cm (0.3 cm) and 0.2 cm (0.4 cm) for my single-difference (table 5.1) and double-difference (table 5.2) datasets, respectively.

To determine the effect of the second form of topographic error, that of inappropriate scaling of the topographic phase, I rewrite equation 5.9 as a function of the perpendicular baseline error:

$$\varepsilon_{B_\perp}^{\Delta z} = \frac{z}{r \sin\theta_c \; \cos\psi} \varepsilon_{B_\perp} \tag{5.11}$$

I assume the spatially uncorrelated component (i.e. no correlation between repeat orbits) of the across-track and radial precision orbit errors to be 8 cm and 5 cm, respectively (Hanssen, 2001). Based upon the satellite geometry, I project this

error vector into the perpendicular baseline direction to determine a 9 cm orbital error in that direction, and a $\sqrt{2} \times 9 = 13$ cm perpendicular baseline error. Using the ERS orbit parameters outlined above, and a mean ice elevation (determined from the DEM) in my study region of 75 m, I estimate $\varepsilon_{B_\perp}^{\Delta z}$ as 2×10^{-3} cm, which is insignificant in comparison to the topographic error resulting from DEM inaccuracies. Combining the two sources of topographic error gives mean single-difference and double-difference errors of 0.1 cm and 0.2 cm respectively. The topographic error is small because of the minimal relief of the ice surface at my study site.

5.7.2 Flat Earth Correction Error

Errors in removing the flat Earth phase signal arise from inaccuracies in estimating the interferometric baseline. Here, I start with the approximation determined by Joughin *et al.* (1996a) from the interferometric geometry:

$$\varepsilon_{flat}^{\varphi} = \frac{4\pi}{\lambda}(\varepsilon_{B_\perp} \sin\theta_{d,flat} + \varepsilon_{B_\parallel} \cos\theta_{d,flat}) \tag{5.12}$$

where $\varepsilon_{flat}^{\varphi}$ is the flat Earth phase error, $\varepsilon_{B_\perp}$ and $\varepsilon_{B_\parallel}$ are the errors in estimating the perpendicular and parallel components of the baseline, and $\theta_{d,flat}$ is the angular deviation from the centre of the radar beam across the image swath, assuming no topography. Two factors are important here: (1) I measure the displacement of floating ice relative to grounded ice, and (2) to mitigate the effect of the perpendicular baseline error I have taken spatial averages over each of the grounded and floating regions of ice, to determine a single estimate of tidal displacement at each epoch. Consequently, the displacement error resulting from unmodelled baseline effects is determined by the change in the mean baseline error between the grounded (figure 5.4) and floating (figure 5.7) regions of ice. Across the image track, the parallel baseline error term remains effectively constant, and

so will not contribute to $\varepsilon^{\varphi}_{flat}$. The perpendicular baseline error term contributes an almost linear phase ramp across the image swath, with zero error at the centre line of the swath ($\theta_{d,flat} = 0$). Consequently, the contribution of this term to my total error will be determined by the phase change associated with this ramp, occurring between grounded and floating regions. From these considerations I ignore the parallel baseline term and re-write equation 5.12 as:

$$\varepsilon^{\varphi}_{flat} = \frac{4\pi}{\lambda}\varepsilon_{B_\perp} \sin(\langle\theta_{d,fl}\rangle - \langle\theta_{d,gr}\rangle) \tag{5.13}$$

where $\langle\theta_{d,fl}\rangle$, $\langle\theta_{d,gr}\rangle$ are the mean angular deviations of floating and grounded ice regions, respectively. Over my study area, $\langle\theta_{d,fl}\rangle - \langle\theta_{d,gr}\rangle = 3.2°$. In essence, this angle expresses the difference in range position between the grounded and floating regions of ice (figures 5.4 and 5.7). This separation, combined with the phase gradient deriving from the baseline error, provides an estimate of the baseline error phase shift between grounded and floating regions, which will incorrectly be interpreted as tidal motion.

As before (section 5.7.1), I assume a 13 cm error in the perpendicular baseline estimate, which equates to a $\sqrt{2} \times 13 = 18$ cm error in my double-difference baseline estimates. Applying equation 5.13, and converting to a vertical displacement, yields flat Earth errors of 0.8 cm and 1.1 cm for my single-difference and double-difference approaches, respectively.

5.7.3 Ice Flow Error

Single-Difference Method

As part of my single-difference method, I removed the flow component of the interferometric signal using estimates determined from SAR intensity tracking. Errors in cancelling the flow signal may arise from errors in my tracking displacement map. Specifically, high frequency noise may arise from inaccuracies in matching image patches using the intensity tracking technique, and errors in the SAR image pair co-registration may contribute long wavelength errors. In this study I mitigate the effect of high frequency noise by spatially averaging displacement estimates over the ice shelf. However, long-wavelength co-registration errors in my tracking estimates will contribute a spurious signal to my estimates of single-difference tidal displacement. I estimate this error, $\varepsilon_{flow}^{\Delta z}$, by converting to a vertical displacement the mean line-of-sight displacement of pixels which are located on stable ground (and hence should exhibit no displacement):

$$\varepsilon_{flow}^{\Delta z} = \frac{\langle \Delta r_{stable} \rangle}{\cos \psi} \tag{5.14}$$

where $\langle \Delta r_{stable} \rangle$ denotes the mean line-of-sight displacement of stable pixels and ψ is the incidence angle of the radar beam. From this calculation I determine a 6.5 cm ice flow error in my single-difference measurements of vertical tidal displacement. Incomplete cancellation of the flow signal may also arise from flow variations occurring during the different length sampling periods (3 days for InSAR versus 15 days for tracking). Without independent high-quality velocity measurements (e.g. from in situ Global Positioning System data) I cannot directly quantify this effect. However, I have aimed to minimise any influence by (1) forming InSAR and SAR intensity tracking predictions from contemporaneous

data, and (2) measuring displacement relative to grounded ice close to the grounding line, which itself is likely to undergo similar variations in flow to that of the ice shelf, given the relatively long wavelength of previously observed flow modulation signals (Gudmundsson, 2006).

Double-Difference Method

I do not utilise velocities determined from SAR intensity tracking when estimating tidal motion using the double-difference approach, and so the only source of ice flow errors are those that may potentially arise from non-steady variations in flow. Specifically, errors in my double-difference tidal predictions could arise if the total displacement occurring during an interferogram acquisition (i.e. 1- or 3-day displacement) varies between the first and second interferograms. Although not strictly flow, I also consider here any transverse motion of the ice shelf (as described in section 2.4.3), as this will similarly lead to inaccuracies in my estimates of vertical tidal motion. Importantly, the Dotson Ice Shelf is bounded by land at its lateral margins (figure 5.1). In contrast, transverse motion has only been observed on laterally unconstrained ice shelves (Doake, 2002; Legresy *et al.*, 2004) where the tide can enter the ice shelf cavity at its lateral margins, and the ice shelf has space to flex in a transverse direction. In view of this, I believe that my observations will not have a transverse-motion component to them and so I assume no corresponding error contribution. To investigate the prevalence of a signal arising from the longitudinal modulation of flow, I checked my double-difference displacement maps for long-wavelength displacement variation indicative of a residual flow signal. Spatial variation in displacement over the ice shelf was small ($\sim$ 1 cm on average for my dataset), indicating no significant residual flow signal. I therefore also discount this term in my double-difference error budget.

5.7.4 Atmospheric Pressure Error

Incomplete removal of ice shelf height changes associated with atmospheric pressure fluctuations will result from inaccuracies in model predictions of atmospheric pressure, and in particular from a failure to predict the timing of large pressure fluctuations associated with passing weather fronts (Padman *et al.*, 2003b). The scarcity of independent in situ meteorological records in remote regions such as the Amundsen Sea limits the assessment of the accuracy of the model reanalysis upon which my atmospheric pressure correction is based. However, one study (King, 2003), has performed an evaluation of the ECMWF modelled surface level atmospheric pressure in the nearby Bellingshausen Sea, based upon independent field data. Although these data span only a relatively short period (February-May 2001), they agree well with the model predictions. I take the 1.05 hPa standard deviation of the model predictions from the independent observations (King, 2003) as an estimate of the error associated with each model estimate of atmospheric pressure. I then calculate the corresponding error associated with single- and double-difference pressure estimates, and convert these to errors in vertical displacement using the empirical ratio determined by Padman *et al.* (2003b). This yields errors associated with my inverse barometer correction of 1.4 cm and 2.0 cm in my single- and double-difference estimates of tidal motion, respectively.

A second source of error associated with my correction for atmospheric pressure fluctuations arises from the validity of the inverse barometer approximation as a means for converting from pressure to ice shelf height changes. Previous studies (Ponte *et al.*, 1991; Padman *et al.*, 2003b) have shown the inverse barometer approximation to be valid at frequencies lower than ~ 0.5 cycles per day (cpd). At these frequencies the ocean responds to changes in atmospheric pressure such that equilibrium is maintained. Consequently, pressure changes correlate well with sea surface height changes. The repeat times of my satellite observations (tables 5.1

and 5.2) require that I model this effect at 0.3 and 1.0 cpd, and so I am at the limit of the frequency range at which an inverse barometer approximation is valid. As such, it is possible that this correction does not account for the full spectrum of atmospheric pressure-driven height changes, in particular for my double-difference approach which utilises some 1-day repeat data (table 5.2). In section 5.9.3 I further investigate my inverse barometer correction, to determine whether, in light of these limitations, such an approximation is beneficial in reducing atmospheric pressure-related signals.

5.7.5 Atmospheric Distortions

The two primary sources of atmospheric distortions affecting repeat pass interferometry arise from tropospheric delay and ionospheric disturbances. Spatial and temporal tropospheric in-homogeneity causes varying phase delays in the radar signal (Goldstein, 1995; Massonnet and Feigl, 1998), primarily as a result of changing water vapour content. Based upon Global Positioning System data, the effect of the varying state of the troposphere on interferometric measurements has been parametrised (Emardson *et al.*, 2003) over a range of length- and time-scales, by the following expression:

$$\varepsilon_{tropo}^{\Delta r} = cL^{\alpha} + kH \tag{5.15}$$

$\varepsilon_{tropo}^{\Delta r}$ is the line-of-sight displacement error due to tropospheric effects (in mm), c and α vary according to the time-scale of the acquisition, and L and H are the length-scale and height difference, respectively (in km), over which tropospheric variability is estimated. Over the scales relevant to my study (50 km length-scale, 0.1 km height difference, and 3 day time period (corresponding to $c = 2.6$, $\alpha = 0.48$, $k = 3.4$ (Emardson *et al.*, 2003))), equation 5.15 gives tropospheric errors

in my single-difference and double-difference estimates of vertical displacement of 1.9 cm and 2.7 cm respectively. These estimates can be taken as an upper bound for tropospheric error because Antarctic tropospheric water vapour variability, and hence c (Emardson *et al.*, 2003), is likely to be much reduced compared to the Californian study site of Emardson *et al.* (2003) (Trenberth *et al.*, 2005).

Over the spatial and temporal interval for which a SAR illuminates a target, variations in the density of electrons in the ionosphere can modulate the phase signal (Gray *et al.*, 2000) and cause errors in associated displacement measurements. This effect can manifest itself as distinctive *azimuth streaks* in the azimuth component of the co-registration offsets, the coherence image and the interferogram (Joughin *et al.*, 1996b; Mattar and Gray, 2002). I checked each interferogram, its corresponding coherence image and the azimuth component of my tracking solution and found no evidence of such features. Furthermore, I note that (1) at the wavelength of ERS, ionospheric errors are typically sub-centimetre (Mattar and Gray, 2002), and (2) by my spatial averaging I will further minimise any ionosphere effects. Consequently, I do not anticipate any significant ionospheric error in my displacement estimates, and so I disregard this term.

5.7.6 Coherence Error

Interferometric phase errors arise from changes in surface properties occurring between the two SAR acquisitions (Zebker and Villasenor, 1992). For a sufficiently multi-looked image, the corresponding line of sight error, $\varepsilon_{coh}^{\Delta r}$, can be approximated (Rodriguez and Martin, 1992) from an estimate of the local coherence, γ, of the interferometric phase within each multi-looked pixel:

$$\varepsilon_{coh}^{\Delta r} = \frac{\lambda}{4\pi\sqrt{2N}} \frac{\sqrt{1-\gamma^2}}{\gamma} \tag{5.16}$$

where N is the number of looks that are averaged. For each interferogram, I take the spatial mean of $\varepsilon_{coh}^{\Delta r}$ as a measure of this error term. Converting to a vertical displacement yields mean errors of 0.1 cm for my single-difference approach and 0.2 cm for my double-difference approach.

5.7.7 Phase Unwrapping Error

Errors can occur during the process of phase unwrapping when discontinuities in the interferometric phase (arising from noise or high phase gradients) are crossed (Goldstein *et al.*, 1988). I checked each unwrapped interferogram to ensure that there was no evidence of the discontinuities associated with unwrapping error, and consequently I assumed no unwrapping errors to be present in my displacement maps.

5.7.8 Combined Error

A summary of the relative contribution of the component error terms is given in table 5.7.8. Assuming the tropospheric error to be at its upper bound, and combining error terms (equation 5.6) yields estimated errors of 7.0 cm and 3.5 cm in my single- and double-difference estimates of vertical tidal displacement, respectively. Consequently, the double-difference technique provides a more accurate assessment of tide model accuracy, primarily because the method is independent of displacement estimates derived using SAR intensity tracking.

Table 5.3: Summary of error terms. Each term is the average calculated from all interferograms used by that technique.

Error term	Single difference error (cm)	Double difference error (cm)
Topography, ε_{topo}	0.1	0.2
Flat Earth correction, ε_{flat}	0.8	1.1
Flow, ε_{flow}	6.5	0
Inverse Barometer Effect, ε_{ibe}	1.4	2.0
Atmosphere, ε_{atm}	1.9	2.7
Coherence, ε_{coh}	0.1	0.2
Unwrapping, ε_{unw}	0	0
Total, ε	7.0	3.5

5.8 Results

In this section I firstly describe my SAR observations of the flow velocity and tidal displacement of the Dotson Ice Shelf. I then use my observations of tidal motion to evaluate the FES, TPX and CATS tide models.

5.8.1 Observations of Ice Shelf Flow Displacement

I have used the technique of SAR intensity tracking to estimate flow speeds across the Dotson Ice Shelf (figure 5.8a). Although this map provides only partial coverage, it is sufficiently complete to determine that the ice shelf is fed by fast flowing ice from the south-west, which originates from the Smith and Kohler glaciers. Considerable flow variation exists over the ice shelf with velocities exceeding 500 m/yr close to the grounding line, yet falling to $\sim$ 100 m/yr at other locations on the ice shelf. The range component of the tracking-derived ice velocities are required to isolate the tidal signal using the single-difference technique. These are shown in figure 5.8b. In comparison to the range displacement map derived from InSAR (figure 5.8c, also includes vertical

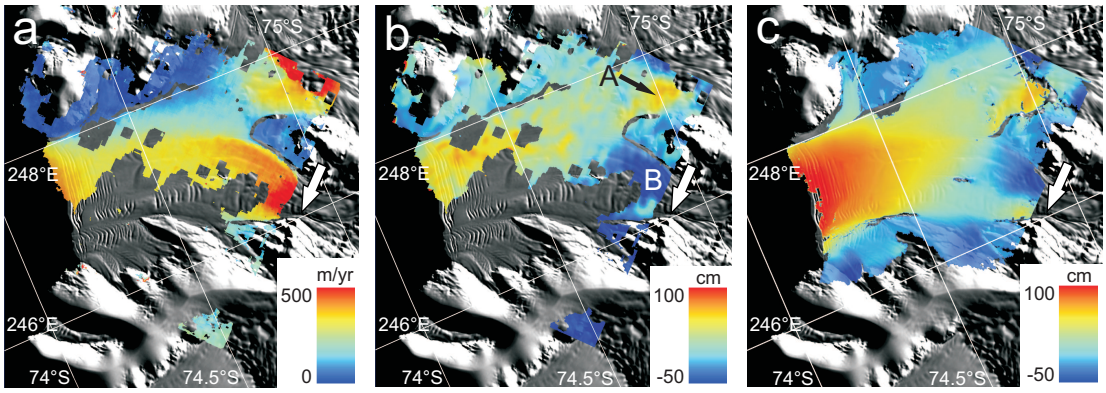

Figure 5.8: Displacement maps of the Dotson Ice Shelf. a) Annual velocity from SAR intensity tracking; b) Range component of 3-day displacement from SAR intensity tracking; c) 3-day range displacement from InSAR. White arrows indicate range direction of satellite; A and B mark fast flowing features referred to in text. Background image is taken from the MODIS mosaic of Antarctica (Haran *et al.*, 2006).

displacement), the SAR intensity tracking map offers more limited coverage and, due to its inferior resolution and precision, a noisier picture of range displacement. It may have been possible to derive a more spatially complete tracking displacement map, using data from an alternative epoch. However, for the purposes of this study, the priority was to obtain a solution contemporaneous with my InSAR data so as to minimise the impact of temporal variations in flow, and complete coverage of the ice shelf was not necessary. A qualitative comparison of the range component of the tracking displacements and the InSAR-derived displacements shows similar large-scale flow displacement patterns. Both resolve the same fast flowing features (marked A and B in figure 5.8b), and a general pattern of increasing displacement towards the calving front of the ice shelf.

5.8.2 Observations of Ice Shelf Tidal Displacement

I made observations of the tidal motion of the Dotson Ice Shelf at multiple epochs using my single-difference and double-difference techniques. I formed five maps of

tidal displacement (e.g. figure 5.9a) using my single-difference technique. These tidal predictions offer only partial coverage of the ice shelf, a consequence of the limited extent of my displacement map derived using SAR intensity tracking. The single-difference tidal maps exhibit substantial long and short wavelength variation, and visually this makes the distinction between floating and grounded ice unclear. There is a long wavelength ramp in each of the five tidal predictions, leading to $\sim$ 1 m variation in the tidal signal across the ice shelf. I discuss the origin of this ramp in section 5.9.1.

I used twenty-four SAR images (table 2) to form six maps of tidal motion (e.g. figure 5.9b) using the double-difference technique. These predictions gave excellent spatial coverage and, in contrast to the single-difference technique, resolved a detailed pattern of floating and grounded ice (blue and red colours, respectively, in figure 5.9b). These solutions indicate a region of grounded ice located between A and B in figure 5.9b, suggesting that a bedrock ridge underlies the ice at this point. This is coincident with a region of slow flow (figure 5.8a). On the freely floating part of the ice shelf, there was little ($\sim$ 1 cm on average) spatial variation in the tidal signal, indicating that the double-difference tide is relatively constant over these length scales, and that there is no residual signal arising from variable flow.

5.8.3 Tide Model Evaluation

I used my single-difference and double-difference tidal observations to evaluate the FES, TPX and CATS tide models at the Dotson Ice Shelf. Comparing my single-difference observations to the equivalent tide model predictions (figure 5.9c) yielded root mean square differences between the observed and modelled tidal displacements of 9.8 cm, 8.8 cm and 8.7 cm for the TPXO, CATS and FES models respectively. The measurement error associated with my single-difference

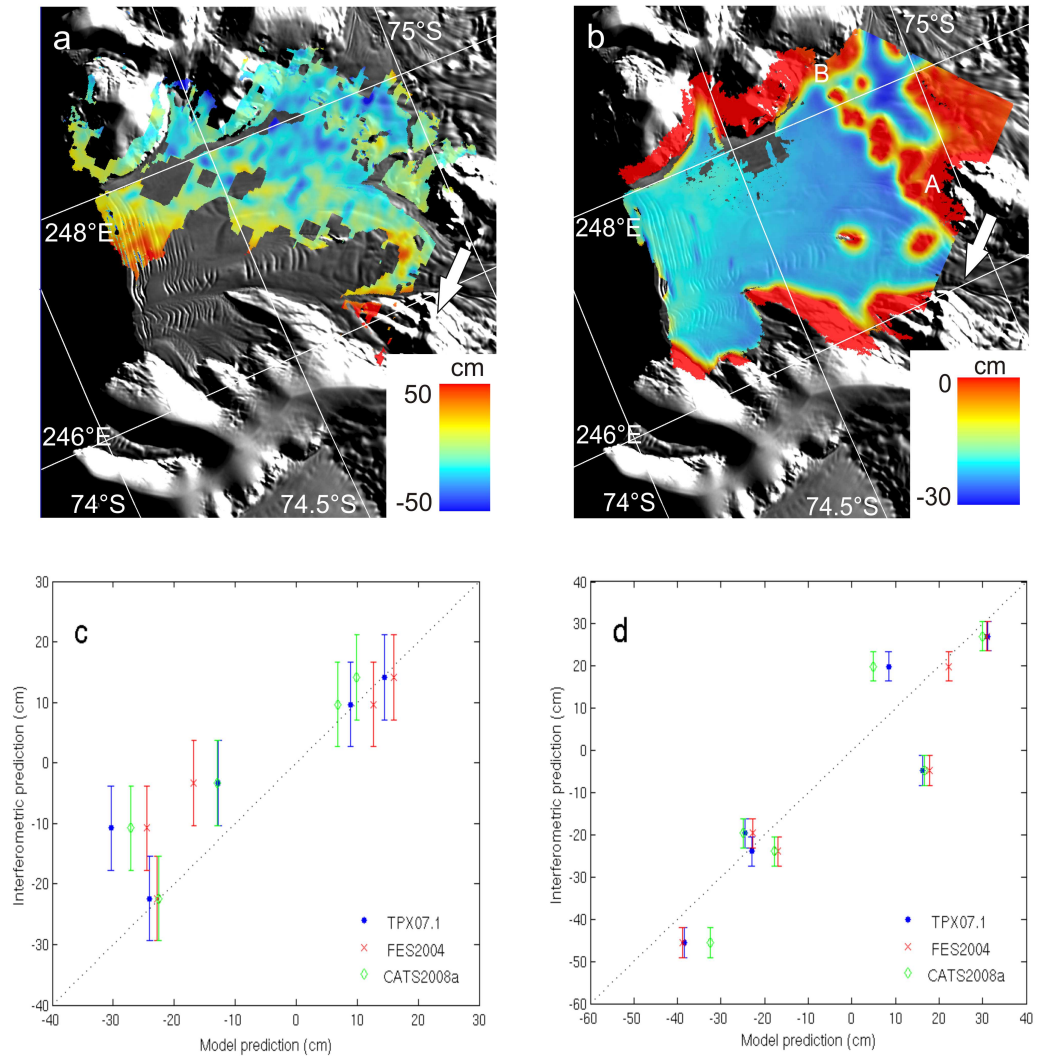

Figure 5.9: Tidal displacement of the Dotson Ice Shelf. a) map of tidal motion determined using single-difference method; b) map of tidal motion determined using double-difference method; c) comparison of modelled and observed single-difference tidal motion, observations determined from multiple SAR image pairs (table 5.1); d) comparison of modelled and observed double-difference tidal motion, observations determined from multiple SAR image pairs (table 5.2). In panels a) and b) the white arrow indicates the satellite's range direction, and the background image is taken from the MODIS mosaic of Antarctica (Haran *et al.*, 2006). In panel b) *A* and *B* bound the locally-grounded areas referred to in section 5.8.2. In panels c) and d) the dashed line indicates equivalence between model predictions and observations, and errors bars represent observational error as determined in section 5.7.

technique is 7 cm (table 3). At three out of the five epochs, the models agreed extremely well with my observations, with only a $\sim$ 2 cm root mean square difference between the two. I have been unable to determine any distinctive circumstances pertaining to these observations, which could explain the apparent distinction between cases of good and poor agreement.

Comparing my double-difference observations to predictions formed from the three tide models (figure 5.9d) gave root mean square differences between the observed and modelled tidal signals of 10.5 cm, 12.4 cm and 10.3 cm for TPXO, CATS and FES respectively. The measurement error associated with my double-difference technique is 3.5 cm (table 3).

5.9 Discussion

In this study I have used two different InSAR-based methods to assess three tide models. In section 5.9.1 I assess the relative strengths of the two evaluation methods, in section 5.9.2 I compare the performance of the three tide models, in section 5.9.3 I consider the benefits of my inverse barometer approximation for pressure-related ice shelf height changes, and in section 5.9.4 I place my results within the context of previous studies.

5.9.1 Comparison of Methods of Observation

I have employed two InSAR-based methods to isolate the tidal motion of an ice shelf; a single-difference method that measures tidal displacement, and a double-difference method that measures changes in tidal displacement. My assessment of measurement error (section 5.7) indicates that both techniques are sufficiently accurate to provide useful information regarding the accuracy

of the current generation of tide models around Antarctica. However, should polar tide model accuracy approach that of the deep ocean (typically 2-3 cm), the techniques presented here would need to be improved if they were to provide the required accuracy for model evaluation. Comparing my two methods, I found that the double-difference technique provided a clearer picture of the tidal signal, consistent with the smaller error associated with this method, and additionally offered better spatial coverage. This analysis indicates that the double-difference method should be used in work that requires a map of tidal displacement, for example when mapping the grounding line of a glacier (e.g. Rignot (1998)).

For certain applications, however, the double-difference method may be unsatisfactory because, in the process of differencing two estimates of tidal displacement, I cancel any systematic error in the model predictions of tidal displacement. An important use of tide models around Antarctica is to simulate the tidal displacement recorded within a single interferogram. This prediction can be used to remove the tidal signal from an interferogram and forms part of a commonly-used interferometric method to map ice shelf flow velocity (e.g. Rignot and Jacobs (2002); Joughin *et al.* (2003); Rignot *et al.* (2004)). In this case, the error in such predictions of flow, resulting from any un-modelled tidal signal, must be quantified. For this purpose a single-difference technique should be applied, so as to account for both systematic and random errors in model predictions of tidal displacement. Accordingly, I can convert my estimate of single-difference tide model accuracy (e.g. 8.7 cm for FES) into an equivalent horizontal displacement error in the ground range direction. This quantifies the uncertainty introduced into the ground range component of model-dependent velocity estimates, should an un-modelled tidal signal of this magnitude be interpreted as a horizontal flow displacement. In this case, my study suggests that tide model inaccuracies will introduce an error of 22 m/yr into such predictions (range component of velocity only).

My analysis has shown that the single-difference technique yields relatively imprecise and noisy observations of tidal displacement. A particular problem with these estimates was the $\sim$ 1 metre amplitude long-wavelength variation in tidal displacement across the ice shelf. Neither my double-difference observations nor the model predictions (section 5.9.2) exhibit a ramp of this magnitude. I therefore conclude that it is an artifact of the processing method used, rather than a real tidal signal. Specifically, I believe it results from errors in my estimation of ice flow (see section 5.7.3), arising from inaccuracies in the co-registration of the image pair used for intensity tracking. This is due to the co-registration function being poorly constrained over some parts of the ice shelf (figure 5.3). To mitigate the effect of the ramp I have refined my method to exclude displacement estimates in regions where the co-registration function is poorly constrained (figure 5.7), specifically the far-range portion of the image where I was unable to determine any co-registration offsets on stationary ground (figure 5.3). Even so, my error analysis suggests that my single-difference measurement error is dominated by errors originating from the co-registration stage of my intensity tracking procedure. This highlights the difficulty of achieving the precision required for tide model evaluations using my single-difference method, particularly at locations lacking stable areas for image co-registration. In other regions, where more extensive stable areas exist, my single-difference technique may provide more precise estimates.

It is possible that additional processing steps could further improve image co-registration. For example, the application of a low-pass filter prior to image co-registration could remove short-wavelength surface features and isolate long-wavelength features originating from sub-ice bedrock topography (e.g. Bindschadler and Scambos (1991)). This could allow a more extensive co-registration dataset to be derived. I do not apply this technique here because of the limited

grounded ice present in my images. An alternative approach to minimise the effect of co-registration error would be to measure ice flow (via intensity tracking) over a longer time period. This would reduce the contribution of co-registration error relative to the measured displacement signal. In this study I found that tracking displacement over a longer time period reduced the area over which a coherent displacement signal could be derived, providing insufficient coverage to determine tidal motion. In areas that exhibit more stable surface characteristics, or alternatively by using lower frequency sensors that penetrate further into the snow pack (such as the L-band radar on-board the Advanced Land Observation System (ALOS) (Rignot, 2008)), it may be possible to reduce the effect of co-registration errors by increasing the time period over which surface features are tracked.

Sensitivity of Tide to Observation Method

The characteristics of the tidal signals recorded by my single-difference and double-difference methods will vary according to the method used and the timespan over which the SAR data were collected (as determined by the satellite repeat time - see tables 5.1 and 5.2). To investigate the impact of these factors upon the amplitude of the tidal signal I simulated the statistics of the single- and double-difference signals from hourly-resolution tide model data spanning the year of 1994 (figure 5.10). When calculating the single- and double-difference tidal signals, I considered the two scenarios relevant to the orbital characteristics of the data used in this study. For my single-difference technique this was the tidal displacement occurring over a 1-day (ERS-1/2 tandem) and 3-day (ERS-1 ice phase) interval. For my double-difference technique I calculated the signals corresponding to (1) a differential interferogram formed from four SAR images, with each acquisition separated by 3 days (hereafter referred to as *3,3 acquisition*

mode); and (2) a differential interferogram formed from two interferograms separated by 35 days, with the component SAR images of each interferogram separated by 1 day (hereafter referred to as *1,35 acquisition mode*). Figure 5.10 indicates that the likely magnitude of the tidal signal will vary depending upon which of the two acquisition modes is being used, and whether single- or double-difference tides are being measured. For both single- and double-difference tides a greater sensitivity to the tidal signal would be expected in the 3,3 acquisition mode, as compared to the 1,35 acquisition mode. This is to be expected since the 1-day sampling period of the 1,35 acquisition mode results in a greater aliasing of the $\sim$ diurnal and semidiurnal tidal constituents. As a result, the 3,3 acquisition mode provides a more comprehensive evaluation of the modelled tidal signal, although it still does not adequately sample all tidal constituents (e.g. S_2, 12 hour period).

For a given acquisition mode, the double-difference technique is likely to resolve a larger tidal signal than the single-difference technique. Consequently, if the aim of a study is to resolve the tidal signal (for example to map the grounding line of a glacier (Rignot, 1998)) then it would be preferable to use 3,3 acquisition mode data, along with a double-difference technique. Conversely, if the aim is to minimise the tidal signal, say for estimating ice flow using a single interferogram, then 1,35 acquisition mode data is a better choice.

5.9.2 Comparison of Tide Models

The three tide models considered here predict the amplitude of the observed single- and double-difference tidal signals with comparable accuracy. In both cases FES marginally outperformed the other two models, but the difference between models was not large. To assess the extent to which model choice affected the simulated tidal amplitude, I investigated the spatial and temporal consistency of

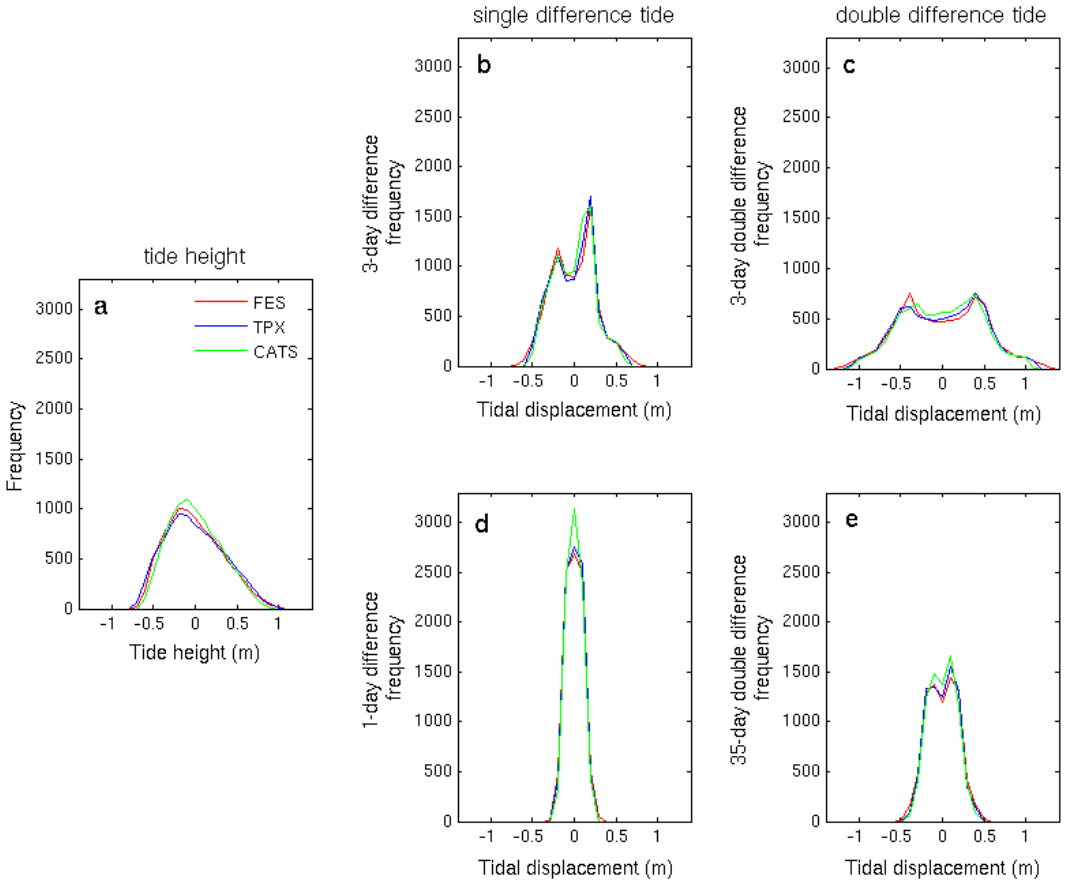

Figure 5.10: Distribution of hourly modelled tide predictions at the Dotson Ice Shelf, 1994. a) tide height; b) difference in tide height over a 3 day period (i.e. the tidal signal recorded by a 3-day interferogram); c) double-difference in tide height (i.e. the tidal signal recorded in a differential interferogram, formed from 4 consecutive SAR images, each separated by 3 days); d) difference in tide height over a 1 day period (i.e. the tidal signal recorded in a 1-day interferogram); e) double-difference in tide height (i.e. the tidal signal recorded in a differential interferogram, formed from two 1-day interferograms, with a 35-day separation between the two interferograms).

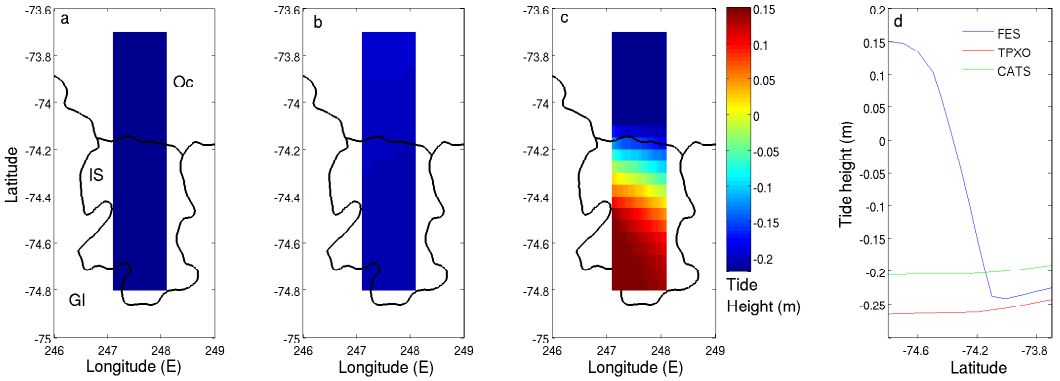

Figure 5.11: Model predictions of tidal displacement at the Dotson Ice Shelf, at 14:50 hrs on 3rd February 1996. Thick black line in a) - c) separates the ocean (*Oc*), the ice shelf (*IS*) and grounded ice (*GI*). a) TPXO; b) CATS; c) FES; d) north-south transect of modelled tide heights along 247.5°E. The spatial extent of predictions are limited to that of FES model domain.

the FES, TPXO and CATS tide model predictions in the vicinity of the Dotson Ice Shelf.

Figure 5.11 illustrates the spatial variability in the tidal amplitude predicted by the three models. Maps of single- and double-difference tidal displacement exhibited similar spatial patterns. Seaward of the ice shelf front, predictions from the three models are relatively consistent. However, upon crossing the ice front, there is a discontinuity in the gradient of the FES solution, and FES tide height rapidly diverges from the other two models. TPXO and CATS retain their consistency over the whole of the ice shelf. Possible sources of the inconsistency of FES may be differing bathymetry used in this region or varying sub-ice shelf water column thickness. Further investigation is required to understand the cause of this discrepancy. The agreement between FES predictions and interferometric observations is far greater seaward of the ice front than on the ice shelf itself, suggesting that the on-shelf ramp in FES tide height (figures 5.11c-d) is not a real phenomenon. This motivated my decision to use modelled tide heights from just seaward of the ice front, at 74.1°S, 247.5°E (figure 5.1). This is not problematic for this work, but in studies where the pattern of tidal displacement over the ice

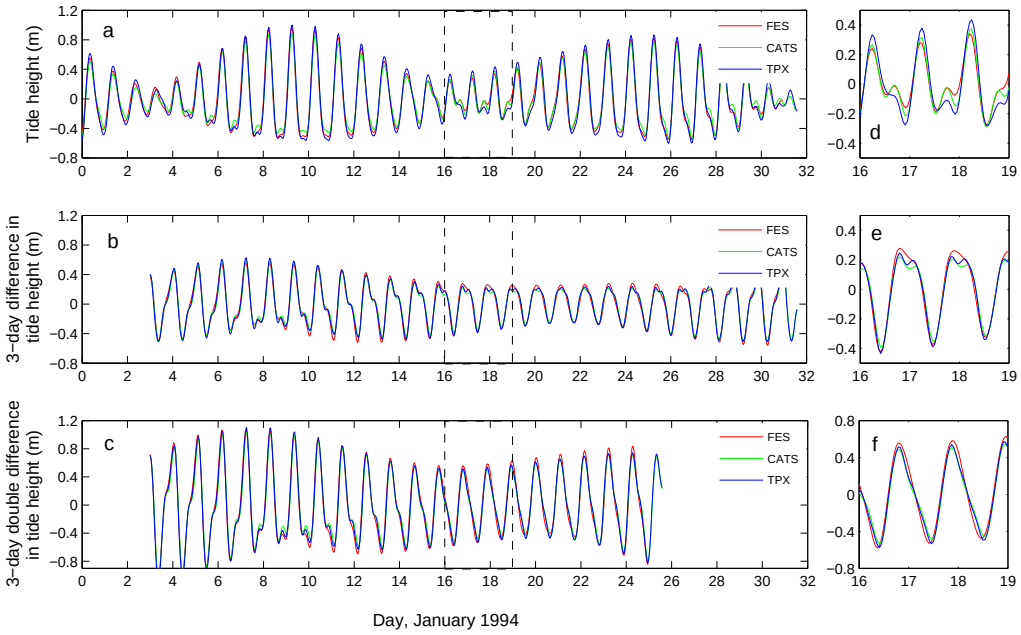

Figure 5.12: Temporal variability of modelled tide predictions at the Dotson Ice Shelf. a) - c) January 1994; d) - f) 3 day period indicated by dashed lines in a) - c) showing differences between models. a) and d) tide height; b) and e) difference in tide height over a 3 day period (i.e. the tidal signal recorded in a 3-day interferogram); c) and f) double-difference in tide height (i.e. the tidal signal recorded in a differential interferogram, formed from 2 consecutive 3-day interferograms).

shelf is being modelled, it would be worthwhile checking the consistency of FES with other models, and may provide a reason to favour CATS or TPXO. I note that a similar assessment of FES95.2 at the Filchner-Ronne Ice Shelf (Rignot *et al.*, 2000) found no such discrepancy, and so this issue may only pertain to small ice shelves.

Next I assessed the temporal consistency of model predictions of tide height, and of the tidal signals isolated by my single-difference and double-difference methods. Using results from the three tide models, I formed time series of tide height, 3-day tide height difference, and the double-difference in tide height for a month-long period coincident with part of my SAR dataset (figure 5.12). All three tide models were generally in good agreement in predicting both the amplitude

and the phase of the tidal signal. Inter-model variability was further reduced by both differencing and double-differencing the tidal signals (figures 5.12d-f). This analysis is consistent with the results of my InSAR-based model evaluation (section 5.8.3), which showed little difference in the performance of the three models. Over the month-long period considered here, the longer-period (greater than diurnal) variability was reduced in the differenced, and double differenced, tidal signal. This analysis (figure 5.12) also indicates that semidiurnal tides are relatively weak at the Dotson Ice Shelf.

5.9.3 Assessment of Inverse Barometer Correction

In situations where in situ meteorological records are located close to the study site, an inverse barometer correction based upon such measurements can substantially improve InSAR-based assessments of tide models (Padman *et al.*, 2003b). What has been less clear is whether, in the absence of such records, model data are sufficiently accurate to merit being used as the basis for inverse barometer corrections. Additionally, previous studies (e.g. Ponte *et al.* (1991)) have indicated that an inverse barometer model may not be appropriate over the 1-day timescales at which some of my data (table 5.2) were collected. To investigate these issues, I compared my single- and double-difference results, both with and without inverse barometer corrections. I found that, for all models considered here, and for both the single- and double-difference results, the inclusion of the correction improved the agreement between observations and model predictions by an average of 6 %. This suggests that the accuracy of model reanalysis pressure fields and the validity of the inverse barometer approximation are sufficient to model, at least in part, ice shelf displacement arising from atmospheric pressure changes over these timescales. It is possible that a more sophisticated model-based

correction for atmospheric pressure loading (e.g. Carrere and Lyard (2003)) may provide further improvement over short timescales.

5.9.4 Comparison to Previous Work

To my knowledge, only one study (Rignot, 2002a) has provided an evaluation of tide model predictions in the Amundsen Sea. My results find a similar degree of agreement between double-difference observations and model predictions to that of Rignot (2002a). Studying the nearby Pine Island Ice Shelf, Rignot (2002a) found the accuracy of FES99 (a predecessor of FES2004) double-difference predictions to be 9 cm. Here I find the equivalent (no inverse barometer correction) root mean square difference to be 10.6 cm. Other tide model evaluations have been conducted around Antarctica, based upon both remote sensing (Padman *et al.*, 2003a) and in situ (King and Padman, 2005; King *et al.*, 2011) data. Variations in these error estimates arise because of differences in (1) the models evaluated, (2) the evaluation methods used, (3) the error metric chosen and (4) the tidal characteristics of the region in which the analysis was performed. Nonetheless, the studies conducted by Rignot (2002a), Padman *et al.* (2003a), King and Padman (2005) and King *et al.* (2011), together with the work described here, paint a broadly consistent picture of approximately decimetre-level tide model accuracy in Antarctic coastal waters.

5.10 Conclusions

In this study I have developed InSAR-based estimates of ice shelf tidal motion in order to assess the accuracy with which ocean tide models can predict ice shelf tidal motion in remote regions of Antarctica. Firstly, I used a single-difference

technique to assess the ability of tide models to predict changes in tide height. Secondly, I used a double-difference technique to evaluate model predictions of the difference between two tidal displacements. Comparing these two methods, I find that the double-difference technique, with a 3.5 cm measurement error, provides a more accurate assessment of tidal displacement. Three tide models (TPXO7.2, CATS2008a_opt and FES2004) perform comparably well, with root mean square deviations from observations of $\sim$ 9 cm (single-difference technique) and $\sim$ 10 cm (double-difference technique). I find here that FES predictions coincident with the ice shelf itself are not reliable. The inclusion of a model-based correction for atmospheric pressure fluctuations improves the agreement between tide model predictions and observations, suggesting that the accuracy of model reanalysis pressure fields is sufficient to merit the application of such a model-based correction.

The single-difference approach, unlike its double-difference counterpart, directly assesses the accuracy with which tide models can reproduce the tidal signal recorded in an interferogram. This quantifies the tidal error in model-dependent InSAR estimates of ice flow, which results from model inaccuracies in predicting tidal displacement. My study indicates that the tide models considered here can reproduce daily-scale tidally-induced ice shelf height changes in the Amundsen Sea to an accuracy of $\sim$ 9 cm. This would equate to an error of 22 m/yr in the ground range component of the velocity field if this unmodelled tidal signal was interpreted as ice shelf flow. This level of accuracy is comparable to other regions around Antarctica, where there is a higher prevalence of in situ tidal records. The methods described here can be used to evaluate tide models in other remote Antarctic waters.

Chapter 6

Mapping Ice Shelf Flow with Interferometric Synthetic Aperture Radar Stacking

Malcolm McMillan[1], Andrew Shepherd[2], Noel Gourmelen[2], Jeong-won Park[2,3], Peter Nienow[1], Eero Rinne[1], Amber Leeson[2]

A modified version of this chapter is in press with the Journal of Glaciology.

Acknowledgement of contribution: N. Gourmelen and JW. Park processed the MAI interferograms, E. Rinne provided the altimetry data, A. Leeson provided the atmospheric pressure data.

[1]The University of Edinburgh, Drummond Street, Edinburgh, EH8 9XP, UK
[2]The University of Leeds, Leeds, LS2 9JT, UK
[3]Yonsei University, Seoul, South Korea

6.1 Abstract

Interferometric Synthetic Aperture Radar (InSAR) observations of ice shelf flow contain ocean tide and atmospheric pressure signals. A model-based correction can be applied, but this method is limited by its dependency upon model accuracy, which in remote regions can be uncertain. Here I describe a method to determine 2-d ice shelf flow vectors independently of model predictions of tide and atmospheric pressure, by stacking conventional and multiple aperture (MAI) InSAR observations of the Dotson Ice Shelf in West Antarctica. In this way I synthesise a longer observation period, which enhances long-period (flow) displacement signals, relative to rapidly-varying (tide and atmospheric pressure) signals and noise. I estimate the error associated with each component of the velocity field to be ~ 22 m/yr, which could be further reduced if more images were available to stack. With the upcoming launch of several satellite missions, offering the prospect of regular short-repeat SAR acquisitions, this study demonstrates that stacking can improve estimates of ice shelf flow velocity.

6.2 Introduction

Around the coastline of Antarctica, ice shelves provide an interface through which ice is melted by the ocean and the relatively warm coastal air. Through this connection, changes in atmospheric (Vaughan and Doake, 1996) and oceanic (Rignot and Jacobs, 2002; Shepherd *et al.*, 2004) conditions can trigger an ice shelf response which, over decadal timescales, can propagate a dynamic instability hundreds of kilometres inland (Payne *et al.*, 2004). These changes can affect the mass balance of glaciological catchments (Shepherd *et al.*, 2002; Wingham *et al.*, 2009) and as a consequence can accelerate sea level rise. Evidence of the dynamic response of inland ice to changing ice shelf conditions has been observed at several

locations on the Antarctic Peninsula and the Amundsen Sea sector of the West Antarctic Ice Sheet (Rott *et al.*, 2002; Shepherd *et al.*, 2002; De Angelis and Skvarca, 2003; Rignot *et al.*, 2004; Scambos *et al.*, 2004; Rignot *et al.*, 2005; Pritchard *et al.*, 2009). These studies demonstrate how external perturbations in climate can lead to changes in Antarctic Ice Sheet (AIS) mass over relatively short time periods. Several studies have documented ice shelf acceleration prior to collapse (Rignot *et al.*, 2004; Vieli *et al.*, 2007). These highlight the importance of monitoring ice shelf flow velocities, both as an indicator of the stability of the glaciological catchment, and in providing detail of the processes through which ice shelves interact with the atmosphere, the ocean and grounded ice upstream (Joughin and Padman, 2003; Payne *et al.*, 2007; Vieli *et al.*, 2007). Until such mechanisms are well understood, the AIS contribution to future sea level rise remains uncertain.

Over the last two decades, conventional satellite-based Interferometric Synthetic Aperture Radar (InSAR) has provided precise, spatially extensive measurements of ice velocity (e.g. Goldstein *et al.* (1993); Joughin *et al.* (1995, 1996a); Kwok and Fahnestock (1996); Rignot (1996); Lang *et al.* (2004); Rignot *et al.* (2008)). This technique measures displacement in the satellite's line of sight, and so the signal returned from the surface of an ice shelf contains both components due to ice flow (assumed here to be in the horizontal plane) and vertical motion (Goldstein *et al.*, 1993; Rignot, 1996; Rignot and MacAyeal, 1998; Rignot *et al.*, 2000). Over the (typically daily) timescales at which InSAR measurements are best made, vertical displacement deriving both from tidal motion and from changes in atmospheric pressure can be significant relative to the speed at which the ice flows (Rignot *et al.*, 2000; Padman *et al.*, 2003b). Consequently, these signals must be removed in order to determine ice flow velocity with confidence. The response of an ice shelf to atmospheric pressure fluctuations is commonly modelled as an inverted barometer (Padman *et al.*, 2003b) and termed the *Inverse Barometer*

Effect (IBE). Whilst this method has been used to isolate the tidal component of altimetry observations (Padman *et al.*, 2008), no studies have attempted to model and remove this component of the InSAR signal when estimating ice shelf flow. In the case of the tidal component, a tide model is commonly used to simulate this part of the interferometric signal (computed as the difference in tide height at the acquisition times of the two SAR images) (e.g. Rignot and Jacobs (2002); Joughin *et al.* (2003); Rignot *et al.* (2004); Vieli *et al.* (2006)). However, in remote Antarctic regions this method is limited by two factors: (1) modelling tides is challenging, because tide gauge, bathymetric and altimetry data are scarce (Egbert *et al.*, 1994; King and Padman, 2005), and (2) in the absence of *in situ* data, it is difficult to assess precisely the ability of a model to predict changes in tide height over the period of interferometric acquisition (chapter 5). As a consequence, the extent to which unmodelled tidal motion affects these ice shelf flow velocity estimates is uncertain.

Stacking interferograms is routinely used to map solid Earth topography (Sandwell and Price, 1998; Sandwell and Sichoix, 2000) and ground deformation (Zebker *et al.*, 1997; Wright *et al.*, 2001; Gourmelen and Amelung, 2005). When mapping surface deformation, stacking enables a longer observation period to be utilised, and so the magnitude of unwanted atmospheric, orbital and topographic signals is reduced relative to the steady rate of deformation. Here I apply this technique to the problem of mapping ice shelf flow; by stacking I minimise unwanted short period tidal and IBE signals, relative to the steady flow signal. As a consequence, I do not rely on tide or IBE model predictions to map ice shelf flow speeds, and hence eliminate the requirement that any single model realisation of tidal or IBE displacement is sufficiently accurate (or of known accuracy). As with solid Earth applications, by stacking I also reduce atmospheric, orbital and topographic noise.

Stacking interferograms to minimise the tidal component of ice shelf displacement

was originally proposed by Rignot and MacAyeal (1998) in a study of the Filchner-Ronne Ice Shelf. To date, however, mapping ice shelf flow using this approach has primarily been limited by the lack of long sequences of regular, short-repeat SAR acquisitions which lend themselves to this technique. The recent European Remote Sensing satellite (ERS-2) 3-day campaign and the planned Sentinel-1 and Radarsat Constellation satellites offer the prospect of the provision of such data. With a view to these missions, I revisit the ERS data archive to provide a detailed demonstration and assessment of the technique at the Dotson Ice Shelf, in the Amundsen Sea sector of West Antarctica. Specifically, I (1) extend the stacking method so as to resolve 2-d velocity vectors from data acquired from a single viewing direction, by utilising conventional and multiple aperture interferometry, (2) use model statistics to quantify the residual tidal and IBE error in my stacked velocity solution, (3) compare my results to flow predictions determined using a traditional method whereby model predictions are used to remove the tidal and IBE signals, and (4) assess the wider application of a stacking-based approach to future satellite missions.

6.3 Study Area

The Dotson Ice Shelf (figure 6.1) spans an area of approximately 3400 km^2, and is one of several small ice shelves situated along the Amundsen Sea coastline of the West Antarctic Ice Sheet. This region, which contains sufficient ice to raise sea levels by $\sim$ 1.5 m, currently has the greatest mass deficit of all of Antarctica (Shepherd and Wingham, 2007). In the last two decades, satellite observations of this region have revealed ice shelf thinning (Shepherd *et al.*, 2004) and grounding line retreat (Rignot, 1998, 2002a). Additionally, grounded ice upstream has thinned (Shepherd *et al.*, 2002; Pritchard *et al.*, 2009; Wingham *et al.*, 2009) and accelerated (Rignot, 2008). The changes in this region are likely to have

been driven by high rates of ice shelf basal melting, resulting from the intrusion of warm Circumpolar Deep Water into sub-ice shelf cavities (Jacobs *et al.*, 1996; Thoma *et al.*, 2008; Jenkins *et al.*, 2010), via seabed troughs that run across the continental shelf (Nitsche *et al.*, 2007) (chapter 4). Satellite observations indicate that between 1992 and 2001, the Dotson Ice Shelf was thinning at an average rate of 3.3 $\pm$ 0.4 m/yr (Shepherd *et al.*, 2004). Once other factors affecting surface lowering had been accounted for (namely temporal fluctuations in sea level height, ocean density, ice shelf density, surface mass accumulation, and ice mass flux divergence), Shepherd *et al.* (2004) estimated that an average net basal melt rate of $\sim$ 8 m/yr was required to produce this rate of thinning.

6.4 Data

The principle dataset used in this study to demonstrate the stacking method was a sequence of SAR images acquired by the ERS-1 satellite. These data were processed using a range of techniques to provide measurements of ice shelf flow. As part of the InSAR processing, a digital elevation model (DEM) and laser altimetry data were used for the removal of unwanted signals from the SAR data. To determine the errors associated with the stacking technique, and to provide a more general assessment of my proposed method, I have used data from tide and atmospheric pressure models to simulate other forms of ice shelf motion. Further details of these data are given below.

6.4.1 Synthetic Aperture Radar

To map ice shelf flow I used Synthetic Aperture Radar data acquired during the second ice phase of the ERS-1 satellite (table 6.1). The SAR data were obtained

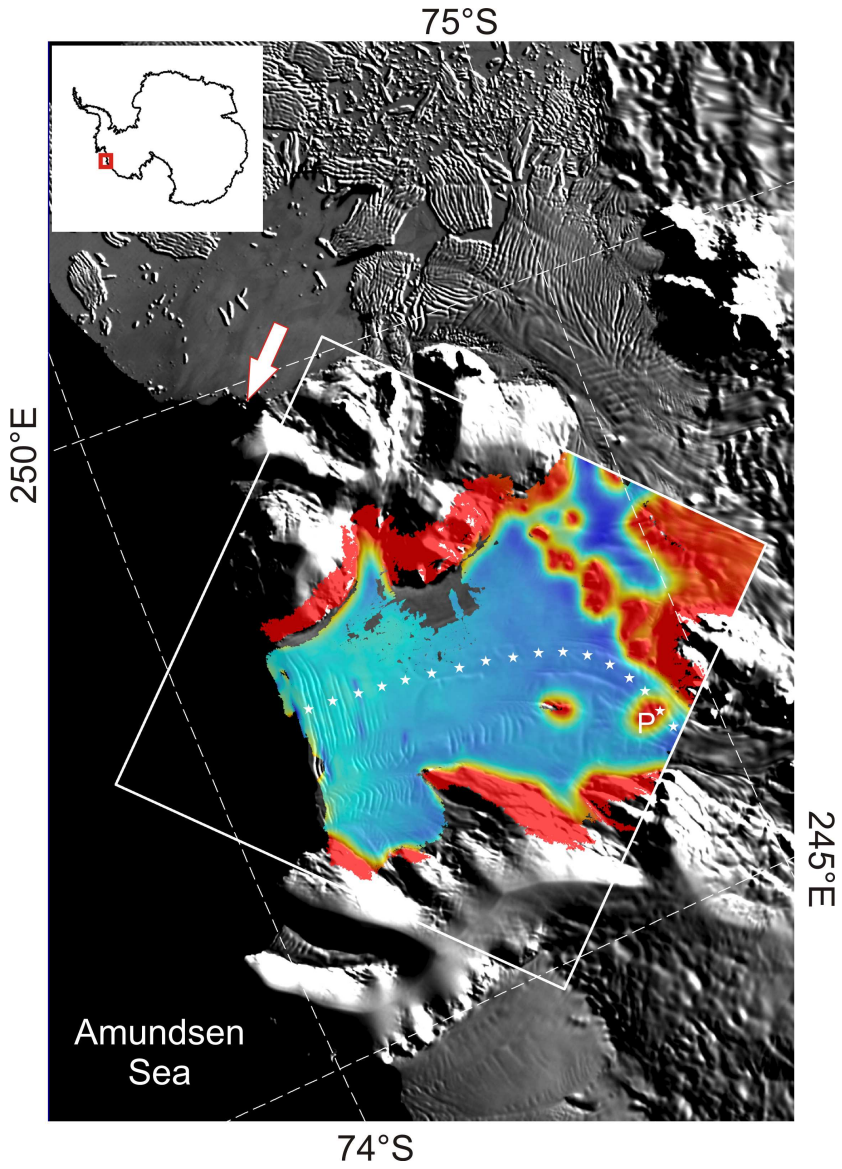

Figure 6.1: The Dotson Ice Shelf. Colour scale shows pattern of non-steady (tidal and IBE) displacement, derived from differential interferometric synthetic aperture radar; red indicates grounded ice, blue indicates floating ice. White box shows the spatial extent of the SAR data frames used in this study. White arrow indicates the satellite across-track direction. White stars indicate the location of the transect shown in figure 6.8 and *P* indicates the position of the pinning point identified in figure 6.8. The background image is taken from the Moderate Resolution Imaging Spectroradiometer (MODIS) mosaic of Antarctica (Haran *et al.*, 2006).

in raw format and processed using the Gamma software package (Werner *et al.*, 2000). I used a 5-km Antarctic-wide DEM (Bamber and Bindschadler, 1997) to remove the topographic component of the interferometric phase. To refine the ERS-1 interferometric geometry, I used point (60 m diameter) measurements of elevation from the Geoscience Laser Altimeter System (GLAS), on-board the Ice Climate and Elevation Satellite (ICESat) (Zwally, 2002). These data were acquired during the period 2003 - 2007. I used GLAS Level 1B elevation data (GLA06), which includes corrections for atmospheric propagation delays and the effect of solid Earth tides (Brenner *et al.*, 2003). Data points with no saturation elevation correction or large receiver gain values (greater than 50) were discarded. Saturation correction was added to the elevations. Geolocations in the GLA06 dataset were used without additional corrections.

Table 6.1: Synthetic aperture radar data used to form interferometric solutions. *e1* signifies ERS-1 satellite, $B_\perp$ specifies the perpendicular baseline of the SAR image pair.

Image pair (sensor-orbit-frame)	Acquisition date (reference image)	Temporal separation	Track	$B_\perp$	Usage	Interferogram identifier
e1-13153-5182 / e1-13196-5182	20 Jan 1994	3 days	39	17 m	InSAR + MAI	I1
e1-13239-5182 / e1-13282-5182	26 Jan 1994	3 days	39	-196 m	InSAR + MAI	I2
e1-13325-5182 / e1-13368-5182	1 Feb 1994	3 days	39	44 m	InSAR	I3

6.4.2 Tide Model

To model the tidal motion of the Dotson Ice Shelf, I used the Finite Element Solution model FES2004 (Lyard *et al.*, 2006), which performs well in the Amundsen Sea (chapter 5). FES2004 is a global tide model, with 1/8° resolution, which utilises sparse Antarctic tide gauge data (less than 10 records), together with TOPEX / Poseidon and ERS altimetry. The model was used for two purposes: (1) to generate tidal predictions coincident with the acquisition of the

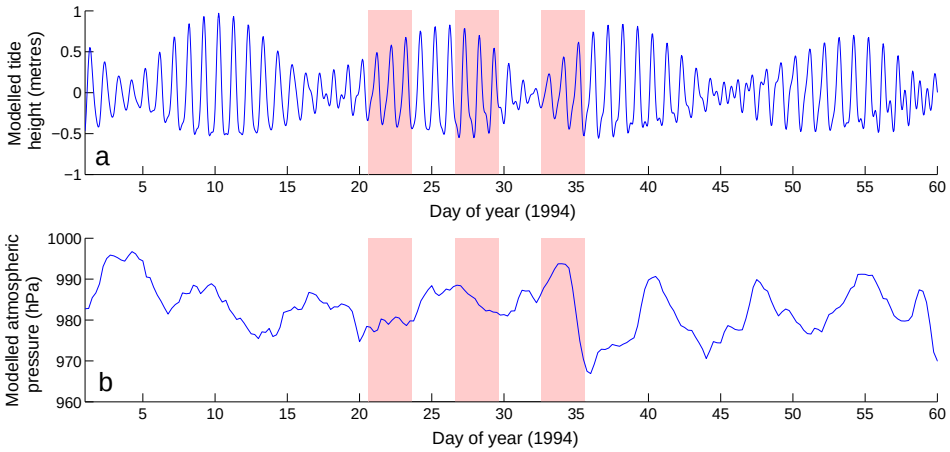

Figure 6.2: Modelled tide height (a) and surface level atmospheric pressure (b) at the Dotson Ice Shelf during the period of SAR data acquisition. Tide heights were estimated at 74.1°S, 247.5°E using the FES2004 tide model (Lyard *et al.*, 2006). Atmospheric pressure was estimated at 74°S, 247°E using the ERA-40 reanalysis (Uppala *et al.*, 2005). Shaded areas indicate periods over which interferograms were formed.

SAR data, and (2) to compute the distribution of tidal signals from a year-long, hourly resolution model run. Tide heights were obtained from the model just seaward of the ice front, at 74.1°S, 247.5°E, as I believe them to be more accurate at that location (chapter 5), than under the ice shelf itself where water column thicknesses are poorly known. The modelled tide height during the period of SAR data acquisition is shown in figure 6.2a.

6.4.3 Surface Level Atmospheric Pressure

In the absence of *in situ* meteorological data, model data from the European Centre for Medium-Range Weather Forecasts (ECMWF) ERA-40 reanalysis (Uppala *et al.*, 2005) were used to determine surface level atmospheric pressure changes at the Dotson Ice Shelf. Data at 74°S, 247°E were extracted from a 1° x 1° regularly spaced grid (derived from an N80 reduced Gaussian grid), which was acquired from the British Atmospheric Data Centre at 6-hourly temporal

resolution. These model data were used in two ways: (1) to generate predictions of surface level atmospheric pressure coincident with the acquisition of the SAR data (via a linear interpolation between the two closest 6-hourly model records), and (2) to compute the distribution of pressure signals from a year-long model record. The modelled atmospheric pressure during the period of SAR data acquisition is shown in figure 6.2b.

6.5 Methods

In this section I describe (1) the methods used to generate stacked displacement maps, (2) the use of model statistics to estimate the associated tidal and IBE error, and (3) the formation of comparison displacement maps using single model realisations to remove the predicted tidal and IBE signals from a single interferogram.

6.5.1 Conventional InSAR Stacking

The conventional interferometric synthetic aperture radar processing techniques used to map ice motion are well documented (Goldstein *et al.*, 1993; Joughin *et al.*, 1995, 1996a; Kwok and Fahnestock, 1996; Rignot, 1996) and so here I provide only a short overview of the methods used in this study. Interferograms were formed from co-registered SAR image pairs, with 3 days separating each acquisition (table 6.1). This acquisition configuration was chosen so as to (1) minimise temporal decorrelation by keeping the interferometric temporal baseline short, and (2) assess the method with respect to a simple and regular acquisition cycle. The sensitivity of my method to the temporal sampling provided by this acquisition cycle is examined in section 6.7.

For repeat-pass SAR observations of an ice shelf, the interferometric phase, φ, is due to a combination of terms:

$$\varphi = \varphi_{flat} + \varphi_{topo} + \varphi_{flow} + \varphi_{tide} + \varphi_{ibe} + \varphi_{noise} + \varphi_{ref} \tag{6.1}$$

This expression describes the spatial variation in phase, relative to a spatially-constant reference or phase offset (φ_{ref}). Phase variations across the image are caused by (1) the changing viewing angle across the ground track (φ_{flat}), (as described by the shape of Earth's ellipsoid), (2) surface topography (φ_{topo}), (3) surface displacement due to ice flow (φ_{flow}), tidal forcing (φ_{tide}) and the IBE (φ_{ibe}), and (4) noise in the received signal (φ_{noise}). The noise term encompasses both short-wavelength noise (for example from temporal decorrelation of the received signals) and mid-wavelength noise (such as atmospheric distortions of the interferometric phase).

Firstly, I used the interferometric geometry to simulate and remove the *flat Earth* signal. Where possible I used ICESat surface elevations over non-moving terrain to further refine my interferometric baseline estimate, and thus improve my model of this component of the signal. Where this was not possible, due to a lack of interferometric coherence over stationary regions, precise orbit information acquired from the Technical University of Delft was used. Loss of coherence over the period of interferogram acquisition was likely due to wind- or precipitation-driven changes to the near-surface snow pack.

Next, I unwrapped each interferogram. Ignoring the noise term (which I assess in the Errors section) and the constant phase offset (which I address at the end of this section), the remaining variation in the interferometric phase comprises contributions from (1) topography and (2) the line of sight component of the various modes of surface displacement:

$$\varphi = -\frac{4\pi}{\lambda}\left[\frac{z\ B_{\perp}}{r\sin\theta} + \sin\psi\ \Delta h_{flow} + \cos\psi\,(\Delta z_{tide} + \Delta z_{ibe})\right] \tag{6.2}$$

λ denotes the radar wavelength (5.7 cm for the ERS-1 satellite used in this study), $B_{\perp}$ denotes the component of the interferometric baseline perpendicular to the radar line of sight, z is the elevation of the target pixel above Earth's ellipsoid, r denotes the range from the satellite to the target pixel, θ is the radar look angle and ψ is the incidence angle of the radar beam relative to the normal to Earth's ellipsoid. Over the time period (Δt days) of the interferometric observation, Δh_{flow} denotes the horizontal ground range component of surface displacement due to ice flow, and Δz_{tide} and Δz_{ibe} denote the vertical displacement of the ice shelf in response to the tide and IBE, respectively. Stacking n interferograms yields a stacked phase:

$$\begin{aligned}\sum_{i=1}^{n}\varphi_i \;=\; -\frac{4\pi}{\lambda}\Bigg[&\frac{z}{r\sin\theta}\sum_{i=1}^{n}B_{\perp,i} + \sin\psi\ \sum_{i=1}^{n}\Delta h_{flow,i} \\ &+ \cos\psi\sum_{i=1}^{n}(\Delta z_{tide,i} + \Delta z_{ibe,i})\Bigg]\end{aligned} \tag{6.3}$$

To isolate the surface displacement component, elevations from a digital elevation model (Bamber and Bindschadler, 1997) were scaled by the effective perpendicular baseline of the stacked interferogram, and used to simulate and remove the topographic phase. Dividing the remaining stacked phase through by the total observation period of the stack yields an estimate of the ice flow velocity during that period (in m/day) subject to error from residual tidal and IBE signals:

$$\frac{\sum_{i=1}^{n}\varphi_i}{\sum_{i=1}^{n}\Delta t_i} = -\frac{4\pi}{\lambda}\left[\sin\psi\ \frac{\sum_{i=1}^{n}\Delta h_{flow,i}}{\sum_{i=1}^{n}\Delta t_i} + \cos\psi\ \frac{\sum_{i=1}^{n}(\Delta z_{tide,i}+\Delta z_{ibe,i})}{\sum_{i=1}^{n}\Delta t_i}\right] \quad (6.4)$$

This expression forms the basis of this work, whereby I use the stacked phase to estimate horizontal ice flow and model statistics to determine the magnitude of the associated tidal and IBE errors.

The method so far only determines relative displacement, i.e. how displacement varies across the image space. To determine absolute displacement values (by estimating the reference phase offset), I referenced my displacement map to a set of displacement estimates acquired where ice was grounded. As in chapter 5, grounded areas were identified by differencing two interferograms (figure 5.4). Reference displacements were then determined using the technique of coherence tracking (mapping surface motion based upon optimising coherence between patches of SAR image pairs (Derauw, 1999; Pattyn and Derauw, 2002; Strozzi *et al.*, 2002)) to map surface displacement in the satellite's line of sight direction. Following the same procedure described in section 5.6.1, InSAR velocities were adjusted so that the mean InSAR-derived velocity (over regions identified as being grounded) matched the equivalent velocity determined using coherence tracking.

6.5.2 Modelling Tide and IBE Error

My stacked InSAR velocity solution does not utilise model predictions of tide or IBE to isolate ice shelf flow. Instead I have aimed to minimise these signals by stacking displacement estimates. I now use the tide and IBE models to simulate the statistics of the residual tide and IBE signals in order to quantify the associated error in my stacked predictions of flow. I formed time series from both the FES2004 tide model and the ERA-40 atmospheric pressure reanalysis for the entirety of 1994, at hourly and 6-hourly intervals respectively. I converted atmospheric pressure changes into changes in ice shelf height (*IBE displacement*) using an inverse barometer approximation, namely the ratio determined empirically by Padman *et al.* (2003b) of -0.95 cm / hPa. Padman *et al.* (2003b) found little variation in estimates of this ratio derived from data collected at three widely-spaced and different-sized ice shelves, and so I assume this estimate to be valid at the Dotson Ice Shelf. Next, I calculated the tidal- and IBE-displacements that would occur in a stacked interferometric prediction acquired at every point along the timeseries. I converted these modelled vertical displacements into annual velocities in the satellite's across-track direction and so determined the distribution of velocity errors, arising from residual tidal and IBE signals, that could be present in my stacked prediction of flow.

6.5.3 Isolating Flow Displacement Using Model Predictions

To assess my stacked velocity solution I used the same InSAR data (table 6.1) to form alternative displacement maps, using the standard technique of removing the tidal signal from each individual interferogram, based upon the coincident tide model predictions (Rignot and Jacobs, 2002; Joughin *et al.*, 2003; Rignot *et al.*, 2004; Vieli *et al.*, 2006). I have extended this method to additionally remove

the modelled IBE component of ice shelf motion. To isolate flow, I followed the interferometric method described above to convert individual interferograms into maps of absolute across-track displacement. Next, I used a *double difference* technique (Hartl *et al.*, 1994; Rignot, 1996, 2002a) to determine the pattern of non-steady (tide and IBE) displacement of the Dotson Ice Shelf (figure 6.1). To simulate the tidal and IBE signals occurring within each interferogram, I scaled the double difference solution so that the mean displacement across the freely floating portion of the ice shelf matched that of the combined modelled tide and IBE displacement. This prediction was subtracted from each conventional InSAR displacement map, in order to produce multiple predictions of ice flow.

6.5.4 Multiple Aperture InSAR Stacking

Conventional InSAR only measures one dimension of the displacement field; along the satellite's line of sight. To determine 2-d vectors I estimated displacement along the satellite track using Multiple Aperture InSAR (MAI) processing (Bechor and Zebker, 2006; Jung *et al.*, 2009; Gourmelen *et al.*, 2011). Previous work has shown that MAI offers improvements in estimates of along-track displacement as compared to tracking methods, both for solid Earth (Bechor and Zebker, 2006) and glaciological (Gourmelen *et al.*, 2011) applications. MAI processing splits the antenna beam to form two sub-aperture Single-Look Complex (SLC) images, one forward-looking and one backward-looking, from each conventional SAR image. Then, from a pair of SAR images, the forward looking SLC's and the backward looking SLC's are each combined to form two interferograms which are sensitive to displacement in both the azimuth and range directions. Differencing the interferometric phase of these forward-looking and backward-looking interferograms cancels the common range component of the interferometric phase and isolates a phase difference that is proportional to the along-track component of

the displacement field. Because MAI measures the difference between the interferometric phase as observed from two different viewing angles, rather than the interferometric phase itself (as measured by conventional InSAR), the MAI phase measurement is less sensitive to surface motion. Specifically, from the interferometric geometry Bechor and Zebker (2006) show that the MAI phase, φ_{mai}, is related to the along-track displacement, x, by the expression:

$$\varphi_{mai} \approx -\frac{2\pi}{l}\, x \tag{6.5}$$

where l denotes the antenna length (10 m for the ERS-1 satellite). Consequently, a 2π phase change corresponds to a 10 metre change in displacement for MAI (versus 2.8 cm for InSAR), meaning that MAI phase gradients are lower than InSAR and the phase over moving and stationary areas could be linked. These stationary areas provided an absolute reference for my displacement estimates. Although MAI is insensitive to vertical ice shelf motion, I still stack MAI interferograms, so as to amplify the steady ice flow signal, relative to temporally uncorrelated noise sources. Finally I combine the along-track velocity component from MAI with the across-track velocity component from conventional InSAR, in order to determine a map of velocity magnitude.

6.6 Results

6.6.1 Stacked Velocity Map

I used the stacked multiple aperture and conventional InSAR solutions to determine the along-track (figure 6.3a) and across-track (figure 6.3b) components, respectively, of the flow velocity vectors. I then combined these components to

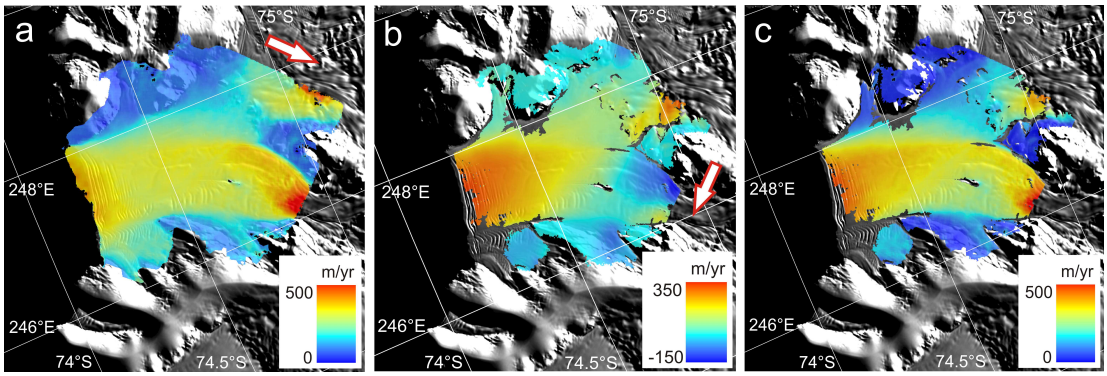

Figure 6.3: Flow velocity of the Dotson Ice Shelf. a. Along-track velocity component derived from stacked MAI, white arrow indicates the satellite along-track direction; b. Across-track velocity component derived from stacked InSAR, white arrow indicates the satellite across-track direction; c. Velocity magnitude from combined azimuth (a) and range (b) components. The background image is taken from the MODIS mosaic of Antarctica (Haran *et al.*, 2006).

give a map of the magnitude of the 2-d flow velocity vectors (figure 6.3c). I assumed ice flow to be in the horizontal plane, i.e. that the vertical component of flow was negligible. My solution shows that the Dotson Ice Shelf is primarily fed by fast flowing ice originating from the Smith and Kohler Glaciers. Close to the grounding line, where the ice funnels through a narrow gap, velocities exceed 500 m/yr. Further downstream, on the freely-floating portion of the ice shelf, speeds drop to $\sim$ 320 m/yr, before increasing again to $\sim$ 500 m/yr close to the calving front.

6.6.2 Error Assessment

To assess the viability of my stacking method, I considered the error associated with my stacked velocity solution. I define the error, ε, associated with interferometric estimates of horizontal ice shelf flow as follows:

$$\varepsilon^2 = \varepsilon^2_{tide} + \varepsilon^2_{ibe} + \varepsilon^2_{topo} + \varepsilon^2_{base} + \varepsilon^2_{atmos} + \varepsilon^2_{coh} + \varepsilon^2_{ref} + \varepsilon^2_{unw} \qquad (6.6)$$

The error components refer, in left to right order, to errors from residual tidal displacement, residual IBE displacement, unmodelled topography, unmodelled baseline effects, atmospheric phase distortions, loss of coherence, error in determining an absolute reference and error in the phase unwrapping process. To simplify this assessment, I assumed that all errors were independent. This provides a close approximation of the true error since the dominant error components (namely tide and IBE, as outlined in this section) are independent. The extent to which these error sources affect the across- and along-track components of my displacement field varies as a consequence of the different techniques used. I address the error associated with each component in turn.

Conventional InSAR

Firstly I considered the effect of each error component (equation 6.6) on my conventional InSAR estimates of across-track displacement. To assess the tide and IBE errors (ε_{tide} and ε_{ibe}) I used one year's worth of model data to estimate the distribution of these signals occurring over the timescales of the interferometric acquisitions, using the procedure outlined in chapter 5. I then converted these estimates of vertical displacement into equivalent errors in the across-track component of the velocity solution (figure 6.4). In each case I computed the signals corresponding to (1) a single interferogram (i.e. the 3-day difference in tide height), (2) two stacked interferograms, and (3) three stacked interferograms. Both the tide and IBE contributions to the velocity error tend to diminish in size as the interferometric predictions are stacked, primarily as a consequence of the longer observation period over which displacement is measured. The distributions of the stacked tidal and IBE signals are roughly normal and centred close to zero. In contrast, the twin-peaked distribution of the single interferogram tidal displacement indicates that, in a single interferogram, a much larger signal is likely to be present, and demonstrates the value of stacking to

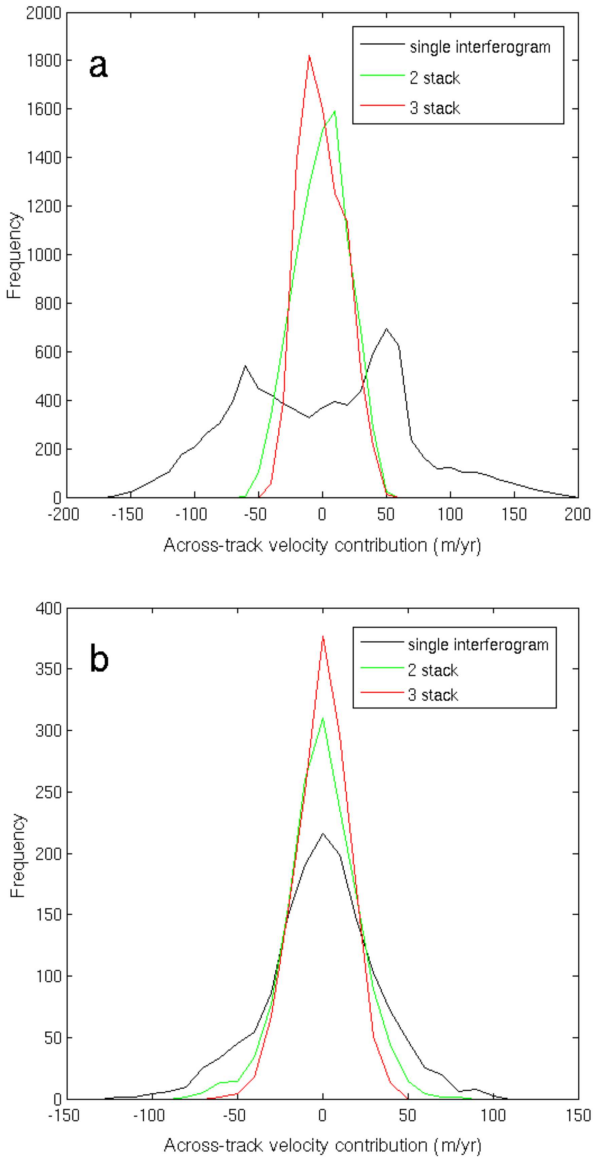

Figure 6.4: Modelled distribution of the (a) tidal and (b) IBE contributions to conventional InSAR estimates of across-track flow velocity at the Dotson Ice Shelf. Each panel shows the expected distribution of across-track velocity errors arising from the tidal and IBE motion of the ice shelf within a single interferogram (3 day separation, as shown in figure 5.10b), and for 2- and 3- stacked interferograms. Tide was computed from hourly realisations of the FES2004 tide model, and the IBE from 6-hourly realisations of the ERA-40 reanalysis of surface level atmospheric pressure, converted into changes in ice shelf height using the empirical relationship determined by Padman *et al.* (2003b). Both models were run for the entirety of 1994, and the resulting vertical displacements were converted into equivalent annual velocities in the satellite's across-track direction.

Figure 6.5: Stationary areas (bounded by white lines) used to estimate the error in my tracking displacement map, ε_{ref}.

reduce the tidal contribution. The distribution of the single interferogram tidal displacements (black line in figure 6.4a) is asymmetric, with the right-hand peak (positive velocity contribution) being larger than the left hand peak (negative velocity contribution). This is likely to be a consequence of the positively skewed distribution of modelled tidal height (figure 5.10a). I do not believe it to be an artifact of the FES model as all three models considered in chapter 5 are consistent in predicting such an effect. To determine the contribution of tide and IBE error to the 3-stack velocity estimate, I combined the standard deviations of the modelled tidal (20 cm over a 9-day period) and IBE (18 cm over a 9-day period) signals. This yielded a total error due to residual vertical motion of 27 cm, which equates to an error of 22 m/yr in the across-track component of the stacked velocity solution.

To determine an absolute reference for my InSAR displacements, I matched the mean InSAR and mean tracking range displacements over grounded ice.

Consequently, any bias in the tracking displacements is transferred to my InSAR solution. I estimated this referencing error, ε_{ref}, from the displacement values of pixels that were located on stationary areas (figure 6.5). Over the 3-day period of my tracking measurements, the mean displacement of these points was 6 cm, equivalent to a bias of 7 m/yr in my velocity solution.

The effect of the remaining error terms upon my velocity solution is likely to be small in comparison to the aforementioned errors. Because of the minimal topographic relief in my study area, relative DEM errors are small (of order 5 m (Bamber and Gomez-Dans, 2005)) as compared to the 70 metre altitude of ambiguity of my stacked interferogram (i.e. the elevation change equivalent to one complete cycle of the interferometric phase, which is a function of the effective baseline of my stacked interferogram). This topographic error, ε_{topo}, equates to a 0.9 cm across-track displacement error in my 9-day stacked interferogram, equivalent to a 0.4 m/yr error in my velocity estimate.

As a measure of the displacement error arising from loss of coherence, ε_{coh}, I calculated the errors associated with the average coherence of each interferogram (Rodriguez and Martin, 1992). The resulting displacement error in my 9-day stacked interferogram is 0.4 cm, equivalent to an error in the across-track component of my velocity solution of less than 0.2 m/yr. Atmospheric distortions of the interferometric phase, ε_{atmos}, occur because of spatial and temporal inhomogeneity in the troposphere and ionosphere. To quantify the tropospheric component, I followed the procedure outlined in chapter 5. Based upon the length- and time-scales appropriate to this study and the parametrisation determined by Emardson *et al.* (2003), I estimated the error arising from the tropospheric variability to be at most 4.1 cm in my 9-day stacked interferogram, equivalent to a 1.7 m/yr error in my velocity solution. I neglected ionospheric errors, (Gray *et al.*, 2000) as these tend to manifest themselves as distinctive features, and I do not see any evidence of these features in my dataset. I have aimed to minimise any

Table 6.2: Summary of terms contributing to displacement error in the three-stack (9-day) InSAR estimate of across-track displacement. Referencing error calculated from tracking displacements determined over a 3-day period.

Error term	**Across-track error (cm)**	**Contribution to across-track velocity (m/yr)**
Tide	41.0	16.6
Inverse Barometer Effect	36.9	15.0
Topography	0.9	0.4
Referencing	5.9	7.2
Atmosphere	4.1	1.7
Coherence	0.4	0.2
Total	55.6	23.5

unmodelled baseline effects by, where possible, refining my baseline estimates and checking for residual long-wavelength phase gradients over stationary areas. It is possible that some small residual baseline error may exist in my velocity solution, which I have not accounted for in my error budget. The process of stacking will, however, further reduce any such effect. During the phase unwrapping process I unwrapped along a path that gave no visible unwrapping errors and so I assume no unwrapping errors in my velocity solution. The contributions from errors associated with my across-track displacement estimates are summarised in table 6.2. Of these, the errors arising from atmospheric distortions and loss of coherence are specific to the C-band frequency of the ERS SAR and will vary for sensors operating at alternative frequencies. Combining all across-track error sources yields a 23.5 m/yr error in this component of my velocity solution. This error component is dominated by the errors from tidal and IBE effects.

Multiple Aperture InSAR

I now consider the error contributions (equation 6.6) to my MAI estimates of along-track displacement. As part of MAI processing the forward- and backward-looking interferometric phases are differenced, and so errors common to both viewing angles will cancel. These include topographic and tropospheric contributions (Bechor and Zebker, 2006), plus any signal associated with the vertical motion of the ice shelf. Long wavelength phase trends over stationary areas were used to estimate residual phase ramps resulting from unmodelled baseline effects (Jung *et al.*, 2009) and these were removed. A visual inspection again showed no evidence of ionosphere-related errors (Gray *et al.*, 2000). Because MAI is less sensitive to surface displacement than conventional InSAR, fringe rates are lower and so I do not anticipate unwrapping errors occurring.

I estimated the remaining MAI error terms, that of loss of coherence, ε_{coh}, and

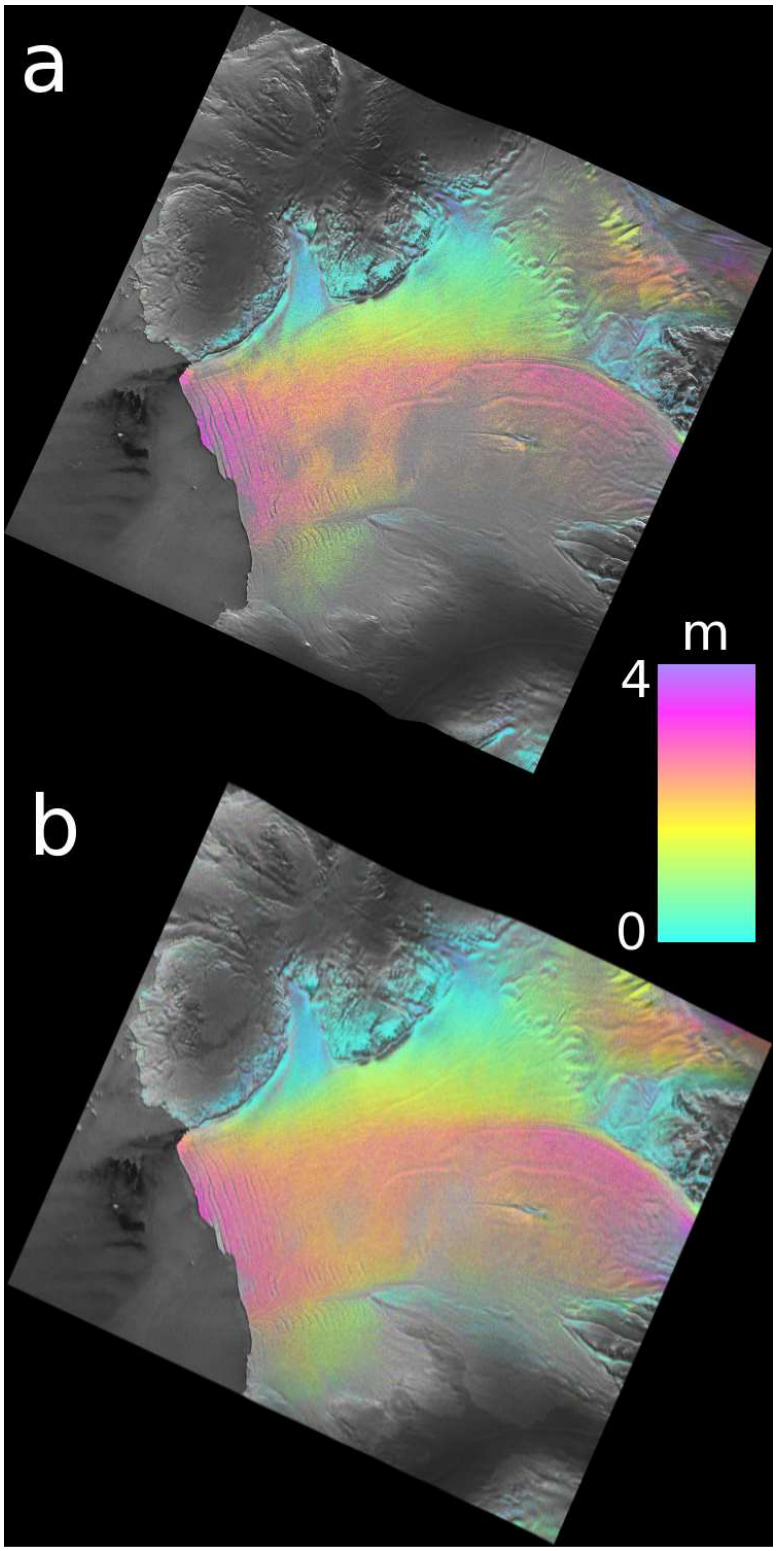

Figure 6.6: Comparison of along-track surface displacement estimates determined using (a) coherence tracking and (b) MAI. No post-processing filtering has been applied to either image. Both estimates were made from a pair of SAR images acquired on the 20th and 23rd January 1994.

of satisfactorily referencing displacements to stationary areas, ε_{ref}, from the displacement values of pixels that were located on non-moving ground. The displacements of these points exhibit an approximately normal distribution, with a root mean square error of 34 cm for my 6-day stacked pair, equivalent to an error of 21 m/yr in the along-track component of my velocity field. To assess the MAI technique, I compared my MAI estimate of azimuth displacement to an equivalent estimate determined using coherence tracking (figure 6.6). As compared to coherence tracking, MAI yields both better spatial coverage and a $\sim$ 30 % reduction in the error, as determined over stationary regions (figure 6.5).

I have determined that that the errors associated with the across- and along-track components of my flow velocity solution are roughly equal (23 m/yr and 21 m/yr respectively); a consequence of (1) the improved along-track accuracy offered by stacking MAI images, as compared to conventional tracking methods, and (2) the effect of residual vertical motion upon InSAR estimates of across-track displacement. As such, I have demonstrated that 2-d ice shelf velocity can be estimated by combining MAI and InSAR data acquired from a single viewing direction, with comparable errors pertaining to both of the velocity vector components.

Velocity Magnitude

Commonly in studies of ice flow, it is estimates of velocity magnitude (figure 6.3c) that are of most interest. The simplest approach to determining the error associated with the velocity magnitude is to sum in quadrature the along-track and across-track error components, which yields an error of 31 m/yr in my velocity magnitude solution. This approach assumes independence of along-track and across-track errors. The MAI and InSAR observations are both derived from

the same SAR data, and so the coherence and referencing errors affecting both velocity components will not necessarily be independent. However, because these errors form only a tiny fraction of the total InSAR error (table 6.2), I expect any increase in the total error due to the non-independence of these components to be small. The extent to which the error vector (defined by the along- and across-track error components) affects the velocity magnitude will vary according to the orientation and magnitude of the velocity vector relative to the error vector. For a 2-d flow velocity vector, $\mathbf{v}$, with an associated error vector, $\mathbf{e}$, the change (i.e. error) in the velocity magnitude, $\varepsilon_{|\mathbf{v}|}$, resulting from the vector addition of $\mathbf{e}$ to $\mathbf{v}$, can be described using the cosine rule:

$$\varepsilon_{|\mathbf{v}|} = |\mathbf{v}+\mathbf{e}| - |\mathbf{v}| = \sqrt{|\mathbf{v}|^2 + |\mathbf{e}|^2 - 2|\mathbf{v}||\mathbf{e}|\cos\theta} \; - \; |\mathbf{v}| \tag{6.7}$$

If the vectors $\mathbf{v}$ and $\mathbf{e}$ are placed head to tail, then θ is the inner angle formed where they meet, such that when $\theta = 180°$ the vectors $\mathbf{v}$ and $\mathbf{e}$ point in the same direction, and $\theta = 0°$ indicates that $\mathbf{v}$ and $\mathbf{e}$ are orientated in opposite directions. To illustrate the variation in velocity magnitude error, I have used this expression (equation 6.7) to plot the error in velocity magnitude, $\varepsilon_{|\mathbf{v}|}$, as a function of the size and orientation of the velocity vector relative to the satellite heading, given a fixed error vector (figure 6.7). I have orientated the error vector in the direction determined from the ratio of my along-track and across-track error components (49° from the along-track direction). The error in velocity magnitude peaks at 31 m/yr when the velocity and error vectors are orientated in the same, or exactly opposite, direction. The quadrature sum of my along- and across-track error components therefore represents an upper bound upon the error associated with my velocity magnitude estimate. In more favourable cases the error in velocity magnitude will be significantly smaller, tending to zero when the velocity and

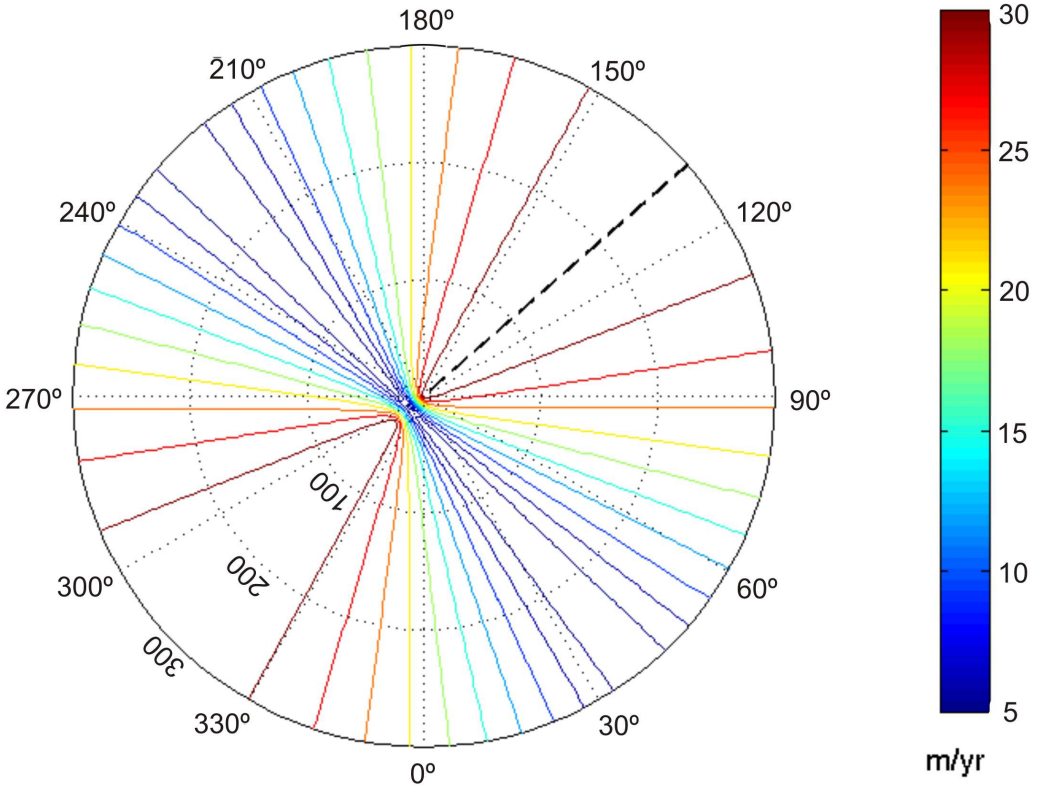

Figure 6.7: Polar contour plot of the velocity magnitude error, as a function of the size and orientation of the flow velocity vector relative to the satellite track. The plot angle indicates the orientation of the flow vector, with 0° - 180° being the along-track direction, and 90° - 270° being the across-track direction. The plot radius indicates the flow speed, plotted here from 0 m/yr to 300 m/yr. The coloured contours indicate the magnitude of flow error, and the thick black dashed line indicates the orientation of the error vector, which is determined from the relative contributions of the errors in along- and across-track directions (see *Velocity Magnitude Error Assessment* section in text for more details). Flow is assumed to be in the horizontal plane. The velocity magnitude error is greatest when flow is orientated in line, or directly opposing the error vector. Velocity magnitude errors decrease to 0 m/yr when these vectors are close to orthogonal.

error vectors are close to orthogonal. Consequently, a simple quadrature sum of the error components will often overestimate the true velocity magnitude error.

6.7 Discussion

In this section I begin by comparing my stacking method to conventional InSAR methods for determining ice shelf flow. With a view to upcoming satellite missions, I then assess the wider applicability of the method described here. I investigate (1) the sensitivity of the tidal and IBE signals to alternative temporal sampling regimes offered by other satellites and (2) the potential for larger image stacks to further reduce these errors.

6.7.1 Comparison of Velocity Predictions

Residual tidal and IBE displacement contribute the greatest error to my across-track velocity solution. To assess the impact of these two error sources upon my across-track velocity estimates, I compared my stacked map of across-track displacement to solutions obtained by a commonly-used method (e.g. Rignot and Jacobs (2002); Joughin *et al.* (2003); Rignot *et al.* (2004); Vieli *et al.* (2006)), whereby model predictions are used to remove the tidal and IBE signals. I formed three velocity estimates by removing modelled tidal and IBE signals from each of the individual interferograms used in my stacking solution. Figure 6.8 shows a comparison of these solutions extracted from a transect along the primary line of ice flow (transect location shown in figure 6.1). I have plotted only the across-track component of velocity, as only this component is sensitive to vertical motion. Where ice is grounded (indicated by P in figures 6.1 and 6.8) all velocity estimates converge. Because the InSAR solutions are tied down using all grounded

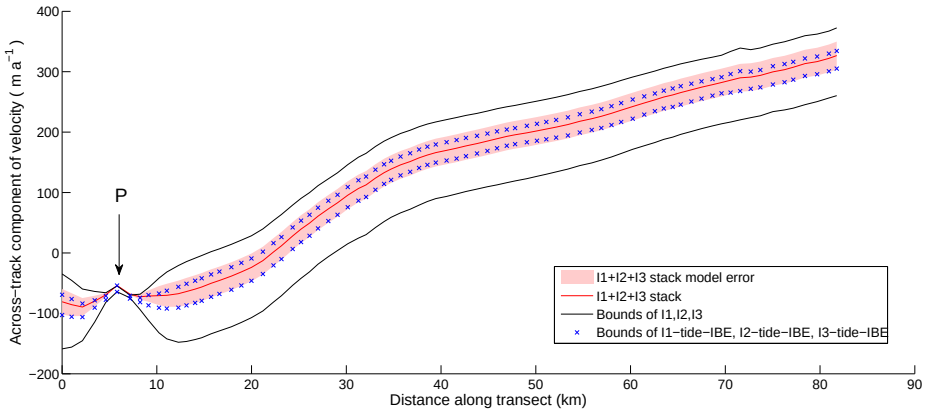

Figure 6.8: Across-track component of the Dotson Ice shelf flow speed, transect location marked in figure 6.1. *P* indicates a pinning point where the ice is grounded. Black lines indicate the maximum and minimum displacements of 3 interferograms (*I1*, *I2* and *I3*, see table 6.1) which include tidal and IBE signals. Crosses indicate the range of these interferometric predictions of displacement, after modelled tide and IBE have been removed. Red line indicates stacked prediction of displacement, with no use of tide or IBE models. Red shading indicates uncertainty of stacked prediction, determined from tide and IBE model statistics.

locations (as shown by red colours in figure 6.1), and not just at the point P, this convergence confirms that errors arising from unmodelled topography and baseline effects are small, and that flow remains steady over the period of data acquisition. Where the ice is freely floating (greater than $\sim$ 10 km along the transect), each velocity estimate exhibits a roughly constant offset, which I interpret as resulting from vertical displacement due to the combined effect of the tide and IBE. The fact that this offset displays little spatial variation over the floating ice shelf indicates that my velocity estimates are not greatly affected by spatial variability in the tidal and IBE signals over the length scales of the ice shelf. This is consistent with the modelled IBE's spatial variability over the ice shelf at the times of data acquisition, which produces on average 3 m/yr variation in the velocity signal. I do not perform an equivalent assessment for the tidal signal because the accuracy of the FES model under the ice shelf is uncertain (chapter 5). Assuming that these spatial patterns are uncorrelated in time, then stacking will further diminish the effects of any such spatial variability.

I compared InSAR velocity predictions before and after modelled tide and IBE corrections. Using model predictions to remove the tidal and IBE signals from each of the interferograms decreases the variability between each of the interferograms (blue crosses in figure 6.8), as compared to the original interferograms (black lines in figure 6.8), and indicates that models successfully account for some of the tidal and IBE motion. However, some variation still exists, likely as a result of residual unmodelled vertical ice shelf motion. This variation is indicative of the accuracy limits of the model predictions used to remove these signals. As a measure of this variation, I calculated the standard deviation of these individual model-dependent estimates of flow at each point along the transect. The mean standard deviation along this transect (floating ice only) was 17 m/yr, which is in reasonable agreement with the estimate of single-difference model accuracy from chapter 5 of 22 m/yr.

In contrast to these model-dependent flow estimates, my stacked velocity solution does not rely upon model predictions and consequently is not limited by the accuracy of these estimates. By utilising stacking, I have maintained independence from model data, whilst achieving a velocity prediction that falls within the range of model-dependent solutions (i.e., the region bounded by the blue crosses in figure 6.8). This gives us confidence that, for the data used here, stacking only a small number of interferograms (three in this case) provides a reasonable, and model-independent, estimate of flow velocity. This study is, however, only based upon a relatively limited set of SAR data and I have no independent means of determining the actual tidal and IBE displacement. Consequently, I cannot discount the possibility that, fortuitously, the tidal and IBE signals happened to cancel in my particular stacked prediction of flow, and in other instances the stacked solution may be more greatly affected by these signals. My error model does, however, account for this uncertainty, because I have modelled the distribution of all potential tide and IBE errors. This provides a measure of the possible

variation in my velocity solution, depending upon the particular tidal and IBE realisation present in my data. The fact that I have only stacked relatively few interferograms is reflected in the spread of this distribution. I assess the magnitude of this error and the implications for my stacking method in the following section.

6.7.2 Comparison of Methods for Error Estimation

When ice shelf flow velocities are determined from a single interferogram, together with a single model realisation of tide and IBE displacement, then different image pairs produce varying velocity solutions (as shown by blue crosses in figure 6.8). This variation results from inaccuracies in model predictions of tidal and IBE displacements. Accordingly, the error assigned to such a velocity solution must account for the effect of these model inaccuracies. A direct model validation is difficult in remote areas such as the Amundsen Sea, where I know of only one attempt (chapter 5) to assess the accuracy with which tide models can specifically reproduce the interferometric tidal displacement. Rignot (2002a) assessed a model's ability to simulate the difference between two displacements, but not the displacement itself. Whilst the work described in chapter 5 produces the first such accuracy estimate in the Amundsen Sea, imprecision inherent in the method used limited the estimate of the associated across-track velocity error to 22 ± 17 m/yr. Consequently, the error associated with flow velocities determined from a single interferogram (blue crosses in figure 6.8) is not well constrained.

In contrast, because velocities derived using the stacking method are independent of model predictions, I avoid the problem of quantifying the associated model accuracy. In my method I do not use models to simulate and remove specific tidal and IBE displacements, but only to estimate the statistics of these signals, in order to assess the distribution of possible errors within my stacked velocity prediction.

As such, I only require that the statistics of the model are sufficiently accurate; in other words, that the model simulates lifelike behaviour. A previous study (Shepherd and Peacock, 2003) found that tide model error was dominated by inaccuracies in predicting the tidal phase. Consequently, model statistics should adequately reflect the set of all tidal amplitudes, even if they do not correctly predict the timing at which a given amplitude occurs. The combined tidal and IBE error determined from model statistics for the stacked velocity solution is plotted in figure 6.8 (red shading). This assessment of error is consistent with the variability of solutions that utilise model predictions to remove the tidal and IBE signals, as would be expected given that both the error associated with my stacked solution and the model error in predicting tidal and IBE displacement (chapter 5) are of the order of 20 m/yr. By stacking only three interferograms, I have achieved an accuracy comparable to that provided by current tide models. Future satellite missions, offering the prospect of forming larger image stacks, have the potential to further reduce this stacked velocity error.

6.7.3 Generalisation of Stacking Method

The results of this study indicate that for the dataset considered here, stacking provides an effective method for reducing tidal and IBE errors, without using model predictions to remove these signals. In this section I assess the wider applicability of this method by considering alternative sampling regimes, resulting from satellites with different orbit configurations. I also assess the potential for a further reduction of errors by stacking a larger number of images.

The motivation for this assessment is provided by the prospect of new data, from satellites which will make regular, short-repeat acquisitions that are well-suited to this stacking method. In the first half of 2011, the ERS-2 satellite was placed into a 3-day acquisition cycle, thus providing a new set of data with

the potential to create larger image stacks. Looking to the future, the planned launch of the Sentinel-1 and Radarsat Constellation satellites offers the prospect of regular SAR acquisitions, albeit with different temporal sampling regimes, and with it the potential to create larger image stacks and further reduce tidal and IBE errors.

Sensitivity of Tide and IBE to Temporal Sampling

This work has focused on a specific acquisition configuration; a series of interferograms formed from a regular 3-day acquisition cycle, such that the reference images of each interferogram are separated by 6 days (table 6.1). Using this configuration I have modelled the distribution of tidal and IBE signals which could occur within my stacked interferogram. If, however, the tidal and IBE signals exhibit temporal structure, then the magnitude of these signals will vary according to the temporal sampling offered by the satellite. To asses this variability, I modelled the tidal and IBE signals for a range of sampling configurations. For each configuration, I modelled the signals in both a stack of 3 and a stack of 5 interferograms to investigate how the sensitivity was affected by the number of interferograms stacked. I varied both the temporal baseline of the interferogram (i.e. the separation between the two SAR images forming each interferogram) and the interferogram separation (i.e. the separation between each master image in the interferogram stack). Repeating the procedure described in the Methods section of this chapter, tide and IBE model statistics were calculated for each sampling regime. For every distribution, the standard deviation of the modelled signal associated with the image stack was converted into an equivalent error in the annual flow velocity. Results are shown in figure 6.9.

In both stacks, the tidal and IBE signals tend to decrease as the temporal baseline increases. This is because of the decreasing influence of the tide and IBE, relative

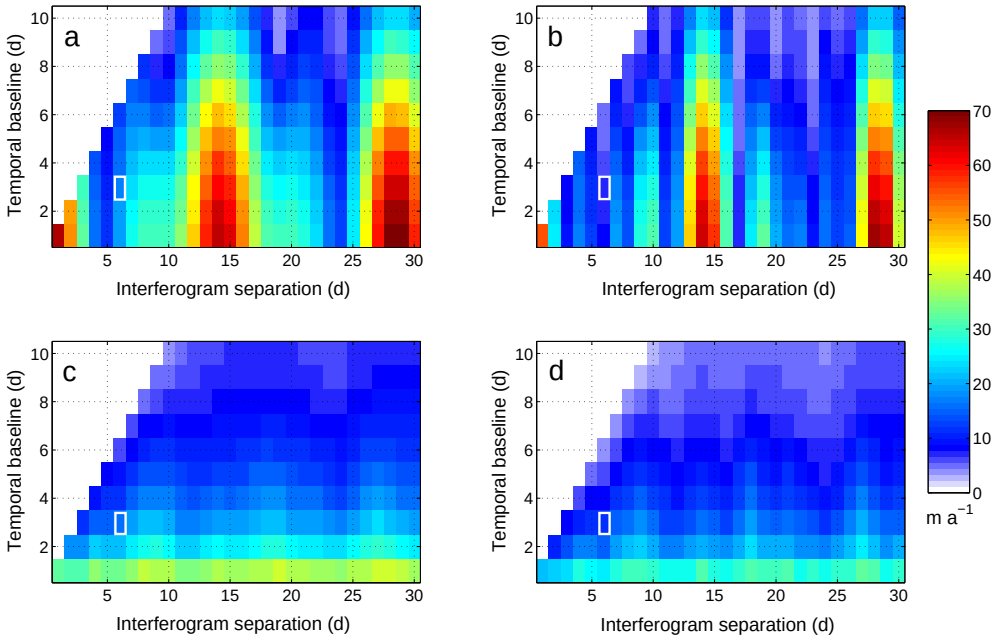

Figure 6.9: Modelled sensitivity of tidal (panels *a* and *b*) and IBE (panels *c* and *d*) signals to the interferometric temporal sampling regime. Results are plotted for stacks of 3 interferograms (panels *a* and *c*) and 5 interferograms (panels *b* and *d*). Each plot shows the standard deviation of the modelled velocity error arising from the tide or IBE. Each standard deviation is calculated from the set of all modelled signals, obtained from a year-long model run, such as those shown in figure 6.4. The temporal baseline specifies the time period separating the pair of SAR images used to form each interferogram; the interferogram separation indicates the elapsed time between the master images of consecutive interferograms in the stack. The white boxes mark the sampling regime used in this study. Interferogram separations shorter than the temporal baseline have been set to zero.

to the steady flow signal, as the observation period increases. With respect to the period of separation between interferograms in the stack, the tidal signal displays a clear structure (figures 6.9a and 6.9b), and exhibits considerable sensitivity to the time separation of interferograms. In both the stack of 3 interferograms (figure 6.9a) and the stack of 5 interferograms (figure 6.9b) the tidal signal peaks at a contribution of $\sim$ 70 m/yr when interferograms are separated by a multiple of $\sim$ 14 days. This is a consequence of the strong fortnightly beating of the *Mf* tidal constituent at my study site, which is clearly evident in the modelled tidal record (figure 6.2a), and which dominates the long period (greater than diurnal) tidal signal.

The sensitivity of the tidal signal to the temporal sampling regime implies that the repeat time of the satellite will influence the effectiveness of the stacking technique. Worst case errors occur where the sampling frequency matches that of the dominant long-period tidal constituent. In this case stacking is unlikely to achieve the accuracy offered by a method that uses model predictions to remove the tidal and IBE signals. For the majority of sampling configurations, however, my analysis (figure 6.9) indicates that stacking will be an effective technique. The temporal sampling provided by the ERS acquisitions used in this study (indicated by white boxes in figure 6.9) proves favourable in producing a relatively small tidal signal. Furthermore, this analysis provides an indication of the effectiveness of stacking given the 6 day revisit time planned for Sentinel-1. For a continuous stack of 6-day interferograms (where the slave image of the preceding interferogram becomes the master image of the next interferogram), this analysis suggests that stacking five interferograms, and hence observing a full month-long period, would reduce the tidal error contribution to $\sim$ 5 m/yr.

In contrast to the tidal signal, the period of separation between the stacked interferograms has little effect upon the magnitude of the IBE signal (figures 6.9c and 6.9d). This is a consequence of the lack of temporal structure in the

atmospheric pressure record. Comparing the 3-stack and the 5-stack scenarios, both the tidal and IBE error contributions tend to be lower in the 5-stack, as a consequence of the longer period of observation. In the case of the tidal signal, the temporal structure is less well defined in the 5-stack; again a consequence of the longer total period of observation, which captures more completely the full tidal cycle.

Benefits Offered by a Larger Stack

In this study the data archive has limited us to stacking only three regularly spaced interferograms. The ERS-2 2011 3-day acquisition phase and the planned Sentinel-1 and Radarsat Constellation satellites offer the prospect of regular SAR acquisitions and with it the potential to stack a greater number of interferograms. To investigate the possible benefits offered by stacking a greater number of images I used the tide and atmospheric models to estimate the magnitude of these signals in larger stacks (again following the procedure described in the Methods section). In particular, I considered three sampling scenarios; (1) the configuration used in this study (3-day interferograms, 6 days between each reference image in the interferogram stack), (2) a continuous series of observations from 3-day data (i.e. the slave image of the previous interferogram becomes the master image of the following interferogram), and (3) as in (2) but with 6-day repeat data (as planned for Sentinel-1). Results for up to 10 stacked interferograms are shown in figure 6.10. In all three sampling scenarios, the tidal and IBE errors decrease as a larger stack is formed; a consequence of the longer period of observation. The greatest benefit is gained with the first few interferograms that are stacked, particularly in the cases where interferograms are separated by 6 days, when simply stacking two interferograms reduces the tidal signal by two thirds. As more interferograms are stacked, there is a general trend towards diminishing improvements, although the availability of a larger number of interferograms has the benefit of providing

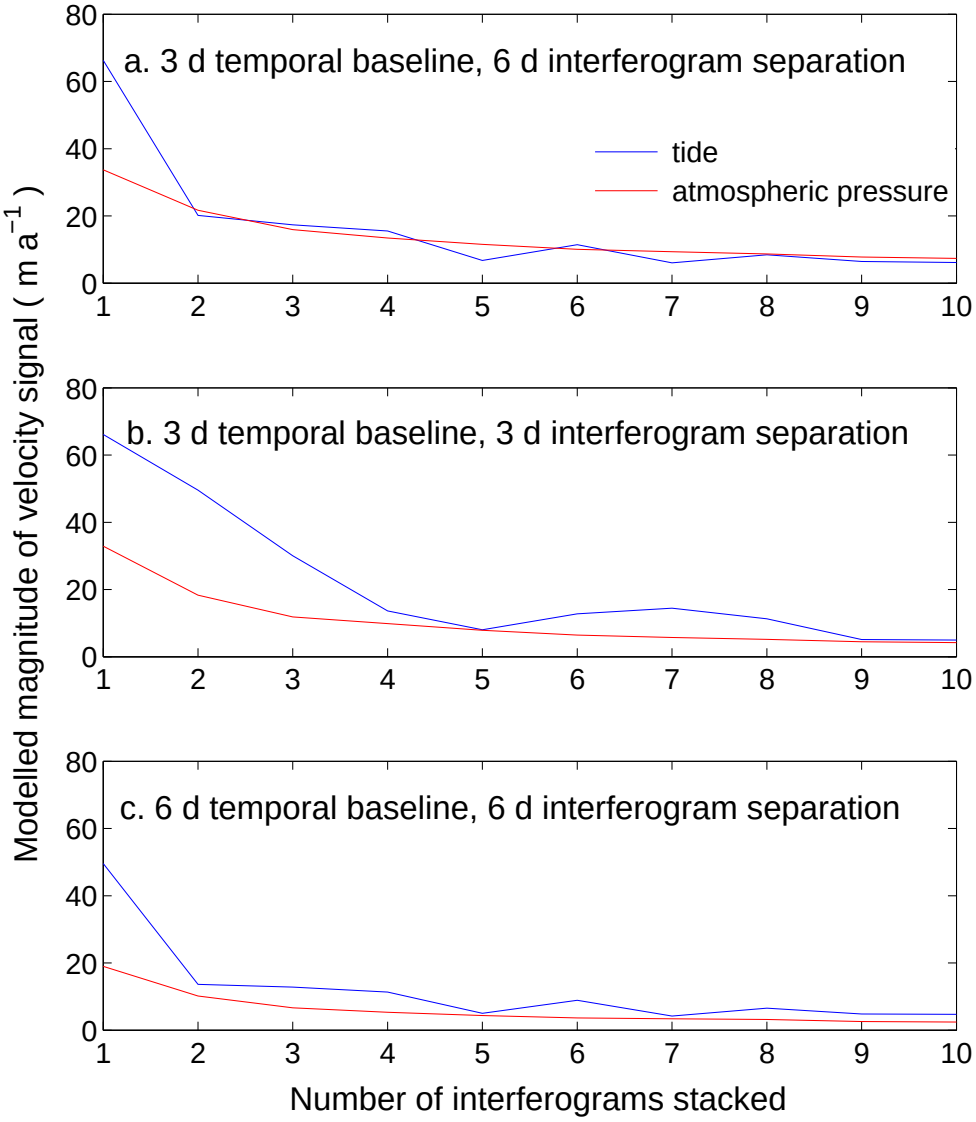

Figure 6.10: Variation in the velocity error arising from modelled tidal and atmospheric pressure (IBE) signals, according to the number of interferograms stacked. Velocity error is dependent upon the temporal sampling regime (figure 6.9) and so I show results for three configurations. a. the configuration used in this study; b. a continuous 3-day sampling configuration whereby the slave image of each interferogram is used as the master image of the following interferogram; c. a continuous sampling configuration (as in *b*) but for a 6-day repeat cycle, as is planned for the Sentinel-1 satellites. Velocity errors are calculated from the standard deviation of the tidal and IBE signals, modelled over a year-long period.

the opportunity to selectively choose interferograms based upon criteria such as coherence and baseline characteristics.

Limitations and Method Development

The primary limitation of the stacking method is its high demand upon data. This was noted by Rignot and MacAyeal (1998) in their earlier assessment of this technique. In the case of this study, for example, I have only been able to form a relatively small stack of images, and there is insufficient usable data to be able to stack interferograms from a second viewing direction. For glaciological applications, the quantity of data suitable for stacking is limited by the relatively rapid timeframe over which signal coherence is lost over ice. To date, stacking has primarily been used for solid Earth applications where surface displacements are relatively small and surface scatterers are relatively stable. This allows coherent interferograms to be formed over much longer time periods than is possible for glaciological applications and consequently provides a more extensive dataset to work with. Future satellite missions with regular short-repeat acquisitions will therefore particularly benefit glaciological applications, by providing longer image sequences that are suitable for stacking. Further improvements to the method described here may also be achieved by utilising more sophisticated stacking regimes (e.g. Biggs *et al.* (2007)), for example by including pixels that are only coherent in a subset of all interferograms in the stack.

Despite the limited data currently available, I find that stacking proves to be a valuable technique for mapping ice shelf velocity, with only relatively few scenes required to reduce residual tidal errors to match the accuracy achievable with tide models in the Amundsen Sea (chapter 5). This is aided by the satellite repeat time, which is exactly 3 days, and yields interferograms that are relatively insensitive to much of the high amplitude, $\sim$ diurnal cyclicity of the tides. As

a consequence, the modelled standard deviation (from its $\sim$ zero mean) of the vertical 3-day tidal displacement is only 26 cm. Both tide model errors (King and Padman, 2005; King *et al.*, 2011) and tidal amplitudes in the Amundsen Sea are broadly comparable to most of Antarctica's coastal waters, with the exception of the Weddell Sea which experiences $\sim$ 2-3 times the tidal range (Padman *et al.*, 2002). Consequently, this study demonstrates that stacking is likely to be an effective method for mapping ice shelf velocity around much of Antarctica. In the case of Weddell Sea ice shelves, or regions where other tidal constituents dominate, it may be necessary to stack more images to reduce the tidal signal to acceptable levels, or to use a combined approach that removes the modelled tidal signal from the stacked interferogram. Alternatively, tide model predictions could be used to guide future satellite acquisition schedules to periods of low tidal variability.

6.8 Conclusions

This study demonstrates a method to map ice shelf flow independently of tide and atmospheric pressure model predictions. By stacking interferograms, I synthesise a longer observation period, and amplify the steady flow signal relative to other temporally-varying signals, such as the vertical motion of an ice shelf in response to the tide and changing atmospheric pressure. Models, instead of being employed to isolate the flow signal, are used to simulate the distribution of residual tidal and IBE signals, and so provide a better constraint upon the remaining error in my velocity solution. By utilising MAI processing, I have demonstrated that 2-d ice shelf velocity can be estimated from InSAR data acquired from a single viewing direction.

I have stacked interferograms to map the ice flow velocity of the Dotson Ice Shelf,

West Antarctica. Residual tide and IBE signals contribute 22 m/yr error to the across-track component of my stacked velocity solution. With the inclusion of other error terms, the total error in my map of velocity magnitude is at most 31 m/yr. The technique of stacking is particularly well-suited to areas where the accuracy of tide and atmospheric pressure models is uncertain, such as remote regions of Antarctica where *in situ* validatory records are scarce. Even in regions where model accuracy is high, stacking will complement the removal of modelled tidal and IBE signals by further reducing residual signals, along with unwanted atmospheric, topographic and baseline effects. In the coming years, the launch of several satellite missions with short revisit times offers the prospect of regular sequences of SAR acquisitions. This study demonstrates that applying a stacking-based approach to these data can further improve estimates of ice shelf flow.

Chapter 7

Synthesis

7.1 Summary of Principle Findings

In the preceding three chapters I have described the work that I have undertaken to develop new datasets and methods for understanding ice-ocean interactions in the Amundsen Sea Sector of the WAIS. In this chapter I firstly summarise the principle findings from each piece of work, I then discuss the significance of the datasets produced, the wider implications of the methods developed and the potential for the future extension of the work described here.

7.1.1 Mapping Amundsen Sea Bathymetry

In Chapter 4, I combined sparse ship-based surveys with satellite-derived gravity data to produce a new bathymetric map of the Amundsen Sea (McMillan *et al.*, 2009). I estimated the depth accuracy of this map to be 120 metres. This is the first published map of this region to utilise data other than that provided by sparse ship-based surveys. The inclusion of satellite gravity data improved the

depth accuracy of the solution by up to 17 %. As a result of additional gravity data being incorporated, large regions of the Amundsen Sea's bathymetry were detailed at a finer spatial resolution than in previously published studies (Nitsche *et al.*, 2007).

7.1.2 Assessing Tide Model Accuracy in the Amundsen Sea

In Chapter 5, I used satellite-based synthetic aperture radar data to assess tide model accuracy in the Amundsen Sea. I compared two methods of validation; one that assessed a model's ability to simulate tidal displacement (i.e. the difference between two tide heights; a *single-difference* technique), and one that assessed a model's ability to predict the difference between two tidal displacements (a *double-difference* technique). I found that the TPXO7.1, CATS2008a_opt and FES2004 tide models performed comparably well, with root mean square (RMS) deviations from observations of $\sim 9 \pm 7$ cm (single-difference technique) and $\sim 11 \pm 4$ cm (double-difference technique). Both methods of validation have advantages; the double difference technique yields a more precise model validation, but the single difference technique directly quantifies the tide model error introduced into model-dependent InSAR-derived velocity estimates. Converting the single-difference RMS deviation into an equivalent across-track displacement yields an estimate of the tide model error associated with model-dependent InSAR-derived ice shelf velocities of $\sim 22 \pm 17$ m/yr.

7.1.3 Mapping Ice Shelf Flow in the Amundsen Sea

In Chapter 6, I described a new method for mapping 2-d ice shelf flow using satellite-based InSAR data acquired from a single viewing direction. InSAR has traditionally been used to provide high resolution and spatially extensive datasets,

but these estimates of ice shelf flow are contaminated by tidal and IBE signals. In this work I aimed to minimise and quantify the tidal and IBE contributions to InSAR-derived velocity estimates, by stacking multiple interferograms and by analysing the statistics of tide and IBE model predictions. The effect of any remaining tide and IBE signals upon across-track velocity estimates was estimated to be 22 m/yr from the modelled distribution of these residual signals. For the first time, along-track ice shelf velocities were determined using multiple aperture interferometry. This eliminated the need for data acquired from a second viewing direction, or for results acquired using (typically less accurate) feature tracking techniques. Along- and across-track velocity components were combined to give a 2-d velocity field, with an associated magnitude error of at most 31 m/yr.

7.2 Significance of Derived Datasets

The work of this thesis is in part motivated by the desire to fully utilise the available satellite-based radar observations to develop datasets for studying the glaciological and oceanic environments of the Amundsen Sea Sector of the WAIS. In this section I discuss how the datasets I have developed can be used for these purposes.

7.2.1 Contribution to Amundsen Sea Glaciology

The datasets developed in this thesis contribute to understanding the past and present behaviour of ice draining the Amundsen Sea Sector of the WAIS.

Past Behaviour of Glaciers Draining into the Amundsen Sea

Knowledge of the past behaviour of the ice sheet is required so as to place contemporary satellite observations within an historical context and to understand the factors which have initiated an ice sheet response in the past. The new bathymetric map described in Chapter 4 (McMillan *et al.*, 2009) contributes towards a better understanding of ice sheet history in two ways. Firstly, it provides a new set of topographic boundary conditions for models of past ice sheet evolution, when the ice extended further across the continental shelf than it does today. This map utilises data covering the entire region and so provides more uniform topographic detail than previous maps. Figure 7.1 shows a comparison between my bathymetry and the most recent previously published bathymetric map of the Amundsen Sea, which was based solely upon ship-based survey data (Nitsche *et al.*, 2007). My bathymetric map resolves more clearly the elevated ridges extending out from the continental shelf break and provides more shorter wavelength topographic detail, such as the undulating surface of the continental shelf region (marked by white ellipses in figure 7.1). This on-shelf detail will allow a more realistic simulation in oceanographic models of the turbulence and mixing the occurs as water passes over a rough bed, as compared to if a relatively smooth bed is assumed (Nitsche *et al.*, 2007).

Secondly, the new bathymetric information extracted from unsurveyed regions can be used to identify previously unsurveyed glaciological bedforms and thus as a resource with which to guide future ship-based surveys. Ship-based surveys can resolve in great detail these glacial bathymetric landforms and so provide evidence with which to constrain the style, timing and duration of ice advance and retreat (Lowe and Anderson, 2002). Surveys can also be used to infer past ice sheet characteristics, such as the locations of paleo-ice streams from mega-scale glacial lineations (Lowe and Anderson, 2002). However, ship surveys in such

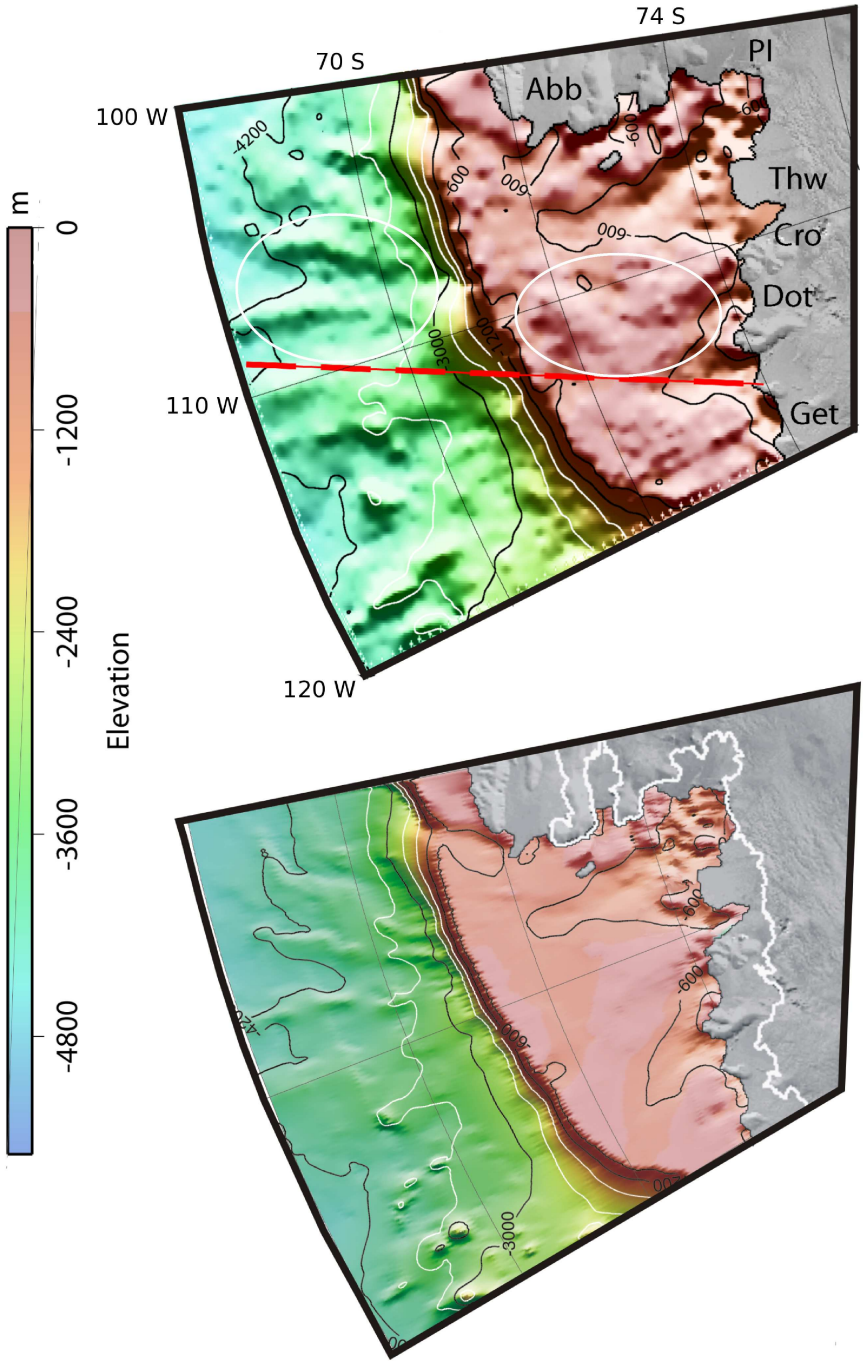

Figure 7.1: Comparison of bathymetry derived in Chapter 4 (top) with map derived solely from ship-based surveys (bottom, redrawn from the data of Nitsche *et al.* (2007)). Plot limited to area common to both bathymetric predictions. *Abb*, Abbott Ice Shelf; *PI*, Pine Island Ice Shelf; *Thw*, Thwaites Ice Shelf; *Cro*, Crosson Ice Shelf; *Dot*, Dotson Ice Shelf; *Get*, Getz Ice Shelf. White ellipses highlight regions where the addition of gravity data resolves additional shorter-wavelength detail both on the continental shelf and on the elevated ridges that extend seaward of the shelf break. Red line indicates location of transect discussed in Chapter 4.

remote regions are time-consuming and expensive, and hence it is important that they are well-directed to regions which will most likely yield the greatest scientific value. I intend to make my bathymetric map available online so that it can be used to aid the planning of these surveys.

Present Behaviour of Glaciers Draining into the Amundsen Sea

The datasets developed by this thesis contribute towards understanding the current behaviour of glaciers draining into the Amundsen Sea. Observations of ice shelf acceleration are central to monitoring the stability of this region. However, the satellite-based methods commonly used to detect velocity changes are reliant upon tide model predictions to remove unwanted signals which arise from the vertical motion of ice shelves (Rignot and Jacobs, 2002; Joughin *et al.*, 2003; Rignot *et al.*, 2004; Vieli *et al.*, 2006). Where model predictions are uncertain, this can lead to errors or data gaps, particularly at locations close to the grounding line, where the gradient of tidal displacement is at its greatest. This region is where basal melt rates peak (Rignot, 1998; Rignot and Jacobs, 2002) and so it can prove difficult to constrain maximum melt rates using methods that rely upon a velocity solution (Joughin and Padman, 2003) (figure 7.2). For example, the modelling study of Payne *et al.* (2007) found that basal melt was concentrated within a narrow region 20 km downstream of the Pine Island Glacier grounding line. However, in mass conservation estimates of the basal melting occurring under this ice shelf, a quarter of this 20 km region had to be excluded because of uncertainties arising from tide model predictions (Payne *et al.*, 2007). My stacked velocity solution addresses this problem by minimising the tidal and IBE signals. This provides a complete InSAR-derived velocity solution in the vicinity of the Dotson Ice Shelf's grounding line. Model statistics can then be used to constrain the uncertainty associated with residual tidal and IBE signals. Furthermore, my assessment of tide models quantifies the accuracy with which tide models can

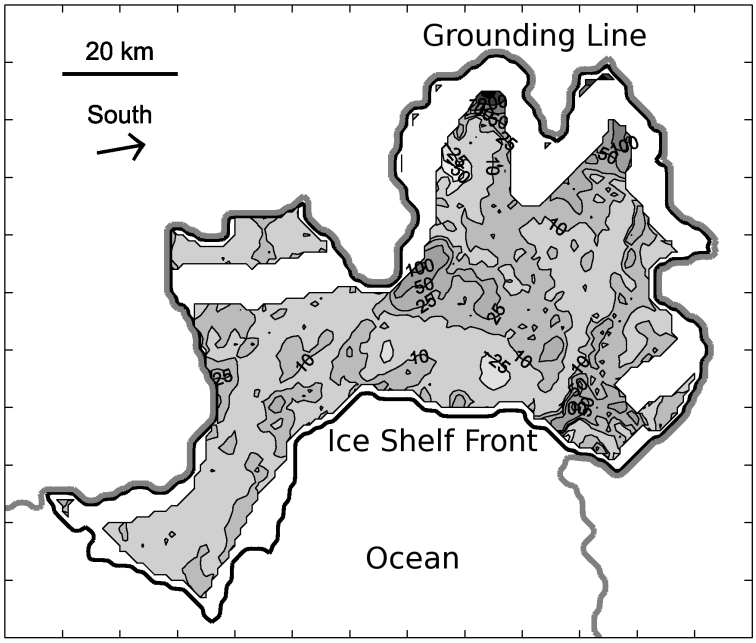

Figure 7.2: Melt rates (m/yr) underneath the Pine Island Ice Shelf determined using a flux divergence calculation, modified from Payne *et al.* (2007). Basal melt rates were not estimated close to the grounding line (white band) because of uncertainty in the velocity map, arising from uncertainty in the accuracy of the tide model correction applied. As a consequence, peak rates of basal melting are not well defined.

reproduce the unwanted tidal component of the InSAR signal in the Amundsen Sea. This assessment indicates the magnitude of velocity changes required to separate long-term trends from tidal artifacts in methods which do utilise tide model predictions to determine ice shelf velocity estimates in the Amundsen Sea.

7.2.2 Contribution to Amundsen Sea Oceanography

In an oceanographic context, the datasets developed by this thesis serve two purposes; that of providing new boundary conditions for models of current ocean circulation and that of providing data for model validation. Oceanographic models require accurate bathymetry, and this is particularly important for studying heat transfer in the Amundsen Sea, as troughs in the sea floor provide a route through

which warm CDW accesses the coastline (Walker *et al.*, 2007; Wahlin *et al.*, 2010). In particular, my bathymetric map (chapter 4) can be used in modelling studies to investigate variations in the heat transported to different ice shelves, to determine whether this can explain differences in ice shelf behaviour in the Amundsen Sea. My bathymetric map also provides comprehensive depth data along the front of all ice shelves in the Amundsen Sea. Accurate depths across the ice shelf front are vital for determining the characteristics of water entering the sub-ice shelf cavity (see, for example, figure 2.11 for an illustration of the depth dependency of ocean temperature). In turn, knowledge of water temperature in the sub-ice shelf cavity allows the heat available for ice melting to be estimated. Bathymetry along the front of ice shelves also influences tidal mixing, and hence heat transfer, in the cavities beneath ice shelves (Makinson *et al.*, 2011).

In terms of validation, my assessment of tide models determines the accuracy of this component of an ocean model. More generally, models of ocean circulation and heat transport in the Amundsen Sea can be validated by assessing how well they predict the magnitude and distribution of melting occurring at the base of an ice shelf (Payne *et al.*, 2007). Basal melting can be inferred from estimates of ice flux divergence (Joughin *et al.*, 2003), once all other terms in the mass balance equation have been accounted for. Such a method requires high quality maps of ice velocity, because any noise in the velocity solution is amplified when the divergence of the velocity field is calculated. As highlighted in section 7.2.1, tidal and IBE errors in the velocity field can also preclude the validation of model predictions of basal melting at the grounding line. Arguably, because melt rates peak close to the grounding line, this is precisely the region where there is the greatest need for models of basal melting to be validated. The Dotson Ice Shelf velocity field determined in chapter 6 is well suited for the purpose of flux divergence calculations, because it combines the technique of stacking with methods (namely InSAR and MAI) that have a high accuracy and

precision, as compared to other remote sensing techniques (e.g. feature tracking). It is intended that estimating the basal melt distribution of the Dotson Ice Shelf will be the focus of future work. By developing new datasets for oceanographic modelling and model validation, my thesis contributes to the effort to understand the ocean processes driving glaciological change in this region, and the reasons for the observed spatial and temporal variability in glaciological behaviour.

7.3 Significance of Thesis Methods

Throughout this thesis I have focused upon developing and assessing radar-based methods for studying ice-ocean interactions in the Amundsen Sea Sector of the WAIS. The wider significance of this work lies in the demonstration that these are viable techniques with wide applicability. As part of each piece of work I have conducted an assessment of the method used; I compared my bathymetric solution to solutions formed solely from ship-based soundings, I assessed the precision with which InSAR methods could validate tide models and I compared stacked InSAR maps of ice shelf flow to those determined by traditional InSAR methods. Through these critical evaluations I have aimed to justify the wider application of the methods described in this thesis. In this section I briefly summarise the significance of each method. By their very nature, much of each method's significance lies in its application to future studies, and so many of the points raised here will be expanded upon when considering extensions to this body of work (section 7.4).

7.3.1 Significance of Bathymetric Prediction Method

The bathymetric map of the Amundsen Sea (Chapter 4) is the first published map of gravity-derived bathymetry from a polar region with perennial sea ice cover. The assessment of this technique demonstrates the improvements in polar bathymetric prediction that can be achieved with the inclusion of gravity data; this had been shown to be the case for the deep, open ocean (Smith and Sandwell, 1994), but until now the validity of applying this method to ice-covered ocean remained unclear. Chapter 4 illustrates the potential of this method to provide comprehensive bathymetric coverage of Antarctic coastal waters and to resolve glaciologically, and oceanographically, important bathymetric details in unsurveyed regions.

7.3.2 Significance of Tide Model Validation Method

The work described in Chapter 5 provides a comprehensive assessment of two InSAR-based methods of tide model validation, and documents the relative strengths of each method. As such it provides a template for tide model validation from satellite-based InSAR data, which can be widely applied to assess tide model accuracy in other remote Antarctic waters where ice shelves exist. Assessments of tide model accuracy serve a number of important roles. Firstly, they quantify the tidal error in estimates of ice shelf flow and provide a basis to choose between alternative methods for estimating flow. This is discussed in more detail in section 7.3.4. Secondly, it forms part of the error budget associated with gravimetry and altimetry products which utilise tide model data to remove unwanted tidal signals. Finally, it can identify areas of tide model weakness and focus efforts to further improve these models.

7.3.3 Significance of Stacking Method of Mapping Ice Shelf Flow

The work described in Chapter 6 demonstrates the viability of a new InSAR-based method for producing high quality 2-d estimates of ice shelf velocity. The principle advantages of this technique are (1) data acquired from a single viewing direction are sufficient to determine 2-d velocity vectors, and (2) model predictions are not required to remove unwanted tidal and IBE signals. This is the first time that multiple aperture interferometry has been used to map ice shelf flow. In view of the likely importance of ice shelf basal melting as a driver of glaciological change, these techniques provide a valuable new method for deriving the high quality velocity maps required by many methods of estimating basal melt (Joughin and Padman, 2003). Furthermore, I have outlined a new approach whereby model statistics are used to estimate the error in velocity maps, which arises from residual tidal and IBE signals. This method can be widely applied in instances where the accuracy of individual model predictions is uncertain.

7.3.4 An Integrated Approach to Mapping Ice Shelf Flow

Together, the work described in Chapters 5 and 6 form an integrated approach to mapping ice shelf flow. Specifically, the tide model inter-comparison described in Chapter 5 provides a basis for selecting the optimal model to use to produce the stacking error statistics, and the quantification of tide model error can be used to guide the stacking approach.

The evaluation of several tide models using the methods of Chapter 5 provides a means to select the most accurate tide model for generating the tidal statistics, as required to determine the uncertainty in stacked flow predictions. In this thesis, I chose to use the FES2004 model for this purpose (Chapter 6), based

upon the assessment of several tide models in Chapter 5. Specifically, I chose the FES2004 model because it exhibited the lowest root mean square deviation from our interferometric observations. Given the close agreement between models, arguments could be made for choosing the TPXO7.1 or CATS2008a_opt models, based upon the apparent inconsistency of FES2004 predictions coincident with the ice shelf. However, such an approach prioritises on-shelf performance over off-shelf performance, which is debatable given the difficulty of modelling tides under ice shelves, where bathymetry and water column thickness are poorly known. Instead I preferred to base model choice on data just seaward of the ice front, where all models produce consistent results and where bathymetry and water column thickness are more certain. Furthermore, at this location all three tide models predict a similar distribution of signals within the 3-day interferograms stacked in Chapter 6 (figure 5.10; standard deviations of 0.26 m (FES), 0.25 m (TPXO) and 0.24 m (CATS)), and so the estimate of tidal error is anyway largely insensitive to the choice of model. Secondly, of these small differences in the models' predicted distributions, FES2004 predicts the largest tidal signal. As such, using FES2004 model statistics in Chapter 6 provides the worst case scenario (i.e. upper bound) for model estimates of tidal error.

Having chosen which tide model to use for the generation of error statistics, a comparison between the model error determined using the method of Chapter 5 and the model statistics determined in Chapter 6 can be used to guide the precise stacking approach to mapping flow. The residual tidal error in a prediction of flow that utilises tide model predictions to remove the tidal signal (Rignot and Jacobs, 2002; Joughin *et al.*, 2003; Rignot *et al.*, 2004; Vieli *et al.*, 2006) can be estimated using the single difference method described in Chapter 5. Here I find this error to be 22 $\pm$ 17 m/yr. In comparison, the residual tidal error associated with my stacking-based approach can be estimated from model statistics (Chapter 6) and equates to a flow velocity error of 17 m/yr. These errors will vary according

to factors such as tide model accuracy, the tidal range in the area of interest and the number of interferograms stacked. The relative magnitude of the errors associated with each method should be considered when choosing how to estimate flow velocities. Where the stacking error is smaller, as is the case here, a purely stacking-based approach to estimating flow velocities (as described in Chapter 6) should be favoured. Model accuracy is insufficient to merit the model being used to remove the tidal signal. However, in cases where the tide model error is smaller than the modelled tidal signal in the stacked interferogram, the model predictions should be used to remove the tidal signal from the stacked velocity estimate. The residual tidal error in the flow prediction would then be estimated from the tide model error as determined in Chapter 5. Such a scenario may occur in regions of Antarctica where tide models are better constrained by in situ data, or where the tidal range is large, such as in the Weddell Sea Sector of Antarctica.

7.4 Future Work

In this section I explore the ways in which the methods developed in this thesis can benefit future studies, and also the improvements that new data can bring to my methods. Firstly I consider the application of the methods developed in this thesis to other relevant areas of study. I then look at how these methods can be applied to current and planned future remote sensing missions.

7.4.1 Application of Methods to Other Areas

In this thesis my work has focused on the Amundsen Sea Sector of West Antarctica, as this is a region where the ocean is believed to be driving rapid glaciological change (Shepherd *et al.*, 2004). Much of the work has focused

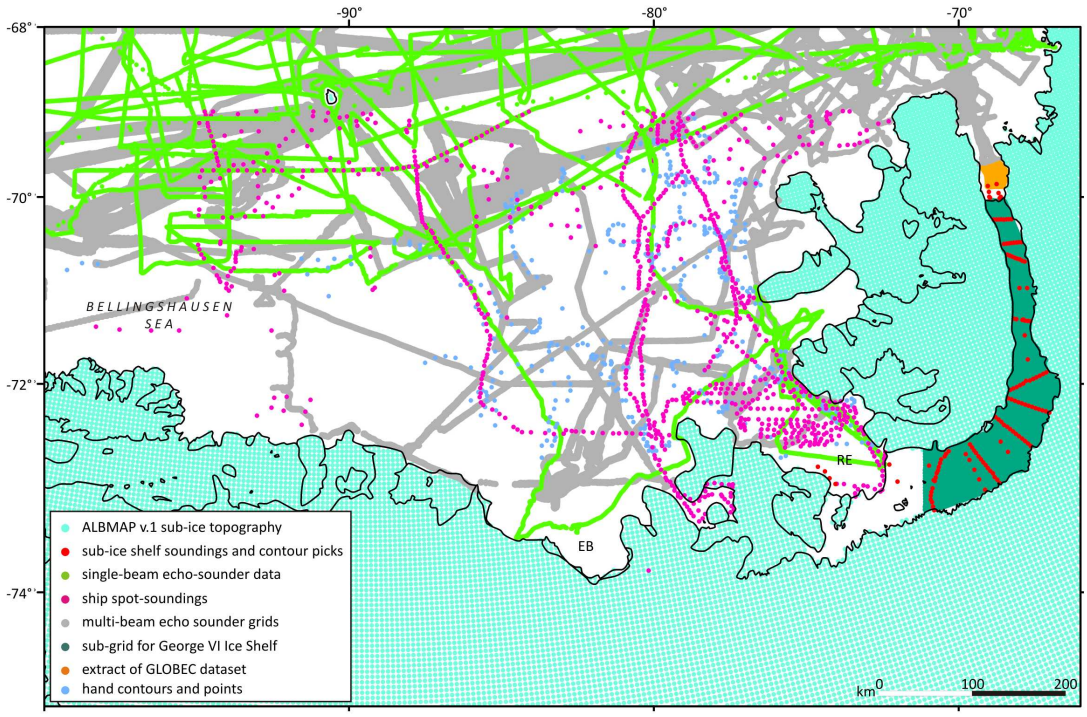

Figure 7.3: Locations of ship-based depth surveys in the Bellingshausen Sea, West Antarctica, upon which the most recent bathymetric map is based, from Graham *et al.* (2011). Green hatching indicates grounded ice and ice shelves. Large areas, particularly along the western coastline, are lacking ship-based depth sounding data.

specifically upon the Dotson Ice Shelf. The methods employed in this thesis are well suited to the study of other ice shelves in the Amundsen Sea Sector of the WAIS and more widely to other remote marine terminating regions of Antarctica and Greenland. In particular, they can provide detail of glaciological and oceanic processes in regions where the effect of the ocean is significant or poorly understood.

Like the Amundsen Sea, the coastal waters of other regions of the WAIS south of 72°S are typically only sparsely covered by ship-based surveys. The work described in Chapter 4 has demonstrated that by utilising marine gravity data, additional bathymetric detail could be resolved in these poorly surveyed regions. This could improve our understanding of past ice extent and current ocean circulation around other parts of the WAIS, such as in the adjacent Bellingshausen

Sea, which is also only sparsely covered by ship-based surveys (figure 7.3). This would provide comparative studies which may enable us to better understand the reasons for the rapid glaciological change occurring in the Amundsen Sea Sector of the WAIS.

The techniques described in this thesis for mapping ice shelf dynamics (Chapters 5 and 6) can be applied to any environment in which glaciers terminate in floating ice which undergoes short-period vertical motion; be it ice shelves in Antarctica or ice tongues in Greenland. Where there is sufficient satellite coverage, the work described here provides a template both for assessing tide model accuracy and for mapping ice shelf flow. These methods can contribute valuable data in the absence of *in situ* measurements and help to build comprehensive records of changes to marine terminating glacier catchments that drain the great ice sheets. In particular, the methods employed here can be applied to other ice shelves in the Amundsen Sea, to further our understanding of ice-ocean interactions in this region. For example, by contrasting flow histories of the neighbouring Dotson and Crosson Ice Shelves, and comparing the bathymetric configuration seaward of each ice shelf (Chapter 4), it would be possible to explore reasons for the differing behaviour exhibited by these two ice shelves.

7.4.2 Application of Methods to Other Remote Sensing Platforms

Current and future remote sensing missions will provide the opportunity to collect new, high quality datasets. These data, in conjunction with the methods developed in this thesis, can be used to improve upon the datasets produced in this thesis. This in turn will provide better data with which to understand the past and present behaviour of the Amundsen Sea Sector of the WAIS, and also

allow the continued monitoring of any ongoing glaciological and oceanic change in this region.

Bathymetric Prediction from Gravimetry

Two current missions have the potential to provide high quality marine gravity data, which in turn could be used to further improve bathymetric maps of the Amundsen Sea, via the method described in Chapter 4. NASA's *Operation IceBridge* is a six-year airborne campaign, planned to run from 2009 - 2015, which is providing repeat observations of the polar regions. Because of the rapid change occurring in the Amundsen Sea region of West Antarctica, this area has been the focus of many flights (figure 7.4) and so a valuable dataset is being acquired. One element of these missions is to record gravity, and because this is an airborne campaign, this can be achieved at a higher resolution and accuracy than satellite-based studies. Using the approach described in chapter 4, the resulting gravity fields can be used to map sea floor topography. In particular, because gravity data is acquired directly (rather than from measurements of sea surface slope), bathymetry can be determined beneath ice shelves. Consequently, the IceBridge mission offers the opportunity to extend the bathymetric map derived here to include sub-ice shelf cavities. This is particularly important for modelling studies of ocean circulation and heat transfer beneath ice shelves, which are currently limited by the lack of such data. IceBridge gravity data have recently been used to map sea floor topography below the Pine Island Ice Shelf (figure 7.5, unpublished work), illustrating the potential of such a method to be extended to other ice shelves covered by the IceBridge campaign (figure 7.4).

The European Space Agency's (ESA) Cryosat-2 satellite was launched in 2010, carrying onboard a radar altimeter capable of providing improvements in the resolution, accuracy and precision of estimates of sea surface slope, as compared

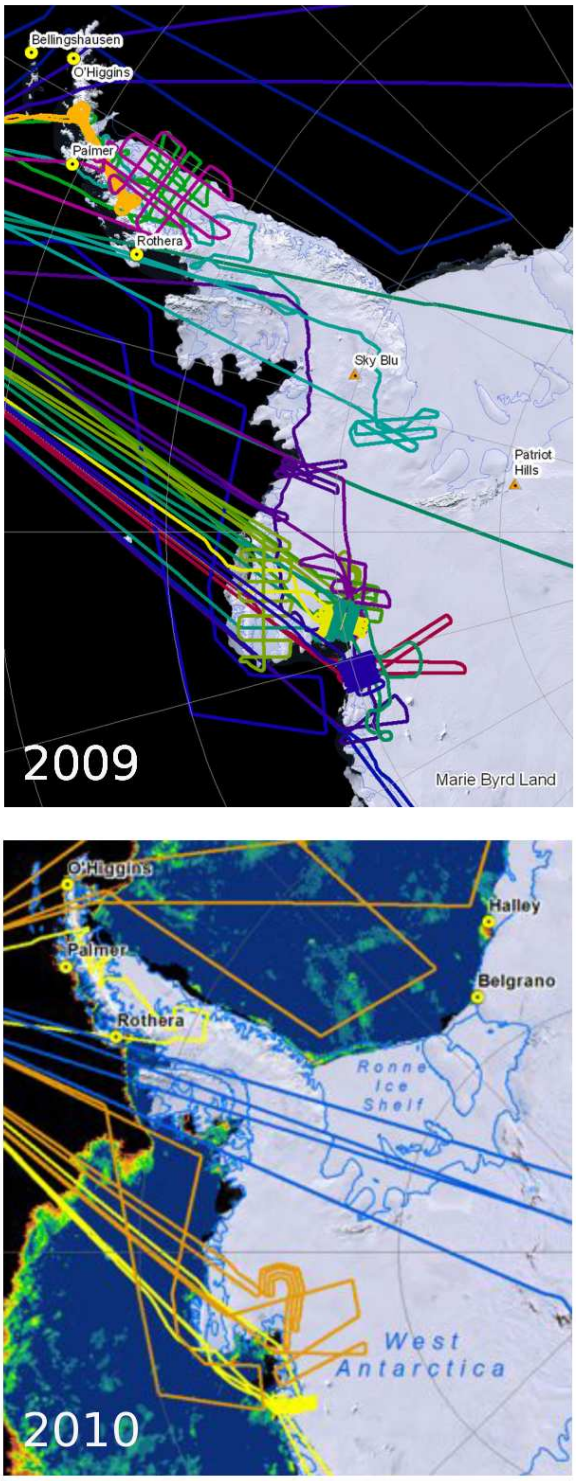

Figure 7.4: WAIS surveys flown during the 2009 (top) and 2010 (bottom) IceBridge campaigns. Map compiled by M. Studinger. These surveys provide extensive coverage of ice shelves in the Amundsen Sea Sector of the WAIS and have the potential to provide high resolution maps of the bathymetry underneath ice shelves.

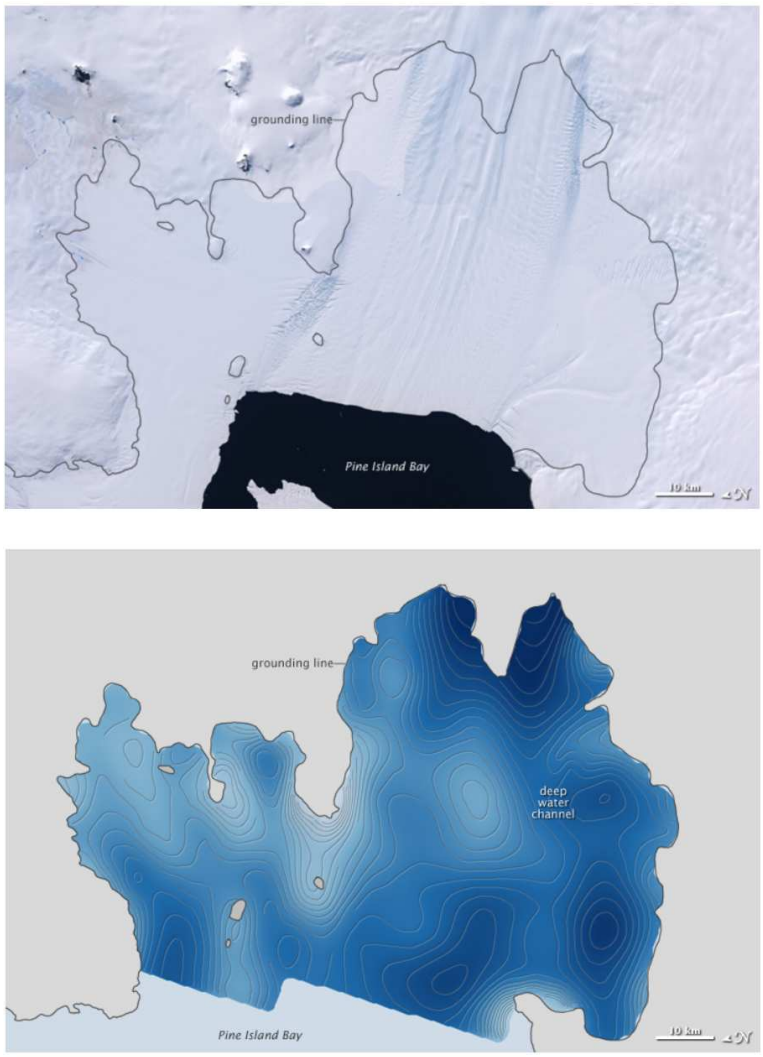

Figure 7.5: The Pine Island Glacier Ice Shelf in the Amundsen Sea of the WAIS. Top, Landsat image of ice surface, black line indicates grounding line. Bottom, bathymetry of sub-ice shelf cavity determined from Operation IceBridge airborne gravimetry. Images taken from NASA's Earth Observatory (http://earthobservatory.nasa.gov). Images created by Jesse Allen, bathymetric model by Michael Studinger and gravity data from Columbia University.

to the ERS data used in Chapter 4. As such, it has the potential to provide a factor of two improvement in the marine gravity field over length scales less than 100 km (Sandwell *et al.*, 2011). Such a gravity field could be used, via the method described in Chapter 4, to further improve polar bathymetric maps. In particular, this could enhance the depth accuracy with which glaciologically-important features in the Amundsen Sea could be mapped with marine gravity, and thus provide better constraints upon the delivery of warm CDW to the base of ice shelves in this region. Early investigations (Stenseng and Andersen, 2011) have produced promising results and indicate that this may indeed be achievable in the future. Looking further ahead, ESA's pair of Sentinel-3 satellites, which are scheduled for launch in 2013, will also carry onboard SAR altimeters with the aim of collecting high quality ocean altimetry data. This mission also holds the potential to further improve bathymetric maps derived from marine gravity.

Ice Shelf Dynamics from InSAR

Since the end of the ERS-1/2 tandem mission phase in 1996, there has been a lack of SAR data with the short ($\sim$ daily) revisit time required by the interferometric methods used here to determine ice shelf flow and tidal motion. In recognition of the value of short repeat SAR data to a wide range of glaciological studies, several recent, current and imminent missions aim to provide new sources of such data.

Between September 2007 and February 2008 ESA placed the ERS-2 and Envisat satellites in a configuration capable of performing short-repeat, cross-platform interferometry, whereby ERS-2 followed Envisat with a time lag of approximately 30 minutes. This has enabled the processing of cross-sensor interferograms (Wegmüller *et al.*, 2009), each capturing surface displacement over a 30-minute interval. The short time-period over which the SAR image pairs were acquired

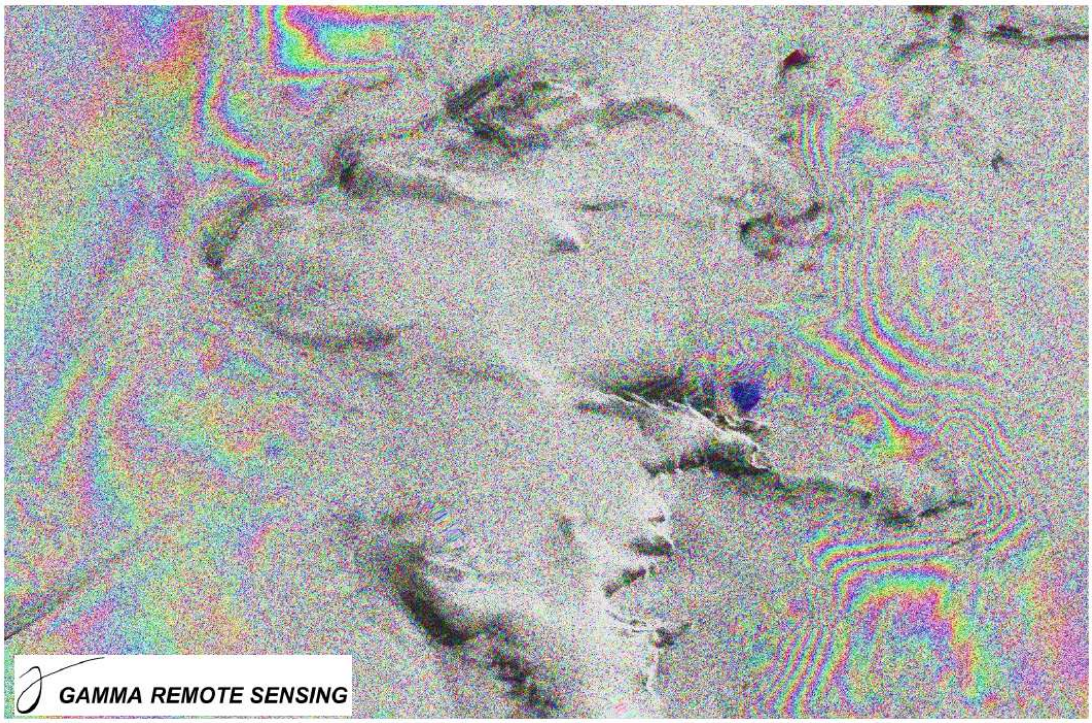

Figure 7.6: ERS2-Envisat cross-platform interferogram acquired over the Larsen Ice Shelf, Antarctic Peninsula. Image courtesy of U. Wegmuller and Gamma Remote Sensing. Overall the phase signal is noisy, although some regions exhibit a spatially coherent signal arising from a combination of topographic, tidal and ice flow effects.

increased the sensitivity of the interferogram to tidal motion relative to ice flow. Consequently these acquisitions should be well-suited to measuring the tidal displacement of an ice shelf and validating tide models through the methods described in Chapter 5. This new dataset has the potential to improve upon the relative imprecision associated with my measurements of single difference tidal displacement (Chapter 5), because there will be less reliance upon tracking techniques to remove the reduced ice flow signal. However, because of inter-platform differences between the ERS-2 and Envisat SAR sensors, constraints are placed upon the interferometric geometry (Wegmüller *et al.*, 2009), which makes the interferograms particularly sensitive to surface topography and noise arising from the effect of near-surface volume scattering. Recent efforts to map ice shelf displacement using cross-interferometry have only had limited success (figure 7.6), but this is an ongoing area of research with the potential to provide valuable, contemporary datasets of tidal motion.

Between March and July 2011, ERS-2 was manoeuvred into a 3-day repeat cycle. During that time, the satellite repeated the acquisitions of ERS-1 in 1992 and 1994, thus providing new data with which to study glaciological change over the past two decades. Extensive coverage of the coastal regions of the WAIS was achieved (figure 7.7) offering the potential to apply the methods of Chapters 5 and 6 to study current ice shelf dynamics, and the changes that have occurred since the early 1990's.

Looking to the future, two missions promise future data relevant to the methods developed in this thesis. ESA's pair of Sentinel-1 satellites are scheduled for launch in 2013-2015 and will each carry onboard a SAR. With a stated objective of monitoring the polar environment and a potential revisit time of 6 days, they could provide a new source of data with which to monitor ice shelf dynamics using the methods described in Chapters 5 and 6. Data from Sentinel-1 should provide the opportunity to improve the quality of measurements of ice shelf tidal motion

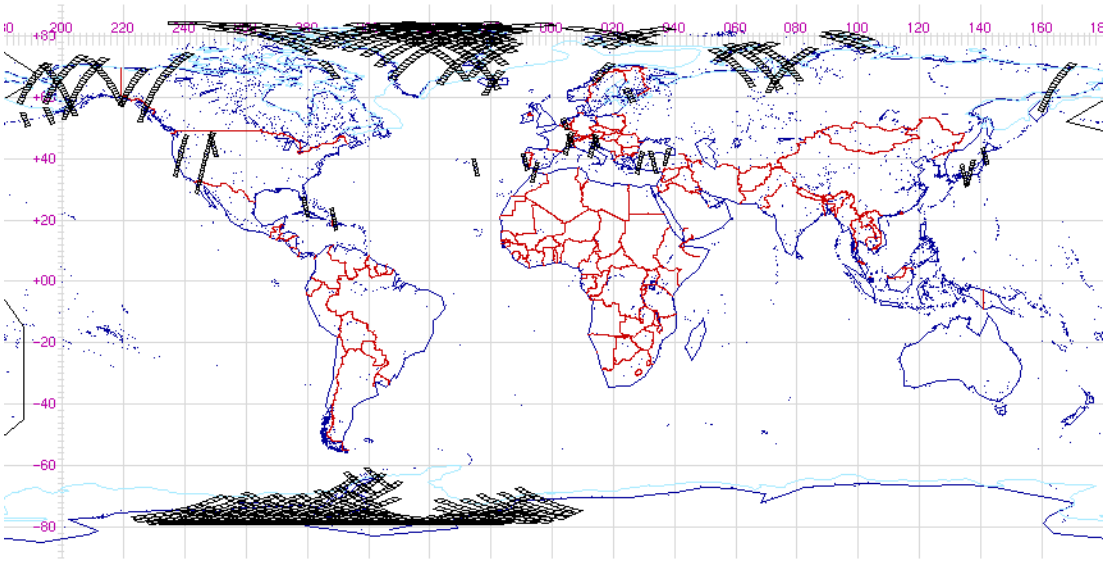

Figure 7.7: ERS-2 ground tracks during 2011 campaign (black boxes). Extensive coverage over coastal regions of the WAIS. Image from http://earth.esa.int/ers/ers2-ice-phase.gif.

and flow using the methods of this thesis. The SAR data will have a higher resolution than the ERS-1/2 SAR's, which should provide higher quality tracking estimates of flow displacement. This in turn will improve the accuracy with which the tidal signal can be isolated using my single difference technique (Chapter 5). Furthermore, the regular repeat time of Sentinel-1 will provide large amounts of data suitable for interferometry. This, in particular, will benefit studies that use stacking to map ice shelf flow (as in Chapter 6), as this technique has a high demand on data. Consequently, it will be possible to extend the stacking method described in Chapter 6 to stack large numbers of interferograms to further reduce unwanted signals. Further into the future, the Canadian Space Agency (CSA) plans to launch the Radarsat Constellation of three satellites in 2014 and 2015. Each satellite will carry onboard a SAR and the individual satellites will be staggered so that together they will provide a 4-day revisit time capable of acquiring data applicable to the methods described in Chapters 5 and 6.

In the last fifteen years, there has been a conspicuous lack of short repeat-time InSAR data suitable for the applications described in this thesis. As such, studies have been limited to archived data and focused upon understanding glaciological processes, rather than providing current monitoring of ongoing glaciological change. With the recent ERS-2 acquisitions and the future Sentinel-1 and Radarsat Constellation missions, the future promises the potential for the methods described in Chapters 5 and 6 to be applied to contemporary data. These will complement the results of this thesis and allow a record spanning twenty years to be constructed, which will shed new light on the changing nature of ice-ocean interactions over this period.

7.5 Concluding Remarks

Over the last twenty years, radar remote sensing has transformed our ability to monitor the Antarctic Ice Sheet. Observations have highlighted the complexity of the Antarctic system and the limitations in our current understanding of the processes that drive it. We are now in a position where we can monitor the response of the ice sheet to a changing climate but not where we can confidently predict its future evolution. In this context, satellite observations can provide the data required to understand past behaviour, monitor ongoing change and test model predictions of the future. In this thesis I have developed datasets and methods that contribute towards this effort, with a particular focus upon the Amundsen Sea Sector of the West Antarctic Ice Sheet. At present, the reasons for the rapid change occurring in this region are not well understood, and the relative influence of anthropogenic and natural factors remains uncertain. The datasets developed in this thesis should, in conjunction with models of the glaciological and ocean environments, aid in the narrowing of this uncertainty. With the prospect of new radar-equipped satellite missions on the horizon, the

methods developed in this thesis will have considerable future relevance. Only by extending the observational record and providing improved datasets for modelling studies will ice-ocean interactions in the Amundsen Sea be better understood, and the implications for future glacier evolution in this region resolved. Given the potential impact of a declining WAIS on rates of sea level rise and numerous coastal centres of population, it is imperative that advances in understanding are made, so as to allow more certain assessments of both the likelihood and timescales of such a scenario occurring.

Bibliography

Alley, R., Blankenship, D., Bentley, C. and Rooney, S. (1986). Deformation of till beneath Ice Stream-B, West Antarctica. *Nature*, **322**, 57–59.

Anandakrishnan, S. (2003). Ice stream D flow speed is strongly modulated by the tide beneath the Ross Ice Shelf. *Geophysical Research Letters*, **30**, 1361.

Anandakrishnan, S., Blankenship, D., Alley, R. and Stoffa, P. (1998). Influence of subglacial geology on the position of a West Antarctic ice stream from seismic observations. *Nature*, **394**, 62–65.

Andersen, O., Woodworth, P. and Flather, R. (1995). Intercomparison of recent ocean tide models. *Journal of Geophysical Research-Oceans*, **100**, 25261–25282.

Assmann, K., Hellmer, H. and Jacobs, S. (2005). Amundsen Sea ice production and transport. *Journal of Geophysical Research*, **110**, C12013.

Bamber, J. and Gomez-Dans, J.L. (2005). The accuracy of digital elevation models of the Antarctic continent. *Earth and Planetary Science Letters*, **237**, 516–523.

Bamber, J.L. and Bindschadler, R.A. (1997). An improved elevation dataset for climate and ice-sheet modelling: validation with satellite imagery. *Annals of Glaciology*, **25**, 438–444.

Bamber, J.L., Gomez-Dans, J.L. and Griggs, J.A. (2009). A new 1 km digital elevation model of the Antarctic derived from combined satellite radar and laser data - Part 1: Data and methods. *The Cryosphere*, **3**, 101–111.

Bassett, S.E., Milne, G.A., Bentley, M.J. and Huybrechts, P. (2007). Modelling Antarctic sea-level data to explore the possibility of a dominant Antarctic contribution to meltwater pulse 1A. *Quaternary Science Reviews*, **26**, 2113–2127.

Bechor, N. and Zebker, H. (2006). Measuring two-dimensional movements using a single InSAR pair. *Geophysical Research Letters*, **33**, L16311.

Biggs, J., Wright, T., Lu, Z. and Parsons, B. (2007). Multi-interferogram method for measuring interseismic deformation: Denali Fault, Alaska. *Geophysical Journal International*, **170**, 1165–1179.

Bindschadler, R. (2002). History of lower Pine Island Glacier, West Antarctica, from Landsat imagery. *Journal of Glaciology*, **48**, 536–544.

Bindschadler, R. and Scambos, T. (1991). Satellite-image-derived velocity-field of an Antarctic ice stream. *Science*, **252**, 242–246.

Bingham, R. and Siegert, M. (2007). Radar-derived bed roughness characterization of Institute and Moller ice streams, West Antarctica, and comparison with Siple Coast ice. *Geophysical Research Letters*, **34**.

Brenner, A., Zwally, H., Bentley, C., Csathó, B., Harding, D., Hofton, M., Minster, J., Roberts, L., Saba, J., Thomas, R. and Yi, D. (2003). Derivation of Range and Range Distributions From Laser Pulse Waveform Analysis for Surface Elevations, Roughness, Slope, and Vegetation Heights, Algorithm Theoretical Basis Document, v.4.1. Tech. Rep. September 2003.

Carrere, L. and Lyard, F. (2003). Modeling the barotropic response of the global ocean to atmospheric wind and pressure forcing - comparisons with observations. *GEOPHYSICAL RESEARCH LETTERS*, **30**.

Cook, A.J. and Vaughan, D.G. (2010). Overview of areal changes of the ice shelves on the Antarctic Peninsula over the past 50 years. *Cryosphere*, **4**, 77–98.

Davis, C. and Ferguson, A. (2004). Elevation change of the Antarctic ice sheet, 1995-2000, from ERS-2 satellite radar altimetry. *IEEE Transactions on Geoscience and Remote Sensing*, **42**, 2437–2445.

De Angelis, H. and Skvarca, P. (2003). Glacier surge after ice shelf collapse. *Science*, **299**, 1560–1562.

Derauw, D. (1999). DInSAR and coherence tracking applied to glaciology: The example of Shirase Glacier. In *FRINGE99 workshop*.

Dixon, T., Naraghi, M., McNutt, M. and Smith, S. (1983). Bathymetric Prediction From Seasat Altimeter Data. *Journal of Geophysical Research*, **88**, 1563–1571.

Doake, C.S.M. (2002). Tide-induced lateral movement of Brunt Ice Shelf, Antarctica. *Geophysical Research Letters*, **29**.

Dorman, L. and Lewis, B. (1970). Experimental Isostasy 1. Theory of Determination of Earths Isostatic Response to a Concentrated Load. *Journal of Geophysical Research*, **75**, 3357.

Dowdeswell, J.A., O Cofaigh, C. and Pudsey, C.J. (2004). Thickness and extent of the subglacial till layer beneath an Antarctic paleo-ice stream. *Geology*, **32**, 13–16.

Dowdeswell, J.A., Evans, J., O'Cofaigh, C. and Anderson, J.B. (2006). Morphology and sedimentary processes on the continental slope off Pine Island Bay, Amundsen Sea, West Antarctica. *Geological Society of America Bulletin*, **118**, 606–619.

Egbert, G. and Erofeeva, S. (2002). Efficient inverse Modeling of barotropic ocean tides. *Journal of Atmospheric and Oceanic Technology*, **19**, 183–204.

Egbert, G., Bennett, A. and Foreman, M. (1994). TOPEX/Poseidon tides estimated using a global inverse model. *Journal of Geophysical Research-Oceans*, **99**, 24821–24852.

Emardson, T.R., Simons, M. and Webb, F.H. (2003). Neutral atmospheric delay in interferometric synthetic aperture radar applications: Statistical description and mitigation. *Journal of Geophysical Research-Solid Earth*, **108**, 8.

Evans, J., Dowdeswell, J.A., Cofaigh, C.O., Benharn, T.J. and Anderson, J.B. (2006). Extent and dynamics of the West Antarctic Ice Sheet on the outer continental shelf of Pine Island Bay during the last glaciation. *Marine Geology*, **230**, 53–72.

Fricker, H. (2002). Tides on Filchner-Ronne Ice Shelf from ERS radar altimetry. *Geophysical Research Letters*, **29**, 1622.

Fyfe, J. and Saenko, O. (2006). Simulated changes in the extratropical Southern Hemisphere winds and currents. *Geophysical Research Letters*, **33**, L06701.

Gille, S. (2002). Warming of the Southern Ocean since the 1950s. *Science*, **295**, 1275–7.

Giulivi, C. and Jacobs, S. (1997). Oceanographic data in the Amundsen and Bellingshausen Seas: N. B. Palmer cruise 9402, February - March 1994, Tech Rep LDEO-97-3. Tech. rep., Lamont-Doherty Earth Obs., Pallisades, New York, New York.

Goldstein, R. (1995). Atmospheric limitations to repeat-track radar interferometry. *Geophysical Research Letters*, **22**, 2517–2520.

Goldstein, R., Zebker, H. and Werner, C. (1988). Satellite radar interferometry - two-dimensional phase unwrapping. *Radio Science*, **23**, 713–720.

Goldstein, R., Engelhardt, H., Kamb, B. and Frolich, R. (1993). Satellite radar interferometry for monitoring ice-sheet motion - application to an Antarctic ice stream. *Science*, **262**, 1525–1530.

Gourmelen, N. and Amelung, F. (2005). Postseismic mantle relaxation in the Central Nevada Seismic Belt. *Science*, **310**, 1473–6.

Gourmelen, N., Kim, S.W., Shepherd, A., Park, J.W., Sundal, A.V., Bjornsson, H. and Palsson, F. (2011). Ice velocity determined using conventional and multiple-aperture InSAR. *Earth and Planetary Science Letters*, **307**, 156–160.

Graham, A., Nitsche, F. and Larter, R. (2011). An improved bathymetry compilation for the Bellingshausen Sea, Antarctica, to inform ice-sheet and ocean models. *The Cryosphere*, **5**, 95–106.

Gray, A., Mattar, K., Vachon, P., Bindschadler, R., Jezek, K., Forster, R. and Crawford, J.P. (1998). InSAR results from the RADARSAT Antarctic Mapping Mission data: Estimation of glacier motion using a simple registration procedure. In T. Stein, ed., *IGARSS '98 - 1998 International Geoscience and Remote Sensing Symposium, Proceedings Vols 1-5 - Sensing and Managing the Environment*, IEEE International Symposium on Geoscience and Remote Sensing (IGARSS), 1638–1640, IEEE, Geosci & Remote Sensing Soc; Univ Washington; NASA; NOAA; USN, Off Naval Res; Natl Space Dev Agcy Japan; Int Union Radio Sci.

Gray, A., Short, N., Mattar, K. and Jezek, K. (2001). Velocities and flux of the Filchner Ice shelf and its tributaries determined from speckle tracking interferometry. *Canadian journal of remote sensing*, **27**, 193–206.

Gray, A.L., Mattar, K.E. and Sofko, G. (2000). Influence of ionospheric electron density fluctuations on satellite radar interferometry. *Geophysical Research Letters*, **27**, 1451–1454.

Grotov, A., Nechaev, D., Panteleev, G. and Yaremchuk, M. (1998). Large scale circulation in the Bellingshausen and Amundsen seas as a variational inverse of climatological Data. *Journal of Geophysical Research*, **103**, 13,011–13,022.

Gudmundsson, G.H. (2006). Fortnightly variations in the flow velocity of Rutford Ice Stream, West Antarctica. *NATURE*, **444**, 1063–1064.

Hanssen, R. (2001). *Radar Interferometry: Data Interpretation and Error Analysis*. Kluwer Academic Publishers, Dordrecht.

Haran, T., Bohlander, J., Scambos, T., Painter, T. and Fahnestock, M. (2006). MODIS mosaic of Antarctica (MOA) image map.

Hartl, P., Thiel, K., Wu, X., Doake, C. and Sievers, J. (1994). Application of SAR interferometry with ERS-1 in the Antarctic. *Earth Observation Quarterly*, **43**.

Helsen, M., van den Broeke, M.R., van de Wal, R., van de Berg, W., van Meijgaard, E., Davis, C., Li, Y. and Goodwin, I. (2008). Elevation changes

in Antarctica mainly determined by accumulation variability. *Science*, **320**, 1626–9.

Holland, P., Jenkins, A. and Holland, D. (2008). The Response of Ice Shelf Basal Melting to Variations in Ocean Temperature. *Journal of Climate*, **21**, 2558–2572.

Holt, J., Blankenship, D., Morse, D., Young, D., Peters, M., Kempf, S., Richter, T., Vaughan, D. and Corr, H. (2006). New boundary conditions for the West Antarctic Ice Sheet: Subglacial topography of the Thwaites and Smith glacier catchments. *Geophysical Research Letters*, **33**, L09502.

Huybrechts, P. (2004). Mass balance of the Cryosphere: Observations and modeling of contemporary and future changes. 491–523, Cambridge University Press, Cambridge, UK.

Jacobs, S.S., Hellmer, H.H. and Jenkins, A. (1996). Antarctic ice sheet melting in the Southeast Pacific. *Geophysical Research Letters*, **23**, 957–960.

Jakobsson, M., Anderson, J.B., Nitsche, F.O., Dowdeswell, J.A., Gyllencreutz, R., Kirchner, N., Mohammad, R., O'Regan, M., Alley, R.B., Anandakrishnan, S., Eriksson, B., Kirshner, A., Fernandez, R., Stolldorf, T., Minzoni, R. and Majewski, W. (2011). Geological record of ice shelf break-up and grounding line retreat, Pine Island Bay, West Antarctica. *Geology*, **39**, 691–694.

Jenkins, A., Dutrieux, P., Jacobs, S.S., McPhail, S.D., Perrett, J.R., Webb, A.T. and White, D. (2010). Observations beneath Pine Island Glacier in West Antarctica and implications for its retreat. *Nature Geoscience*, **3**, 468–472.

Joughin, I. (2002). Ice-sheet velocity mapping: a combined interferometric and speckle-tracking approach. *Annals of Glaciology*, **34**, 195–201.

Joughin, I. and Padman, L. (2003). Melting and freezing beneath Filchner-Ronne Ice Shelf, Antarctica. *Geophysical Research Letters*, **30**, 1477.

Joughin, I., Winebrenner, D. and Fahnestock, M. (1995). Observations of ice-sheet motion in Greenland using satellite radar interferometry. *Geophysical Research Letters*, **22**, 571–574.

Joughin, I., Kwok, R. and Fahnestock, M. (1996a). Estimation of ice-sheet motion using satellite radar interferometry: Method and error analysis with application to Humboldt Glacier, Greenland. *Journal of Glaciology*, **42**, 564–575.

Joughin, I., Winebrenner, D., Fahnestock, M., Kwok, R. and Krabill, W. (1996b). Measurement of ice-sheet topography using satellite radar interferometry. *Journal of Glaciology*, **42**, 10–22.

Joughin, I., Kwok, R. and Fahnestock, M. (1998). Interferometric estimation of three-dimensional ice-flow using ascending and descending passes. *IEEE Transactions on Geoscience and Remote Sensing*, **36**, 25–37.

Joughin, I., Rignot, E., Rosanova, C.E., Lucchitta, B.K. and Bohlander, J. (2003). Timing of recent accelerations of Pine Island Glacier, Antarctica. *Geophysical Research Letters*, **30**, 1706.

Joughin, I., Tulaczyk, S., Bamber, J., Blankenship, D., Holt, J., Scambos, T. and Vaughan, D. (2009). Basal conditions for Pine Island and Thwaites Glaciers, West Antarctica, determined using satellite and airborne data. *Journal of Glaciology*, **55**, 245–257.

Joughin, I., Smith, B.E. and Holland, D.M. (2010). Sensitivity of 21st century sea level to ocean-induced thinning of Pine Island Glacier, Antarctica. *Geophysical Research Letters*, **37**, L20502.

Jung, H., Won, J. and Kim, S. (2009). An Improvement of the Performance of Multiple-Aperture SAR Interferometry (MAI). *IEEE Transactions on Geoscience and Remote Sensing*, **47**, 2859–2869.

Kamb, B. (2001). *Basal zone of the West Antarctic ice streams and its role in lubrication of their rapid motion*, 157–199. American Geophysical Union, Washington DC.

King, J.C. (2003). Validation of ECMWF sea level pressure analyses over the Bellingshausen Sea, Antarctica. *Weather and Forecasting*, **18**, 536–540.

King, M. and Padman, L. (2005). Accuracy assessment of ocean tide models around Antarctica. *Geophysical Research Letters*, **32**, L23608.

King, M., Padman, L., Nicholls, K., Clarke, P., Gudmundsson, G.H., Kulessa, B., Shepherd, A. and Gourmelen, N. (2011). Ocean tides in the Weddell Sea: New observations on the Filchner-Ronne and Larsen C ice shelves and model validation. *Journal of Geophysical Research-Oceans*, **116**.

Kwok, R. and Fahnestock, M.A. (1996). Ice sheet motion and topography from radar interferometry. *IEEE Transactions on Geoscience and Remote Sensing*, **34**, 189–200.

Lang, O., Rabus, B.T. and Dech, S.W. (2004). Velocity map of the Thwaites Glacier catchment, West Antarctica. *Journal of Glaciology*, **50**, 46–56.

Larter, R.D., Graham, A.G.C., Gohl, K., Kuhn, G., Hillenbrand, C.D., Smith, J.A., Deen, T.J., Livermore, R.A. and Schenke, H.W. (2009). Subglacial bedforms reveal complex basal regime in a zone of paleo-ice stream convergence, Amundsen Sea embayment, West Antarctica. *GEOLOGY*, **37**, 411–414.

Laxon, S. (1994). Sea-Ice Altimeter Processing Scheme at the Eodc. *International Journal of Remote Sensing*, **15**, 915–924.

Laxon, S. and McAdoo, D. (1994). Arctic Ocean Gravity Field Derived From ERS-1 Satellite Altimetry. *Science*, **265**, 621–4.

Legresy, B., Wendt, A., Tabacco, I., Remy, F. and Dietrich, R. (2004). Influence of tides and tidal current on Mertz Glacier, Antarctica. *JOURNAL OF GLACIOLOGY*, **50**, 427–435.

Lemke, P., Ren, J., Alley, R., Allison, I., Carrasco, J., Flato, G., Fujii, Y., Kaser, G., Mote, P., Thomas, R. and Zhang, T. (2007). Observations: Changes in Snow, Ice and Frozen Ground. *Climate Change 2007: The Physical Science Basis. Contribution of Working Group I to the Fourth Assessment Report of the Intergovernmental Panel on Climate Change*, 339–378.

Lewis, B. and Dorman, L. (1970). Experimental Isostasy 2. an Isostatic Model for USA Derived from Gravity and Topographic Data. *Journal of Geophysical Research*, **75**, 3367.

Lowe, A.L. and Anderson, J.B. (2002). Reconstruction of the West Antarctic Ice Sheet in Pine Island Bay during the last glacial maximum and its subsequent retreat history. *Quaternary Science Reviews*, **21**, 1879–1897.

Lucchitta, B. and Ferguson, H. (1986). Antarctica - measuring glacier velocity from satellite images. *Science*, **234**, 1105–1108.

Lucchitta, B. and Rosanova, C. (1997). Velocities of Pine Island and Thwaites Glaciers, West Antarctica, from ERS-1 SAR images. In *Third ERS Symposium on Space at the Service of our Environment, Vols. II & III*, vol. 414 of *ESA SPECIAL PUBLICATIONS*, 819–824, European Space Agcy, European Space Agency, Paris, France.

Luckman, A. and Murray, T. (2005). Seasonal variation in velocity before retreat of Jakobshavn Isbræ, Greenland. *Geophysical Research Letters*, **32**.

Luckman, A., Murray, T. and Strozzi, T. (2002). Surface flow evolution throughout a glacier surge measured by satellite radar interferometry. *Geophysical Research Letters*, **29**, 2095.

Luckman, A., Murray, T., Jiskoot, H., Pritchard, H. and Strozzi, T. (2003). ERS SAR feature-tracking measurement of outlet glacier velocities on a regional scale in East Greenland. *Annals of Glaciology*, **36**, 129–134.

Luckman, A., Murray, T., de Lange, R. and Hanna, E. (2006). Rapid and synchronous ice-dynamic changes in East Greenland. *Geophysical Research Letters*, **33**.

Lyard, F., Lefevre, F., Letellier, T. and Francis, O. (2006). Modelling the global ocean tides: modern insights from FES2004. *Ocean Dynamics*, **56**, 394–415.

Lythe, M.B. and Vaughan, D.G. (2001). BEDMAP: A new ice thickness and subglacial topographic model of Antarctica. *Journal of Geophysical Research-Solid Earth*, **106**, 11335–11351.

MacAyeal, D. (1984). Thermohaline Circulation Below the Ross Ice Shelf: A Consequence of Tidally Induced Vertical Mixing and Basal Melting. *Journal of Geophysical Research*, **89**, 597–606.

Makinson, K., Holland, P., Jenkins, A., Nicholls, K. and Holland, D. (2011). Influence of tides on melting and freezing beneath Filchner-Ronne Ice Shelf, Antarctica. *Geophysical Research Letters*, **38**, L06601.

Marks, K.M. and Smith, W. (2006). An evaluation of publicly available global bathymetry grids. *Marine Geophysical Researches*, **27**, 19–34.

Massom, R. and Lupin, D. (2006). *Polar Remote Sensing: Volume II Ice Sheets*. Praxis Publishing Limited, Chichester.

Massonnet, D. and Feigl, K.L. (1998). Radar interferometry and its application to changes in the earth's surface. *Reviews of Geophysics*, **36**, 441–500.

Mattar, K.E. and Gray, A.L. (2002). Reducing ionospheric electron density errors in satellite radar interferometry applications. *Canadian Journal of Remote Sensing*, **28**, 593–600.

McAdoo, D. and Laxon, S. (1997). Antarctic Tectonics: Constraints From an ERS-1 Satellite Marine Gravity Field. *Science*, **276**, 556–61.

McAdoo, D.C. and Marks, K.M. (1992). Resolving Marine Gravity with Ers-1 Satellite Altimetry. *Geophysical Research Letters*, **19**, 2271–2274.

McKenzie, D. and Bowin, C. (1976). The Relationship Between Bathymetry and Gravity in the Atlantic Ocean. *Journal of Geophysical Research*, **81**, 1903–1915.

McMillan, M., Shepherd, A., Vaughan, D.G., Laxon, S. and McAdoo, D. (2009). Amundsen Sea Bathymetry: The Benefits of Using Gravity Data for Bathymetric Prediction. *IEEE Transactions on Geoscience and Remote Sensing*, **47**, 4223–4228.

Mercer, J. (1978). West Antarctic ice sheet and CO2 greenhouse effect: a threat of disaster. *Nature*, **271**, 321–325.

Michel, R. and Rignot, E. (1999). Flow of Glaciar Moreno, Argentina, from repeat-pass Shuttle Imaging Radar images: comparison of the phase correlation method with radar interferometry. *Journal of Glaciology*, **45**, 93–100.

Murray, T., Smith, A., King, M. and Weedon, G. (2007). Ice flow modulated by tides at up to annual periods at Rutford Ice Stream, West Antarctica. *Geophysical Research Letters*, **34**, L18503.

Nitsche, F., Jacobs, S., Larter, R. and Gohl, K. (2007). Bathymetry of the Amundsen Sea continental shelf: Implications for geology, oceanography and glaciology. *Geochemistry Geophysics Geosystems*, **8**.

Padman, L. and Fricker, H.A. (2005). Tides on the Ross Ice Shelf observed with ICESat. *Geophysical Research Letters*, **32**, L14503.

Padman, L., Fricker, H., Coleman, R., Howard, S. and Erofeeva, L. (2002). A new tide model for the Antarctic ice shelves and seas. *Annals of Glaciology*, **34**, 247–254.

Padman, L., Erofeeva, S. and Joughin, I. (2003a). Tides of the Ross Sea and Ross Ice Shelf cavity. *Antarctic Science*, **15**, 31–40.

Padman, L., King, M., Goring, D., Corr, H. and Coleman, R. (2003b). Ice-shelf elevation changes due to atmospheric pressure variations. *Journal of Glaciology*, **49**, 521–526.

Padman, L., Erofeeva, S. and Fricker, H. (2008). Improving Antarctic tide models by assimilation of ICESat laser altimetry over ice shelves. *Geophysical Research Letters*, **35**, L22504.

Pattyn, F. and Derauw, D. (2002). Ice-dynamic conditions of Shirase Glacier, Antarctica, inferred from ERS SAR interferometry. *Journal of Glaciology*, **48**, 559–565.

Payne, A., Vieli, A., Shepherd, A., Wingham, D. and Rignot, E. (2004). Recent dramatic thinning of largest West Antarctic ice stream triggered by oceans. *Geophysical Research Letters*, **31**, L23401.

Payne, A., Holland, P., Shepherd, A., Rutt, I., Jenkins, A. and Joughin, I. (2007). Numerical modeling of ocean-ice interactions under Pine Island Bay's ice shelf. *Journal of Geophysical Research-Oceans*, **112**, 14.

Peacock, N. and Laxon, S. (2004). Sea surface height determination in the Arctic Ocean from ERS altimetry. *Journal of Geophysical Research-Oceans*, **109**.

Pfeffer, W.T., Harper, J.T. and O'Neel, S. (2008). Kinematic constraints on glacier contributions to 21st-century sea-level rise. *Science*, **321**, 1340–3.

Ponte, R.M., Salstein, D.A. and Rosen, R.D. (1991). Sea-level response to pressure forcing in a barotropic numerical-model. *Journal of Physical Oceanography*, **21**, 1043–1057.

Pritchard, H., Murray, T., Luckman, A., Strozzi, T. and Barr, S. (2005). Glacier surge dynamics of Sortebrae, east Greenland, from synthetic aperture radar feature tracking. *Journal of Geophysical Research-Earth Surface*, **110**, 13.

Pritchard, H.D., Arthern, R.J., Vaughan, D.G. and Edwards, L.A. (2009). Extensive dynamic thinning on the margins of the Greenland and Antarctic ice sheets. *Nature*, **461**, 971–975.

Ray, R., Rowlands, D. and Egbert, G. (2003). Tidal models in a new era of satellite gravimetry. *Space Science Reviews*, **108**, 271–282.

Raymond, C., Echelmeyer, K., Whillans, I. and Doake, C. (2001). Ice stream shear margins. *Antarctic Research Series 77. The West Antarctic Ice Sheet: Behavior and environment*, 137–155.

Rignot, E. (1996). Tidal motion, ice velocity and melt rate of Petermann Gletscher, Greenland, measured from radar interferometry. *Journal of Glaciology*, **42**, 476–485.

Rignot, E. (1998). Fast recession of a West Antarctic glacier. *Science*, **281**, 549–551.

Rignot, E. (2001). Evidence for rapid retreat and mass loss of Thwaites Glacier, West Antarctica. *Journal of Glaciology*, **47**, 213–222.

Rignot, E. (2002a). Ice-shelf changes in Pine Island Bay, Antarctica, 1947-2000. *Journal of Glaciology*, **48**, 247–256.

Rignot, E. (2002b). Mass balance of East Antarctic glaciers and ice shelves from satellite data. *Annals of Glaciology, Vol 34, 2002*, **34**, 217–227.

Rignot, E. (2006). Changes in ice dynamics and mass balance of the Antarctic ice sheet. *Philosophical Transactions of the Royal Society A-Mathematical Physical and Engineering Sciences*, **364**, 1637–1655.

Rignot, E. (2008). Changes in West Antarctic ice stream dynamics observed with ALOS PALSAR data. *Geophysical Research Letters*, **35**, L12505.

Rignot, E. and Jacobs, S.S. (2002). Rapid bottom melting widespread near Antarctic ice sheet grounding lines. *Science*, **296**, 2020–2023.

Rignot, E. and MacAyeal, D. (1998). Ice-shelf dynamics near the front of the Filchner-Ronne Ice Shelf, Antarctica, revealed by SAR interferometry. *Journal of Glaciology*, **44**, 405–418.

Rignot, E. and Thomas, R.H. (2002). Mass balance of polar ice sheets. *Science*, **297**, 1502–1506.

Rignot, E., Padman, L., MacAyeal, D. and Schmeltz, M. (2000). Observation of ocean tides below the Filchner and Ronne Ice Shelves, Antarctica, using synthetic aperture radar interferometry: Comparison with tide model predictions. *Journal of Geophysical Research-Oceans*, **105**, 19615–19630.

Rignot, E., Casassa, G., Gogineni, P., Krabill, W., Rivera, A. and Thomas, R. (2004). Accelerated ice discharge from the Antarctic Peninsula following the collapse of Larsen B ice shelf. *Geophysical Research Letters*, **31**, L18401.

Rignot, E., Casassa, G., Gogineni, S., Kanagaratnam, P., Krabill, W., Pritchard, H., Rivera, A., Thomas, R., Turner, J. and Vaughan, D. (2005). Recent ice loss from the Fleming and other glaciers, Wordie Bay, West Antarctic Peninsula. *Geophysical Research Letters*, **32**, L07502.

Rignot, E., Bamber, J., Van Den Broeke, M., Davis, C., Li, Y., Van De Berg, W. and Van Meijgaard, E. (2008). Recent Antarctic ice mass loss from radar interferometry and regional climate modelling. *Nature Geoscience*, **1**, 106–110.

Rippin, D., Vaughan, D. and Corr, H. (2011). The basal roughness of Pine Island Glacier, West Antarctica. *Journal of Glaciology*, **57**, 67–76.

Rodriguez, E. and Martin, J. (1992). Theory and design of interferometric synthetic aperture radars. *IEEE Proceedings - Radar and Signal Processing*, **139**, 147–159.

Rott, H., Skvarca, P. and Nagler, T. (1996). Rapid collapse of northern Larsen Ice Shelf, Antarctica. *Science*, **271**, 788–792.

Rott, H., Rack, W., Skvarca, P. and De Angelis, H. (2002). Northern Larsen Ice Shelf, Antarctica: further retreat after collapse. In R. Winther, JG and Solberg, ed., *Annals of Glaciology*, vol. 34 of *ANNALS OF GLACIOLOGY*, 277–282, Int Glaciol Soc; NASA; US Natl Sci Fdn, INT GLACIOLOGICAL SOC, LENSFIELD RD, CAMBRIDGE CB2 1ER, ENGLAND.

Russel-Head, D. (1980). The melting of free-drifting icebergs. *Annals of Glaciology*, **1**, 119–122.

Sandwell, D. and Smith, W. (1997). Marine gravity anomaly from Geosat and ERS 1 satellite altimetry. *J. geophys. Res*, **102**, 039–10.

Sandwell, D., Garcia, E. and Smith, W. (2011). Potential for Improving Global Marine Gravity from CryoSat and Jason-1. In *Cryosat Validation Workshop*, Frascati, Italy.

Sandwell, D.T. (1992). Antarctic Marine Gravity-Field from High-Density Satellite Altimetry. *Geophysical Journal International*, **109**, 437–448.

Sandwell, D.T. and Price, E.J. (1998). Phase gradient approach to stacking interferograms. *Journal of Geophysical Research-Solid Earth*, **103**, 30183–30204.

Sandwell, D.T. and Sichoix, L. (2000). Topographic phase recovery from stacked ERS interferometry and a low-resolution digital elevation model. *Journal of Geophysical Research-Solid Earth*, **105**, 28211–28222.

Sandwell, D.T. and Smith, W.H.F. (2005). Retracking ERS-1 altimeter waveforms for optimal gravity field recovery. *Geophysical Journal International*, **163**, 79–89.

Sandwell, D.T. and Smith, W.H.F. (2009). Global marine gravity from retracked Geosat and ERS-1 altimetry: Ridge segmentation versus spreading rate. *Journal of Geophysical Research*, **114**, 1–18.

Scambos, T., Bohlander, J., Shuman, C. and Skvarca, P. (2004). Glacier acceleration and thinning after ice shelf collapse in the Larsen B embayment, Antarctica. *Geophysical Research Letters*, **31**, L18402.

Scambos, T., Fricker, H., Liu, C., Bohlander, J., Fastook, J., Sargent, A., Massom, R. and Wu, A. (2009). Ice shelf disintegration by plate bending and hydro-fracture: Satellite observations and model results of the 2008 Wilkins ice shelf break-ups. *Earth and Planetary Science Letters*, **280**, 51–60.

Schmeltz, M., Rignot, E. and Macayeal, D. (2001). Ephemeral grounding as a signal of ice-shelf change. *Journal of Glaciology*, **47**, 71–77.

Schoof, C. (2007). Ice sheet grounding line dynamics: Steady states, stability, and hysteresis. *Journal of Geophysical Research*, **112**, 1–19.

Shepherd, A. and Peacock, N. (2003). Ice shelf tidal motion derived from ERS altimetry. *Journal of Geophysical Research-Oceans*, **108**, 9.

Shepherd, A. and Wingham, D. (2007). Recent sea-level contributions of the Antarctic and Greenland ice sheets. *Science*, **315**, 1529–1532.

Shepherd, A., Wingham, D., Mansley, J. and Corr, H. (2001). Inland thinning of Pine Island Glacier, West Antarctica. *Science*, **291**, 862–864.

Shepherd, A., Wingham, D. and Mansley, J. (2002). Inland thinning of the Amundsen Sea sector, West Antarctica. *Geophysical Research Letters*, **29**, 1364.

Shepherd, A., Wingham, D. and Rignot, E. (2004). Warm ocean is eroding West Antarctic Ice Sheet. *Geophysical Research Letters*, **31**, L23402.

Shepherd, A., Wingham, D., Wallis, D., Giles, K., Laxon, S. and Sundal, A.V. (2010). Recent loss of floating ice and the consequent sea level contribution. *Geophysical Research Letters*, **37**, L13503.

Shoosmith, D. and Jenkins, A. (2006). FRISP Report No. 17: Oceanographic fieldwork in the Amundsen Sea: An overview of cruise JR141. Tech. Rep. 17.

Shum, C., Woodworth, P., Andersen, O., Egbert, G., Francis, O., King, C., Klosko, S., LeProvost, C., Li, X., Molines, J., Parke, M., Ray, R., Schlax, M., Stammer, D., Tierney, C., Vincent, P. and Wunsch, C. (1997). Accuracy assessment of recent ocean tide models. *Journal of Geophysical Research-Oceans*, **102**, 25173–25194.

Siegert, M. (2008). Antarctic subglacial topography and ice-sheet evolution. *Earth Surface Processes and Landforms*, **33**, 646–660.

Siegert, M., Taylor, J., Payne, A. and Hubbard, B. (2004). Macro-scale bed roughness of the siple coast ice streams in West Antarctica. *Earth Surface Processes and Landforms*, **29**, 1591–1596.

Siegert, M., Barrett, P., DeConto, R., Dunbar, R., Ó Cofaigh, C., Passchier, S. and Naish, T. (2008). Recent advances in understanding Antarctic climate evolution. *Antarctic Science*, **20**, 313–325.

Smith, J.A., Hillenbrand, C.D., Kuhn, G., Larter, R.D., Graham, A.G.C., Ehrmann, W., Moreton, S.G. and Forwick, M. (2011). Deglacial history of the West Antarctic Ice Sheet in the western Amundsen Sea Embayment. *QUATERNARY SCIENCE REVIEWS*, **30**, 488–505.

Smith, W. and Sandwell, D. (1994). Bathymetric prediction from dense satellite altimetry and sparse shipboard bathymetry. *Journal of Geophysical Research*, **99**, 21,803 – 21,824.

Smith, W. and Sandwell, D. (1997). Global Sea Floor Topography from Satellite Altimetry and Ship Depth Soundings. *Science*, **277**, 1956–1962.

Smith, W.H.F. (1993). On the Accuracy of Digital Bathymetric Data. *Journal of Geophysical Research-Solid Earth*, **98**, 9591–9603.

Stenseng, L. and Andersen, O. (2011). First results of recovery of short wavelength gravity field signals from Cryosat-2 data. In *Cryosat Validation Workshop*.

Strozzi, T., Luckman, A., Murray, T., Wegmuller, U. and Werner, C. (2002). Glacier motion estimation using SAR offset-tracking procedures. *IEEE Transactions on Geoscience and Remote Sensing*, **40**, 2384–2391.

Sugden, D. (2009). Ice sheets and ice caps. In O. Slaymaker, T. Spencer and C. Embleton-Hamann, eds., *Geomorphology and Global Environmental Change*, chap. 14, 368–402, Cambridge University Press, Cambridge, UK.

Tedesco, M. (2009). Assessment and development of snowmelt retrieval algorithms over Antarctica from K-band spaceborne brightness temperature (1979-2008). *Remote Sensing of Environment*, **113**, 979–997.

Thoma, M., Jenkins, A., Holland, D. and Jacobs, S. (2008). Modelling Circumpolar Deep Water intrusions on the Amundsen Sea continental shelf, Antarctica. *Geophysical Research Letters*, **35**.

Thomas, R., Rignot, E., Casassa, G., Kanagaratnam, P., Acuna, C., Akins, T., Brecher, H., Frederick, E., Gogineni, P., Krabill, W., Manizade, S., Ramamoorthy, H., Rivera, A., Russell, R., Sonntag, J., Swift, R., Yungel, J. and Zwally, J. (2004). Accelerated sea-level rise from West Antarctica. *Science*, **306**, 255–258.

Thompson, D. and Solomon, S. (2002). Interpretation of recent Southern Hemisphere climate change. *Science*, **296**, 895–9.

Trenberth, K., Fasullo, J. and Smith, L. (2005). Trends and variability in column-integrated atmospheric water vapor. *Climate Dynamics*, **24**, 741–758.

Turner, J., Bindschadler, R., Convey, P., Prisco, G., Fahrbach, E., Gutt, J., Hodgson, D., Mayewski, P. and Summerhayes, C. (2009). Antarctic Climate Change and the Environment. Tech. rep., Scientific Committee on Antarctic Research, Cambridge, UK.

Uppala, S., Kallberg, P., Simmons, A., Andrae, U., Bechtold, V., Fiorino, M., Gibson, J., Haseler, J., Hernandez, A., Kelly, G., Li, X., Onogi, K., Saarinen, S., Sokka, N., Allan, R., Andersson, E., Arpe, K., Balmaseda, M., Beljaars, A., Van De Berg, L., Bidlot, J., Bormann, N., Caires, S., Chevallier, F., Dethof, A., Dragosavac, M., Fisher, M., Fuentes, M., Hagemann, S., Holm, E., Hoskins, B., Isaksen, L., Janssen, P., Jenne, R., McNally, A., Mahfouf, J., Morcrette, J., Rayner, N., Saunders, R., Simon, P., Sterl, A., Trenberth, K., Untch, A., Vasiljevic, D., Viterbo, P. and Woollen, J. (2005). The ERA-40 re-analysis. *Quarterly Journal of the Royal Meteorological Society*, **131**, 2961–3012.

van den Broeke, M., Jan, W., van Meijgaard, E. and Reijmer, C. (2006). Identification of Antarctic ablation areas using a regional atmospheric climate model. *Journal of Geophysical Research-Atmospheres*, **111**, 14.

Vaughan, D. (2008). West Antarctic Ice Sheet collapse - the fall and rise of a paradigm. *Climatic Change*, **91**, 65–79.

Vaughan, D.G. and Doake, C.S.M. (1996). Recent atmospheric warming and retreat of ice shelves on the Antarctic Peninsula. *Nature*, **379**, 328–331.

Vaughan, D.G., Smith, A., Corr, H.F.J., Jenkins, A., Bentley, C., Stenoien, M., Jacobs, S.S., Kellogg, T., Rignot, E. and Lucchitta, B. (2001). *Antarctic Research Series Vol. 77. The West Antarctic Ice Sheet: Behavior and Environment*, vol. 77. American Geophysical Union, Washington, D. C.

Vaughan, D.G., Corr, H.F.J., Ferraccioli, F., Frearson, N., O'Hare, A., Mach, D., Holt, J.W., Blankenship, D.D., Morse, D.L. and Young, D.A. (2006). New boundary conditions for the West Antarctic ice sheet: Subglacial topography beneath Pine Island Glacier. *Geophysical Research Letters*, **33**, L09501.

Vieli, A., Payne, A., Du, Z. and Shepherd, A. (2006). Numerical modelling and data assimilation of the Larsen B ice shelf, Antarctic Peninsula. *Philosophical transactions. Series A, Mathematical, physical, and engineering sciences*, **364**, 1815–39.

Vieli, A., Payne, A., Shepherd, A. and Du, Z. (2007). Causes of pre-collapse changes of the Larsen B ice shelf: Numerical modelling and assimilation of satellite observations. *Earth and Planetary Science Letters*, **259**, 297–306.

Wahlin, A., Yuan, X., Björk, G. and Nohr, C. (2010). Inflow of Warm Circumpolar Deep Water in the Central Amundsen Shelf. *Journal of Physical Oceanography*, **40**, 1427–1434.

Walker, D.P., Brandon, M.A., Jenkins, A., Allen, J.T., Dowdeswell, J.A. and Evans, J. (2007). Oceanic heat transport onto the Amundsen Sea shelf through a submarine glacial trough. *Geophysical Research Letters*, **34**, L02602.

Weertman, J. (1974). Stability of the junction of an ice sheet and an ice shelf. *Journal of Glaciology*, **13**, 3–11.

Wegmüller, U., Santoro, M., Werner, C., Strozzi, T., Wiesmann, A. and Lengert, W. (2009). DEM generation using ERS-ENVISAT interferometry. *Journal of Applied Geophysics*, **69**, 51–58.

Werner, C., Wegmuller, U., Strozzi, T. and Wiesmann, A. (2000). Gamma SAR and interferometric processing software. In *Proc. ERS-Envisat Symposium*, 16–20.

Werner, C., Strozzi, T., Wiesmann, A., Wegmuller, U., Murray, T., Pritchard, L. and Luckman, A. (2001). Complimentary measurement of geophysical deformation using repeat-pass SAR. In *Proceedings of the Geoscience and Remote Sensing Symposium, IGARSS '01*, 3255–3258.

Wingham, D., Ridout, A., Scharroo, R., Arthern, R. and Shum, C. (1998). Antarctic elevation change from 1992 to 1996. *Science*, **282**, 456–458.

Wingham, D., Wallis, D. and Shepherd, A. (2009). Spatial and temporal evolution of Pine Island Glacier thinning, 1995-2006. *Geophysical Research Letters*, **36**, L17501.

Wright, T., Parsons, B. and Fielding, E. (2001). Measurement of interseismic strain accumulation across the North Anatolian Fault by satellite radar interferometry. *Geophysical Research Letters*, **28**, 2117–2120.

Zebker, H. and Villasenor (1992). Decorrelation in interferometric radar echoes. *IEEE Transactions on Geoscience and Remote Sensing*, **30**, 950–959.

Zebker, H., Rosen, P. and Hensley, S. (1997). Atmospheric effects in interferometric synthetic aperture radar surface deformation and topographic maps. *Journal of Geophysical Research*, **102**, 7547–7563.

Zwally, H. (2002). ICESat's laser measurements of polar ice, atmosphere, ocean, and land. *Journal of Geodynamics*, **34**, 405–445.